



## **Satellite remote sensing of surface winds, waves, and currents: where are we now?**

Danièle Hauser, Saleh Abdalla, Fabrice Ardhuin, Jean-Raymond Bidlot, Mark Bourassa, David Cotton, Christine Gommenginger, Hayley Evers-King, Harald Johnsen, John Knaff, et al.

### **► To cite this version:**

Danièle Hauser, Saleh Abdalla, Fabrice Ardhuin, Jean-Raymond Bidlot, Mark Bourassa, et al.. Satellite remote sensing of surface winds, waves, and currents: where are we now?. Surveys in Geophysics, 2023, "Oceanography, Hydrology and Glaciology from Space", Guest Editors J. Benveniste, A. Cazenave, 44, pp.1357-1446. <10.1007/s10712-023-09771-2>. <hal-03969955v3>

**HAL Id: hal-03969955**

**<https://hal.science/hal-03969955v3>**

Submitted on 28 Sep 2023

**HAL** is a multi-disciplinary open access archive for the deposit and dissemination of scientific research documents, whether they are published or not. The documents may come from teaching and research institutions in France or abroad, or from public or private research centers.

L'archive ouverte pluridisciplinaire **HAL**, est destinée au dépôt et à la diffusion de documents scientifiques de niveau recherche, publiés ou non, émanant des établissements d'enseignement et de recherche français ou étrangers, des laboratoires publics ou privés.



Distributed under a Creative Commons CC BY 4.0 - Attribution - International License



# Satellite Remote Sensing of Surface Winds, Waves, and Currents: Where are we Now?

Danièle Hauser<sup>1</sup> · Saleh Abdalla<sup>2</sup> · Fabrice Ardhuin<sup>3</sup> · Jean-Raymond Bidlot<sup>2</sup> · Mark Bourassa<sup>4</sup> · David Cotton<sup>5</sup>, et al. *[full author details at the end of the article]*

Received: 25 July 2022 / Accepted: 30 January 2023 / Published online: 18 March 2023  
© The Author(s) 2023

## Abstract

This review paper reports on the state-of-the-art concerning observations of surface winds, waves, and currents from space and their use for scientific research and subsequent applications. The development of observations of sea state parameters from space dates back to the 1970s, with a significant increase in the number and diversity of space missions since the 1990s. Sensors used to monitor the sea-state parameters from space are mainly based on microwave techniques. They are either specifically designed to monitor surface parameters or are used for their abilities to provide opportunistic measurements complementary to their primary purpose. The principles on which is based on the estimation of the sea surface parameters are first described, including the performance and limitations of each method. Numerous examples and references on the use of these observations for scientific and operational applications are then given. The richness and diversity of these applications are linked to the importance of knowledge of the sea state in many fields. Firstly, surface wind, waves, and currents are significant factors influencing exchanges at the air/sea interface, impacting oceanic and atmospheric boundary layers, contributing to sea level rise at the coasts, and interacting with the sea-ice formation or destruction in the polar zones. Secondly, ocean surface currents combined with wind- and wave- induced drift contribute to the transport of heat, salt, and pollutants. Waves and surface currents also impact sediment transport and erosion in coastal areas. For operational applications, observations of surface parameters are necessary on the one hand to constrain the numerical solutions of predictive models (numerical wave, oceanic, or atmospheric models), and on the other hand to validate their results. In turn, these predictive models are used to guarantee safe, efficient, and successful offshore operations, including the commercial shipping and energy sector, as well as tourism and coastal activities. Long-time series of global sea-state observations are also becoming increasingly important to analyze the impact of climate change on our environment. All these aspects are recalled in the article, relating to both historical and contemporary activities in these fields.

**Keywords** Remote sensing · Satellite · Ocean · Atmosphere · Surface wind · Surface waves · Surface current

## Article Highlights

- The different techniques and satellite missions to monitor winds, waves and currents at the ocean surface from space are described
- Sea-state observations from space are widely used in operational meteorology, as well as for research on ocean, atmosphere and climate processes
- Sea-state observations from space are also actively used by the offshore industry, as well as in coastal zone management

## 1 Introduction

Surface winds, waves, and currents are the evident manifestation at the ocean surface of the atmospheric and oceanic thermodynamic ‘engine effect.’ However, in return, the processes affected by surface wind, waves, and current are numerous (Cavaleri et al. 2012). This includes momentum, heat and gas fluxes (e.g.,  $\text{CO}_2$ ) at the air/sea interface, turbulence, and vertical mixing in the ocean and atmospheric boundary layers, production of spray in the atmosphere, and sea-ice evolution. When wind-generated waves in the open ocean arrive at the coast, their properties are modified by the bathymetry and the near surface currents. Several parameters, including surface wind and waves, contribute to a water level increase at the coast during storm events. In addition, waves and currents are major factors in sediment transport and coastal erosion. At high latitudes, the sea-ice evolution is impacted by wind, waves, and currents (Stopa et al. 2018). The ocean surface currents combined with the drift induced by wind-generated waves contribute to the transport of heat, salt and pollutants (Ardhuin et al. 2018). For all these reasons, observations of surface wind, waves, and currents are needed by the research and operational communities to better understand and quantify these interactions and represent them in numerical models.

In the operational application domain, the monitoring and modeling of wind, waves, and currents (as well as ocean temperature, productivity, and bathymetry) are required to promote more safe, efficient, and successful operations at sea and mitigate adverse impacts on navigation, exploration, tourism, and coastal communities. Nowadays, forecasters mainly rely on numerical models based on prognostic equations. The accuracy of the wind and wave forecasts has impressively increased in the last 20 or 30 years (The WISE group report 2007), as a result of improved modeling and initialization by observations in so-called data assimilation procedures. Hence, observations of surface parameters remain necessary on one hand to constrain the numerical solutions of the models, and on the other hand to further improve their physical parameterizations and to validate them. Additionally, more observations are needed to progress in the characterization, understanding and modeling of the evolution of extreme events (severe storms, tropical cyclones).

To simulate the evolution of atmosphere ocean and at seasonal to inter-annual scales, beyond simply coupling numerical atmospheric and oceanic circulation models, it is now recognized that it is important to take into account the role of waves (Babanin et al. 2009; Breivik et al. 2015) and surface currents (Brivoal 2021) because they impact the energy exchanges at the ocean/atmosphere interface and thus the ocean/atmosphere coupling.

In the domain of ocean surface parameters, several “essential climate variables” (ECVs) have been identified by the international community (program GCOS/WMO—Global Climate Observing System from the World Meteorological Organization). This includes the surface wind stress (strongly related to wind speed, but also to surface waves and current),

the sea-state (with main focus on the significant wave height until now), and the sea surface current. To account for this need, both European and US agencies support the creation and curation of long time series of homogenous observations. In particular, the European space agency (ESA) has implemented the “climate change initiative” (CCI) to support re-processing of satellite data for generating long time series of inter-calibrated and homogenized parameters (Dodet et al. 2020; <https://climate.esa.int/fr/projects/sea-state/>).

These statistics are essential to many applications in the maritime industries (comprising sectors as broad as energy, health, leisure, minerals, and transport)—such as offshore fisheries, hydrocarbons / renewables and shipping—on which the future welfare and prosperity of humankind depends (OECD report 2016, OECD is the Organization for Economic Cooperation and Development). At the same time, government agencies and coastal managers tackling the pressures of human activity in environmentally sensitive and highly urbanized near-shore areas require information on related changes and hazards—such as coastal erosion, pollutant dispersal, and water safety which are highly dependent on wind, waves and current conditions.

To properly understand the opportunity presented by observations of wind, waves and currents from space, it is useful to consider the relative advantages and disadvantages of these satellite-based sampling methods compared to those obtained from traditional oceanographic measurements, for example those collected from platforms such as buoys or ships. An excellent discussion of these differences is presented in Srokosz et al. (1995). Additional, more recent, reviews on instrumentation and methods employed for the sampling of metocean parameters are provided by Ardhuin et al. (2019c), Villas Bôas et al. (2019), and Röhrs et al. (2021). In summary, traditional oceanographic measurements are typically obtained from moored or static instruments that record a time series at a single point or, at best, along a single profile. These data often have a very high temporal resolution, but offer little or no information about the spatial variability of the parameters and processes being sampled and studied. Alternatively, ships (or, increasingly, autonomous equivalents such as gliders) and drifters may be used to survey the ocean, to characterize both surface and sub-surface dynamics. However, these measurements are either on a relatively local scale or global with sparse coverage, and their analysis is further compounded by an acute confusion of temporal and spatial signals.

Compared to conventional in-situ methods, remote sensing techniques from space allow observations of wind, waves and currents to be mapped over much larger regions, in a near-synoptic manner. Despite their spatial sampling capabilities, satellites have limited temporal sampling, due to a limited number of satellites and their chosen orbits. Also, consistent with all data that is based on the detection of energy reflected or emitted from the Earth as electromagnetic radiation, these techniques are restricted to only sampling the ocean surface (or the inference of sub-surface properties derived from it) owing to the small penetration depths in water of the wavelengths at which they operate. For some instruments that operate in the visible and infrared part of the spectrum, the prevailing weather conditions (e.g., presence of clouds or rain) can also adversely affect the propagation of signals. These perhaps present the greatest challenges of remote sensing, but—depending on the exact specification requirements—this is confined to only a subset of the available techniques for the measurement of wind, wave, and currents data from space, and far exceeded by the upside of unique datasets with global high-density coverage, that are unable to be obtained any other way. Furthermore, since the archives from multiple long duration satellite missions are now over 30 years for some parameters, these offer the potential for retrieval of observations when no in-situ data were available. Among other uses, this is important for the sampling of extreme events, since these instruments continue to collect

data in conditions for which traditional platforms (e.g., buoys or ships) are damaged or fail to operate; although such measurements can be difficult to calibrate and/or validate owing to lack of alternatives to compare.

In the following, Sect. 2 presents an overview of the different space-based techniques currently used for measuring surface wind, waves and currents from space. This includes a summary of the main principles of measurements from space-borne instruments (microwave radiometers, wind scatterometer, radar altimeter, synthetic aperture radar, near-nadir scatterometry), illustrated with results. Section 3 presents how these observations are used for operational forecasts, for coupled ocean/atmosphere studies, and illustrates the particular case of extreme events. Section 4 discusses the utility of these observations for marine and coastal applications. Finally, Sect.5 concludes this review.

## 2 On the Different Techniques Used from Space

### 2.1 The Physical Background on the Ocean Surface Microwave Remote Sensing

The most common approach to measurement of sea-state characteristics from space, in terms of surface wind, waves, and currents is based on microwave sensors (Gade and Stof-felen 2019). The first (main) reason for this is the ability of the electromagnetic waves in this domain (typically 1–35 GHz) to propagate through the atmosphere even in presence of clouds and precipitation, without too much degradation by these phenomena. The second reason is the good sensitivity of the signal intensity received by these sensors to the surface geometry, directly related to the surface roughness generated by wind and waves. Surface current measurements from space additionally uses, the sensitivity of the received signals to the kinematics of the ocean surface that impacts the temporal and phase properties of the received signal.

Two categories of microwave systems are distinguished. The first category termed “active,” is based on the emission and reception of the return electromagnetic signal by the same system. The sensors under this category are named “RaDAR” (radio detection and ranging). With the development of the global navigation system satellites, the principle of radar systems is also used from space to estimate surface parameters with a bi-static approach (emission and reception from two different locations). In the second category, termed “passive,” sensors do not emit any electromagnetic waves but receive the natural radiation from the Earth’s environment (and in particular from the ocean surface). These are named “microwave radiometers.”

Since World War II, when radar was operationally used for the first time, the microwave domain was divided into different bands of frequency (or wavelength). Table 1 shows the bands used for the measurements of ocean surface parameters from space, with their corresponding range of frequency and wavelength according to the standard designation of IEEE (Institute of Electrical and Electronics Engineers).

In the microwave domain, the electromagnetic waves that strike the ocean surface either from a natural source (the sun) or from a radar system are reflected by the surface, while because of the dielectric nature of the water their penetration in the water under the surface remains very limited in depth (typically over 1/10 of the electromagnetic wavelength). Therefore, the characteristics of the signal received by a satellite microwave sensor depends largely on the scattering mechanism induced by the rough oceanic surface (see below). In the case of passive measurements, additional parameters like surface temperature, emissivity, and atmospheric attenuation also contribute to the received signal (English et al. 2020).

**Table 1** Microwave bands used for ocean remote sensing

Name of the radar band	Frequency	Wavelength
L	1–2 GHz	15.0–30.0 cm
S	2–4 GHz	7.50–15.0 cm
C	4–8 GHz	3.75–7.50 cm
X	8–12 GHz	2.50–3.75 cm
Ku	12–18 GHz	1.67–2.5 cm
K	18–27 GHz	1.11–1.67 cm
Ka	27–40 GHz	0.75–1.11 cm

The main quantities estimated from the electric field detected by the sensor receiver are the normalized radar cross section (NRCS, also note noted  $T_B$ ) for an active sensor, and the brightness temperature for a passive sensor (noted  $T_B$ ). They both characterize the intensity of the electromagnetic field detected by the receiver.

The normalized radar cross section characterizes the averaged backscattering strength of the targets distributed over the illuminated area. In principle, it is defined as the effective area that intercepts the transmitted radar power and then scatters that power isotropically back to the radar receiver. In practice, it is estimated from the radar equation which gives the relation between the transmitted and the received power:

$$P_r(R) = \frac{P_t \lambda^2}{(4\pi)^3} \iint \frac{G^2(x, y) \sigma_0(x, y)}{R^4} dx dy \quad (1)$$

where  $P_r$  and  $P_t$  are the received and transmitted powers respectively,  $\lambda$  the electromagnetic wavelength,  $G$  the antenna gain,  $\sigma_0$  the normalized radar cross section,  $R$  the radial distance, and  $x$  and  $y$  refer to coordinates at the surface. In most applications over the ocean, the assumption is made that  $\sigma_0$  is constant within each resolution cell of the radar so that it can be extracted from the integral and estimated by inverting Eq. (1) for each resolution cell.

The brightness temperature  $T_B$  of the ocean is expressed as the product of the ocean physical temperature  $T_s$  and its emissivity  $\varepsilon$  (when neglecting atmospheric effects).

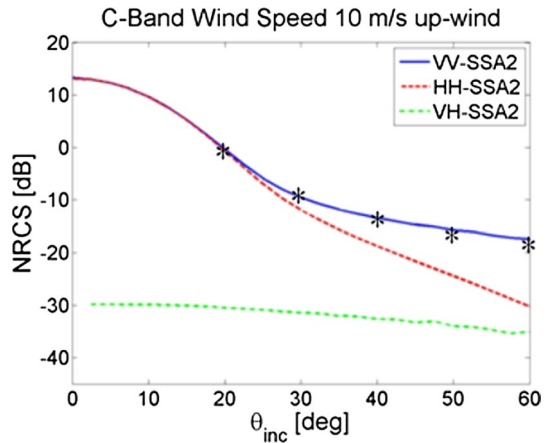
$$T_B = \varepsilon T_s \quad (2)$$

where the emissivity  $\varepsilon$  depends upon sea surface temperature, surface roughness, presence of foam, and on sensor parameters (frequency, polarization, looking angle). When looking from space,  $T_B$  is also impacted by attenuation and scattering of the electromagnetic wave by the atmosphere, mainly due to the presence of water vapor and liquid water (clouds and rain). This effect is much more important at high frequencies (X-K bands) than at low frequencies (C-S- L band).

Another important parameter eventually measured by a microwave system is the phase of the electromagnetic field, which, in the case of the ocean surface, is affected by the Doppler shift generated by the intrinsic motions of the surface scatters.

For both active and passive sensors, measurements performed under multiple polarizations are often chosen, as this helps to separate different surface effects contributing to the backscatter (see below) and make the inversion of geophysical variables more accurate. The most common configuration for  $T_B$  is to use horizontal H and vertical V polarizations. For radar systems which look away from the nadir direction (typically at incidences larger

**Fig. 1** Example of C-band microwave ocean response (normalized radar cross section as a function of incidence angle) in VV, HH and VH polarization from a physically-based model. Stars are VV verification data from the empirical CMOD7 model. Adapted from Foïs (2015)



than  $25\text{--}35^\circ$  with respect to nadir), it is common to use dual polarizations (HH- horizontally emitted and received polarizations and VV-vertically emitted and received polarizations), or even three to four polarization configurations in certain cases (HH, VV, HV, and/or VH).

For a given electromagnetic wavelength, the normalized radar cross section and the brightness temperature depend on the polarization, the surface scattering mechanisms, the geometry of illumination/reception, and eventually on perturbing effects by the atmosphere.

Due to the geometry of the scattering elements at the surface, the  $\sigma_0$  at intermediate incidence angles (typically  $25\text{--}70^\circ$  from nadir) are the strongest in VV polarization while HH  $\sigma_0$  are up to an order of magnitude ( $-10$  dB) weaker (see Fig. 1), and appear more sensitive to second-order scattering processes, initiated at ocean wave breaking events. VH or HV polarization measurements are again an order of magnitude weaker than HH measurements at intermediate incidence angles. However, due to their sensitivity to foam coverage as a result of wave breaking, VH measurements, just like passive radiometers, are very suitable for hurricane wind measurements (Stoffelen et al. 2020a).

The theory of electromagnetic wave scattering from a rough surface has been extensively described in the past in textbooks or papers such as Beekmann and Spizzichino (1963), Ishimaru (1978), Ulaby and Long (2015). Classical reviews of scattering from the ocean surface are described by Valenzuela (1978), Stewart (1984), Geernaert and Plant (1990); (1990) and Martin (2014), with only the main concepts summarized below.

It is common to distinguish two types of scattering mechanisms at the surface, namely the specular (or quasi-specular reflection) and diffuse (or Bragg) scattering.

Specular reflection, associated with a presence of wave facets at the surface oriented perpendicular to the incident electromagnetic waves, results in scattering in a specular direction (like optical rays with a mirror). This type of mechanism is dominant when the incident waves are close to the vertical, because slopes at the surface are usually small (typically less than  $10\text{--}15\%$ ). In this case, the mathematical solution for the normalized radar cross section  $\sigma_0$  results from the Kirchhoff tangent plane approximation of the Maxwell equations (valid when all dimensions of the rough surface are large compared to the electromagnetic wavelength). These electromagnetic equations are then simplified by using either a specular point approach or a correlation function approach—see for example Brown (1990). In both cases, under the assumption that the surface curvature



radius is large compared to the electromagnetic wavelength, the following expression is obtained for  $\sigma_0$  in a monostatic case (Barrick 1968; Brown 1990):

$$\sigma_0(\theta) = \frac{\pi \rho^2 p(\zeta_x, \zeta_y)}{\cos^4(\theta)} \quad (3)$$

where  $\theta$  is the incidence angle with respect to the vertical,  $\rho$  the Fresnel reflection coefficient at normal incidence,  $p(\zeta_x, \zeta_y)$  the joint probability density function evaluated at the specular point slopes, and  $\zeta_x, \zeta_y$  are the slopes in and perpendicular to the radar look directions, respectively. As the probability density (pdf) of surface slopes is dominated by the presence of short waves (typically from a few centimeters to a few meters in wavelength) which respond quickly to the wind,  $\sigma_0$  is related to the slope pdf of the wind-generated waves and hence to the wind. This principle is used by radar altimeter systems to measure wind speed, and by near-nadir scatterometer systems to estimate properties of the long tilting waves on which shorter waves serve as specular facets (see below). Estimation of wind speed from GNSS (Global Navigation Satellite System) is also based on this specular theory.

The other main type of scattering mechanism, which is dominant in non-specular conditions (i.e., for incidence angles larger than typically  $15^\circ$  from the vertical) is a resonant mechanism (Rice 1951; Valenzuela 1978), commonly called Bragg scattering. The mathematical approximate solutions for the scattered field and for  $\sigma_0$  assume that the standard deviation of surface heights is small compared to the wavelength. For the normalized radar cross section in monostatic configuration, the Bragg solution is expressed as (Valenzuela 1978; Plant 1990):

$$\sigma_{0pq}(\theta) = 16\pi k_r^4 \cos^4 \theta \left| g_{pq}(\theta) \right|^2 S(2k_r \sin \theta, 0) \quad (4)$$

where  $p$  and  $q$  denote transmitting and receiving polarizations (vertical-V or horizontal-H),  $k_r$  is electromagnetic wavenumber ( $k_r = \frac{2\pi}{\lambda_r}$  where  $\lambda_r$  is the electromagnetic wavelength),  $S(2k_r \sin \theta, 0)$  the two-dimensional wave height density spectrum estimated at the resonant Bragg wavenumber in the radar look direction, and  $g_{pq}$  the reflection coefficient. This latter is a function of the local incidence and of the complex dielectric constant -see Valenzuela (1978) or Donelan and Pierson (1987) for details.

At the ocean surface, waves of many scales co-exist, typically from very short waves (a few millimeters in wavelengths to several hundred of meters). Furthermore, the short waves which generate the Bragg scattering typically overlay longer waves, and are slightly modified by the latter through hydrodynamic processes, as well as by the atmospheric flow and wind input (Mastenbroek 1996). Therefore, in fact, the physical description of the backscatter at moderate incidence is more complex than that given by Eq. (4). Many theoretical works have been devoted in the past to the proposal of analytical approximations of the exact solution of the Maxwell equations, accounting for the multi-scale nature of the ocean surface (e.g., see Elfouhaily and Guérin 2004; Fois 2015), but we will not enter into more details here.

It is sufficient at this stage to state that the sensitivity of microwave sensors at medium incidence to short Bragg waves is the principle used by so-called “wind scatterometers” to measure the surface wind. Wind scatterometers are radar systems functioning at centimeter wavelengths and looking at typical incidence from  $20$  to  $60^\circ$  with respect to nadir. In these conditions, as a first approximation, the sensitivity to the wind speed of the scatterometer measurement is due to the sensitivity to wind speed of the wind-generated capillary-gravity



waves that serve as Bragg scatterers (Eq. (4)). Furthermore, the development of these short waves is not isotropic: the wave height density spectrum is maximal along the wind-direction and minimal in the cross-wind direction. This fact is used in wind scatterometry to estimate both wind speed and wind direction from the radar signals (see Sect. 2.2.2).

Measurements from microwave radiometers are also based on the same principles but in this case, the instrument receives the natural emission from all incidences, and therefore all the above-mentioned mechanisms are combined.

Of course, the above presentation is necessarily a simplified view of the main scattering mechanisms. In fact, there is generally a combination of effects with, in particular, long ocean waves of small slopes (typically over 10 m in wavelength) tilting the short wind-generated waves and therefore adding a specular effect into the signals scattered at small and medium incidence. In addition, when the sea-state is extreme, specular points due to breaking waves may affect the return power (see, e.g., Phillips 1988; Ericson et al. 1999). From theoretical considerations, it has also been proposed that the polarization ratio can be used as a proxy of the breaking occurrence (Kudryavtsev et al. 2003; Yurovsky et al. 2021).

Because the full physical description is rather complex with substantial uncertainty in some key physical parameterizations (e.g., of wave spectra), in many applications, the inversion of the measured signals is performed by using empirical Geophysical Model Functions (GMFs), which relate the  $\sigma_0$  (or  $T_B$ ) values in different configurations (incidence, polarization, azimuth look angle) to the geophysical parameters to be retrieved. This approach is used in wind scatterometry in particular. The most recent GMFs are expressed as a function of the so-called stress-equivalent 10-m wind vector and of the sea surface temperature (de Kloe et al. 2017; Stoffelen et al. 2017b; Wang et al. 2017) and result in very accurate ocean surface wind vector retrievals (e.g., Vogelzang and Stoffelen 2021).

## 2.2 Space-Borne Instruments, Satellite Missions, and Examples of Results<sup>1</sup>

### 2.2.1 Microwave Radiometers

**2.2.1.1 History and Evolution** Originally, microwave radiometers were developed for measuring parameters such as water vapor, liquid water, temperature, ozone content in the atmosphere of the Earth as well as of other planets. However, it was realized since the mid-1960s that in frequency bands not attenuated by the atmosphere, their measurements are also sensitive to the roughness of the ocean surface. It was also realized that a combination of different electromagnetic frequencies (typically from 5 to 90 GHz) and polarization of the received signal was useful to separate atmospheric effects from surface effects. The first wind speed maps provided at the global scale were obtained from observations at 10.7 GHz of the Scanning Multi-Channel Microwave Radiometer (SMMR) on the Seasat satellite launched in 1978 (Njoku and Swanson 1983). Since then, this approach has been extended to other frequencies or combinations of frequencies (usually in C and X-bands) and used operationally from various series of satellites. A well-known example is the series of the Defense Meteorological Satellite Program (DMSP) that carry the scanning radiometer SSM/I (Special Sensor Microwave Imager, see Hollinger 1991) or its successor SSMIS. Despite some limitations, particularly in regions affected by rain (see below), such observa-

<sup>1</sup> See Appendix 1 for the list of instruments and missions cited in this paper. The list includes the acronym definition, agencies responsible of the instruments and period of operation.

tions of wind speed from radiometer measurements are now systematically used in operational meteorological forecasting systems.

Since the 2000s, new types of microwave radiometers at lower frequencies (L-Band) have been specifically designed to measure the sea-surface salinity and the soil moisture over the continents, such as those on the SMOS and SMAP satellites (Kerr et al. 2010; Entekhabi et al. 2010; Boutin et al., this issue). However, it was shown that the brightness temperature in L-Band allows also to estimate the surface wind speed with a good accuracy, and indeed with a much better performance in rain or high wind conditions than that for higher frequency radiometers (see below).

**2.2.1.2 Principles of measurement** The microwave emission from the ocean surface is used to estimate the ocean surface wind, based on the fact that the wind locally generates surface waves and whitecaps, which contribute to the modification of the surface emissivity from the perfectly flat sea surface value.

The sea surface emissivity contrast  $\Delta e$  induced by the rough and foamy sea surface is expressed as the sum of two terms (Stogryn 1972):

$$\Delta e = (1 - F(U_{10})) \cdot \Delta e_{\text{rough},p}(U_{10}, \theta, \phi, f) + F(U_{10}) \Delta e_{\text{foam},p}^B(U_{10}, \theta, \phi, f) \quad (5)$$

where  $f$ ,  $p$ , and  $\theta$  are the receiving electromagnetic frequency, polarization, and incidence angle of the measuring radiometer, respectively,  $\phi$  is the azimuth angle referenced to the wind direction,  $F(U_{10})$  is the fraction of sea surface area covered by whitecaps at 10 m height,  $U_{10}$  is the wind speed at 10-m height, and  $e_{\text{foam},p}^B$  is the emissivity of typical sea-foam layers. The roughness contribution to surface emission  $\Delta e_{\text{rough},p}$  is formulated as an integral of the directional surface wave spectrum  $S(k, \phi)$  multiplied by an electromagnetic weighting function  $g_p$  specifying the thermal emission contribution of each wave number-directional surface wave component  $(k', \phi')$  (Yueh et al. 1994a,b; Johnson and Zhang 1999):

$$\Delta e_{\text{rough},p}(U_{10}, \theta, \phi, f) = \int_0^{\infty} \int_0^{2\pi} S(k', \phi') g_p(f, \theta, \phi, \varepsilon_{\text{sw}}, k', \phi') k' dk' d\phi' \quad (6)$$

where  $k$  is the wave number and  $\varepsilon_{\text{sw}}$  is sea water relative permittivity. Because the ocean surface becomes rougher and foamier with increasing wind speed, a potential technique became available for the global monitoring of surface winds from Earth orbiting radiometers. The signal of the low microwave frequency (L- to X-bands) radiometers show no sign of saturation or sensitivity loss even in extreme winds. The reason for this is that the low microwave frequency emission from the wind roughened ocean surfaces keeps increasing approximately linearly with wind speed (Nordberg et al. 1971; Monahan and O'Muircheartaigh 1980; Anguelova 2002; Reul and Chapron 2003; Hwang et al. 2019a, b), and does not saturate, even at wind speeds above hurricane force, i.e., 64 kt/32 ms<sup>-1</sup> (Reul et al. 2012, 2016; Yueh et al. 2013; Meissner et al. 2014, 2017; Fore et al. 2016).

The rough sea surface emission  $\Delta e_{\text{rough},p}$  can also be expressed as a function of  $U_{10}$  and of the relative azimuthal direction following:

$$\Delta e_{\text{rough},p}(U_{10}, \theta, \phi, f) = \Delta e_{0,p}(U_{10}, \theta, f) + \Delta e_{1,p}(U_{10}, \theta, f) \cdot \cos(\phi) + \Delta e_{2,p}(U_{10}, \theta, f) \cdot \cos(2\phi) \quad (7)$$

In Eq. (7), the wind direction dependence of the sea surface brightness temperature is in the 1st and 2nd terms of the Fourier series expansion ( $\Delta e_{1,p}$ ,  $\Delta e_{2,p}$ ). It is induced by sea surface anisotropic features (sea surface slope, root mean square height of the small

gravity-capillary waves). Laboratory, tower-based, aircraft, and satellite measurements (Bespalova et al. 1982; Kunkee and Gasiewski 1997; Trokhimovski et al. 2003; Yueh et al. 1995) have demonstrated that the wind direction impacts all Stokes parameters of sea surface (the Stokes parameters characterize the polarization state of the electromagnetic signal). However, the sensitivity of vertically and horizontally polarized brightness temperatures to cloud liquid water and atmospheric water vapor at X- and C-band result in the inability to measure the wind direction with a sufficient accuracy from space, as the signal is relatively small with respect to the amplitudes of errors made in the atmospheric corrections, particularly in rainy conditions. The 3rd (S3) and 4th (S4) Stokes parameters are less sensitive to cloud liquid water and atmospheric water vapor at these frequencies, and are therefore more suitable for wind direction retrieval (Yueh et al. 1995, 2006; Laursen and Skou 2001; Piepmeier and Gasiewski 2001; Lahtinen et al. 2003). This principle is used for the wind direction retrieval from WindSat and SMAP sensors (Meissner and Wentz 2009).

**2.2.1.3 Performance and Limitations** In rain-free conditions, radiometers operated at frequencies in the bands from C- to Ku provide accurate estimates of the surface wind speed (RMS error with buoys < 1 m/s). However, it is difficult to measure surface wind speeds in the presence of precipitation with radiometers that operate at frequencies above 10 GHz (Meissner and Wentz 2009). The atmospheric attenuation by rain droplets increases with increasing frequency (Wentz 2005) and therefore results in a smaller wind signal at the top of the atmosphere. Moreover, it is difficult to model the rain attenuation accurately. This results in large errors for the retrieved wind speeds in the presence of rain if algorithms developed in rain-free conditions are used. It has been shown that this problem can be mitigated to a great extent if the sensor has a combination of multiple low-frequency channels, as demonstrated for the airborne step frequency microwave radiometer (SFMR, 4–8 GHz), where a multi-frequency C-band channel combination is needed to correct for the rain effect and in turn to retrieve the surface wind speed (Klotz and Uhlhorn 2014). For satellite radiometers (e.g., AMSR-E, WindSat and AMSR-2), it is possible to find combinations of the C-band and X-band channels that minimize the rain impact and allow the retrieval of wind speeds in rain conditions (Meissner and Wentz 2009, 2012; Zabolotskikh et al. 2016). Based on this principle, all-weather wind algorithms have been developed for AMSR-E, WindSat and AMSR-2 instruments (see Meissner and Wentz 2012; Shibata 2006). These all-weather wind algorithms need to be trained using match-ups between the measured radiometer brightness temperature  $T_B$  and a reliable true surface wind speed; as described below, surface winds estimated recently from L-band radiometers can be used for this purpose (Meissner et al. 2021). Therefore, currently, the major limiting factor of the C- and X-band radiometers to measure winds are the rain impact and the relatively low spatial resolution (~ 50–60 km) of these sensors. In many cases, this does not allow the resolving of wind structure close to coastlines, around the eye of a tropical cyclone, or for small/compact weather systems (e.g., polar lows).

The recent availability of spaceborne L-band radiometers operating at 1.4 GHz, such as the soil moisture and ocean salinity (SMOS, Kerr et al. 2010) and the soil moisture active passive (SMAP), see Entekhabi et al. 2010. Offers new opportunities to measure surface wind, particularly in stormy and rainy conditions. These L-band radiometers have a distinct advantage over most other passive microwave instruments: due to the use of a long wavelength (21 cm), they are mostly unaffected by rain or frozen precipitation (Wentz 2005; Reul et al. 2012). For wind speeds below 30 kt/15 ms<sup>-1</sup>, the performance of L-band radiometers to measure scalar wind speeds is typically ~ 2–3 m/s; not as good

as that of higher frequency radiometers (i.e., GMI, AMSR-2, WindSat) or scatterometers (QuikSCAT, ASCAT, RapidScat, ScatSat) due to larger radiometer noise and lower sensitivity. It should be noted that the wind speed retrieval of L-band radiometer relies on ocean surface salinity as external ancillary input. In some locations, this ancillary input can be inaccurate, for example in highly dynamical ocean regions such as freshwater river plumes (e.g., Amazon, Congo, Gulf of Bengal and Mississippi), which can result in increased wind speed uncertainty in these areas. For extreme winds, algorithms for SMOS and SMAP have been trained and/or tested using aircraft-based wind speed data from SFMR. Despite the capabilities of this methodology, it is important to acknowledge that there is still a scarcity of reliable in-situ wind measurements in major hurricanes with winds exceeding  $100 \text{ kt}/50 \text{ ms}^{-1}$ , which makes it challenging to train/validate the L-band models or emissivity GMFs. There are many examples of how SMAP and SMOS wind speeds are helpful for both intensity and wind radii estimates (Reul et al. 2012, 2016, 2017; Yueh et al. 2013; Meissner et al. 2014, 2017; Fore et al. 2016) and real-time data are helping tropical cyclone (TC) forecasts as well as adding quality information to historical records. Similar to C- and X-band radiometers, the low spatial resolution ( $\sim 40\text{--}50 \text{ km}$ ) of currently orbiting L-band radiometers imposes a limitation on how close to the coast accurate ocean wind speed measurements can be performed and on the resolution of high wind speed gradients in the inner core of tropical cyclones. For the SMOS case, root mean square differences with other collocated wind speeds from other sensors (SMAP, WindSat, AMSR-2, SSMI) increase from  $\sim 2.5 \text{ m/s}$  for open ocean scenes to  $\sim 5 \text{ m/s}$  when the distance to the coast is less than  $\sim 250 \text{ km}$ . However, combined data from SMOS and SMAP do provide new, independent and very regular estimates of the gale force (R34), damaging (R50), and destructive (R64) wind radii for each given storm, as well as estimates of intensity at  $\sim 40\text{--}50 \text{ km}$  resolution (Reul et al. 2017; Meissner et al. 2017; Fore et al. 2018).

## 2.2.2 Wind Scatterometers

**2.2.2.1 History and Evolution** Wind scatterometers are radar systems specifically designed for measuring the ocean surface wind vector.

The first wind scatterometer entered space in 1978 on-board the Seasat satellite (Born et al. 1979), and demonstrated the feasibility of measuring the ocean wind vector from space. Further NASA instruments were flown on the Japanese spacecraft ADEOS-I and ADEOS-II. Meanwhile, ESA launched the ERS satellites in the 1990s, resulting in the first operational application of scatterometer-derived winds in Numerical Weather Prediction (Stoffelen and Wagner 2013) and hurricane forecasting (Isaksen and Stoffelen 2000), after developing the necessary calibration, empirical Geophysical Model Functions, retrieval, wind direction ambiguity removal, quality assessment and monitoring tools (Stoffelen 1998). Subsequent missions followed, providing operational continuity in the 2000s, for example by QuikSCAT, three ASCAT instruments on the MetOp platform from EUMETSAT (European Organization for the Exploitation of Meteorological Satellites), RapidScat on the International Space Station (ISS), the O-SCAT instruments on the ScatSat and OceanSat Indian platforms, as well as the Chinese HY2 series, and CFOSAT scatterometers (Stoffelen et al. 2019). More recently, the virtual scatterometer constellation was extended in 2021 with HY2-D, and WindRad, to be joined soon by the OceanSat-3 scatterometer. A detailed description of the evolution and performance of scatterometer systems since the 1990s, can be found in Bourassa et al. (2019).

**2.2.2.2 Principles of Measurement** As mentioned in Sect. 2.1, the principle of measurement of wind scatterometers relies on the sensitivity of the normalized radar cross section to the wind speed and wind direction at medium incidences (typically 20–60° from nadir). In this configuration, the radar return is governed by the presence of short capillary-gravity waves generated by the local wind with a very short response time (a few milliseconds). As the wave height density spectrum is not isotropic (higher short waves in the along-wind than in the cross-wind directions), multiple observations over a diversity of incidence and/or azimuths angles are used to estimate both wind speed and wind direction in a Wind Vector Cell (WVC) from the same system.

To achieve this, the current space-borne wind scatterometers are based on either a multiple fixed fan-beam geometry, like ASCAT on MetOp (Figa et al. 2002), or on a rotating pencil-beam geometry with limited incidence angles, like QuikSCAT (Spencer et al. 2000). The wind scatterometers from CFOSAT (Lin et al. 2019) and WindRAD (Tsai et al. 2000) combines both concepts with a rotating fan-beam geometry.

**2.2.2.3 Performance and Limitations** Advanced relative calibration methods with accuracies better than 2% (Belmonte Rivas et al. 2017) provide an excellent basis for the development of accurate GMFs and retrieval codes. Furthermore, the availability of plentiful collocations of different scatterometer types, subsequently allows scatterometer intercalibration and refined wind processing algorithms that produce consistent geophysical products (Wang et al. 2020; Xu and Stoffelen 2020, 2021). Processing codes for all scatterometer types are made available by the Ocean and Sea Ice service-Satellite Application facilities (EUMETSAT OSI-SAF<sup>2</sup>) and associated data sets are accessible from different data centers, e.g., in Europe at EUMETSAT OSI SAF,<sup>3</sup> and the Copernicus Marine Service.<sup>4</sup>

A general method, called triple collocation, was first developed to estimate statistical errors on winds from scatterometer, in-situ and numerical weather prediction (NWP), all at the same time. In combination with studies on 3D atmospheric turbulence spectra and horizontal wind variances, the spatial representation of the collocated measurements has been evaluated and an error analysis on the measurement scale of the scatterometer winds (20–50 km, depending on application) has been performed. Recently, due to the abundance of scatterometers, quadruple collocation studies have also become available (Vogelzang and Stoffelen 2021). Table 2 illustrates these recent results and shows the standard deviations of the wind component errors for moored buoys, ASCAT-A, ScatSat, and collocated NWP of the European Centre for Medium Range Weather Forecast (ECMWF).

Whereas local buoy 10-min-mean measurements are typically very accurate (0.1–1 m s typically), they do not cover the 25-km Wave Vector Cells (WVCs). Therefore, the error standard deviations in Table 2 mainly constitute the natural wind component variability within a 25-km size WVC. Due to their excellent calibration, moored buoy stress-equivalent 10-m winds are used as the absolute calibration reference for scatterometer and atmospheric model winds. The relatively high wind variability in a WVC also determines the quality of the wind retrieval, as different geometric views are consolidated in the retrieval process. For ASCAT, three views are collocated before

<sup>2</sup> <https://nwp-saf.eumetsat.int/site/software/scatterometer/>.

<sup>3</sup> <https://osi-saf.eumetsat.int/products/wind-products>.

<sup>4</sup> <https://marine.copernicus.eu/about/producers/wind-tac>.

**Table 2** Triple collocation error standard deviations for the  $u$  (zonal) and  $v$  (meridional) wind vector components (in  $\text{ms}^{-1}$ ) for buoy (b), ASCAT-A (A), ScatSat (S) and ECMWF (E) collocations on the scatterometer spatial scale ( $\sim 25$  km). The bottom row provides the spread in the results (in  $\text{ms}^{-1}$ ) for the different triple collocation results ((c) AGU, Vogelzang and Stoffelen 2021)

Subset	Buoy		ASCAT-A		ScatSat		ECMWF	
	$\sigma_u$	$\sigma_v$	$\sigma_u$	$\sigma_v$	$\sigma_u$	$\sigma_v$	$\sigma_u$	$\sigma_v$
bAS	1.03	1.12	0.41	0.49	0.78	0.65	–	–
BAE	1.06	1.15	0.34	0.41	–	–	0.94	1.03
bSE	1.09	1.21	–	–	0.72	0.59	0.92	1.03
ASE	–	–	0.43	0.49	0.76	0.65	0.90	0.98
$2\sigma$	0.04	0.04	0.02	0.02	0.03	0.02	0.04	0.04

wind retrieval and its spatial footprints can be well aligned with advanced processing methods, hence reducing the retrieval noise (Vogelzang and Stoffelen 2017). Rotating Ku-band scatterometers have less simple sampling properties, but can benefit from image resolution-enhancement techniques, in particular over sea ice and land surfaces (Long 2017). Unsurprisingly, the scatterometer wind retrieval residual, called maximum likelihood estimator (MLE) error, is a measure of the local inconsistency of the backscatter views and hence related to the local wind variability (Lin et al. 2015).

Whereas natural variability determines the buoy errors, the global NWP model wind component errors in Table 2 are determined by a lack of natural wind variability (Belmonte and Stoffelen 2019). Conversely, ASCAT has the ability to measure the extreme divergence and convergence associated with the updrafts and downdrafts in tropical moist convection, while a global NWP model does not show these (King et al. 2022). Some of this lack of variability is furthermore associated with the local sea surface temperature gradients and can be corrected by averaging wind differences over a few days. Such averaging will remove scatterometer and atmospheric model wind differences due to the transient weather, but will show differences that are related to stationary ocean conditions and due to other systematic errors in the boundary layer parameterization and dynamical model closure (e.g., diffusion operators; see Trindade et al. 2020). The atmospheric model 10-m stress-equivalent wind errors do not only appear on small scales, but also on larger scales as depicted in Fig. 2 (Belmonte and Stoffelen 2019).

### 2.2.3 Radar Altimeters

Spaceborne altimeters are active microwave radars pointing vertically down at the Earth's surface (nadir incidence). As the name suggests, the original purpose of altimeters is to measure the altitude of the satellite i.e., the distance between the satellite and the Earth's surface. Over the oceans, this provides valuable measurements of Sea Surface Height (see Morrow et al. 2023; this issue) from which information is derived about geostrophic currents and sea level. With its unique capability to observe ocean circulation and sea level on global, regional and local scales, satellite altimetry has revolutionized modern oceanography and is now a cornerstone of the global ocean observing system.



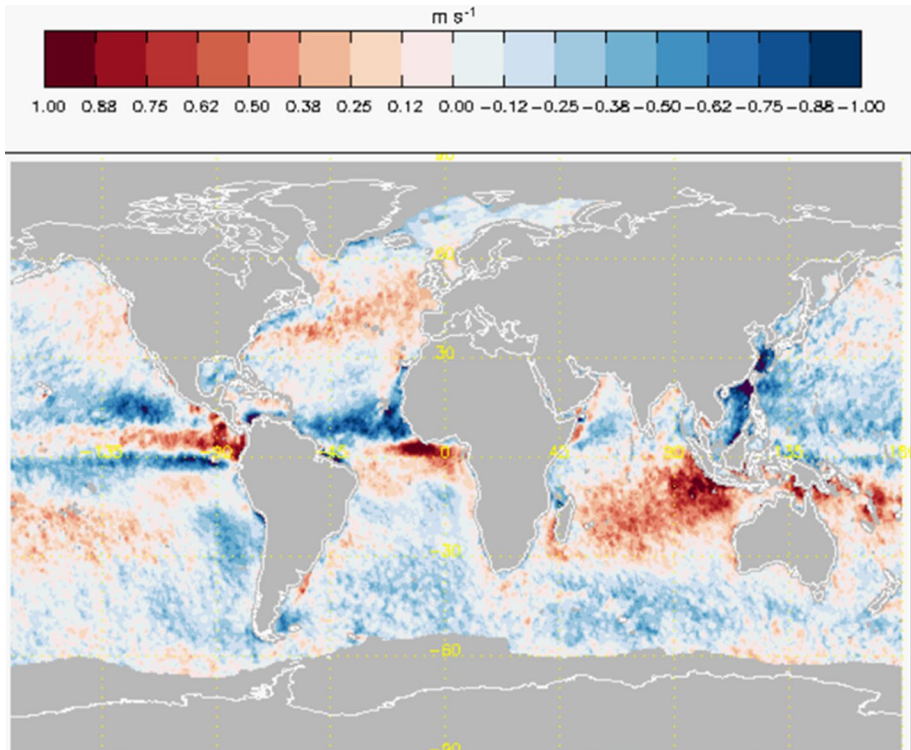


**Fig. 2** Mean differences between ASCAT-A and ERA5 reanalysis for the meridional stress-equivalent 10-m winds after ocean current correction during 2016. From Belmonte and Stoffelen (2019)

Together with SSH, satellite altimeters also provide high-quality measurements of Significant Wave Height (SWH) and wind speed ( $U_{10}$ ), typically referenced to 10 m above the sea surface. Altimeter SWH and  $U_{10}$  have become important satellite observations in their own right, bringing important wind and wave monitoring capability that is particularly relevant for the assimilation in and validation of operational ocean forecasting systems.

Altimeter SWH and  $U_{10}$  also play an essential role in the estimation of the ranging error in altimeter SSH measurements introduced by ocean surface waves, a correction known as sea state bias (SSB) (Srokosz 1986; Gommenginger et al. 2003; Tran et al. 2010; Ablain et al. 2019; Guérou et al. 2022). Today, SSB is still one of the largest contributions to the altimeter SSH error budget (Masters et al. 2012; Cheng et al. 2019), the only altimeter correction to have seen little progress in recent decades. Therefore, accurate and consistent measurements of altimeter SWH and  $U_{10}$  also underpin our ability to accurately observe sea level variability and climate trends. In this chapter we are interested in the altimeter SWH and  $U_{10}$  parameters.

**2.2.3.1 History and Evolution** Satellite altimetry first emerged in the mid-late 1970s and the early success of SEASAT (1978) was followed by a succession of satellite altimeter missions that now form a quasi-continuous time series dating back to 1985 (GEOSAT; Dobson et al. 1987; Carter et al. 1992) comprising the ERS-1/Envisat series, the Topex/Jason series (Lambin et al. 2010; Escudier et al. 2017) and today's Copernicus sentinels (Donlon et al. 2021; The International Altimetry Team 2021).



In April 2010, ESA launched Cryosat-2 as its ice mission, motivated by the need to measure sea ice thickness with greater accuracy in polar regions and observe changes in the Greenland and Antarctica ice sheets (Laxon et al. 2013). Cryosat-2 carried the first altimeter with synthetic aperture radar (SAR) and Interferometric (SARIn) capability (Wingham et al. 2004). The SAR altimetry mode, also known as delay Doppler altimetry (Raney 1998) uses higher Pulse repetition frequency than low-resolution mode (LRM) instruments and unfocused along-track SAR processing to achieve greater precision (lower noise) and finer along-track resolution over leads in sea ice covered oceans (e.g., Arctic). Cryosat-2 was the first spaceborne altimeter to provide SAR mode data over a few ocean regions and these data proved essential to demonstrate, in-orbit, the benefits of SAR mode altimetry over water surfaces (Phalippou and Enjolras 2007; Gommenginger et al. 2011, 2013). SAR altimetry has now been adopted as the default operating mode on all altimeter missions from Copernicus Sentinel-3 Surface topography mission and Sentinel-6 Michael freilich onwards (Donlon et al. 2021).

In 2022, satellite altimetry is expected to take another leap forward with the launch of the surface water and ocean topography mission (SWOT), a collaboration between the USA and France with contributions from Canada and the United Kingdom. The SWOT payload will use across-track SAR interferometry to provide high-resolution 2D observations of water levels over two off-nadir 60 km swaths on either side of the satellite ground-track, accompanied by observations at nadir from a conventional pulse-limited nadir altimeter (Rodriguez et al. 2018; Morrow et al. 2019). SWOT has applications to both hydrology (for inland water) and oceanography (for fine-scale ocean topography), but its capabilities for ocean wind and sea state observing remain to be determined.

**2.2.3.2 Principles of Measurement** Nadir-pointing altimeters transmit short pulses of microwave energy toward the Earth's surface, whence they are reflected back toward the instrument. The timing and temporal evolution of the reflected power measured by the receiver conveys when and how the microwave energy hits, spreads and reflects off the water surface. The temporal shape of the received echo is known as the delay waveform. Up to the launch of Cryosat-2 in April 2010, all altimeter missions carried pulse-limited instruments, whereby the received waveforms are formed by incoherent integration of uncorrelated echoes originating from within the (pulse-limited) footprint as it moves along-track with the satellite. Pulse-limited altimeters have traditionally operated at Ku-band (13.6 GHz) and achieve a footprint 1–10 km in diameter (increasing with significant wave height) thanks to short high-energy pulses (chirps) produced with an elaborate pulse-compression technique involving linear frequency modulation. One exception is SARAL/AltiKa, an India/France altimeter mission also operating in pulse-limited mode but at Ka-band (35 GHz) that reported remarkable improvements in along-track resolution and error reduction (Verron et al. 2018). This mode of operation is variously known as 'pulse-limited,' 'conventional' or 'low-resolution mode' (LRM) altimetry.

The principles used to retrieve the geophysical ocean parameters from the reflected echoes are detailed in many references among which the interested reader is referred to, as the book by Ulaby and Long (2015), or the chapter by Chelton et al. in Fu and Cazenave (2011). Geophysical information about the water surface is contained in the timing and the shape of the waveforms. Figure 3 shows examples of typical altimeter waveforms obtained in LRM and SAR mode over the ocean for average sea state conditions (SWH = 2 m). Note that, for the same sea state, SAR waveforms are naturally narrower and peakier than LRM as a result of unfocused SAR processing.

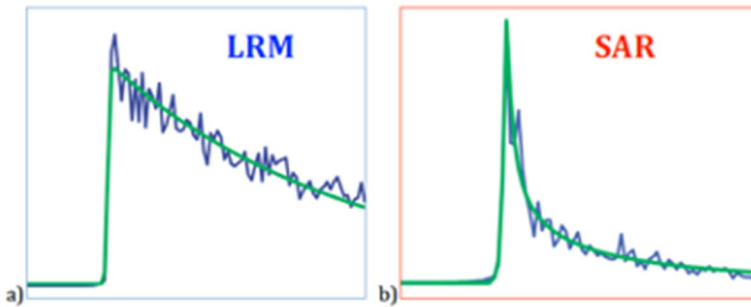


**Fig. 3** Typical ocean type altimeter waveforms (received power versus range distance) for average sea state conditions (significant wave height of about 2 m). **a** in the Low-Resolution Mode (LRM); **b** Synthetic aperture radar mode (SAR). The blue lines are the raw measurement, the solid green lines are fitted waveforms (from Gommenginger et al. 2013)

The geophysical ocean parameters are retrieved by fitting the waveforms with a parametric analytical or numerical model, a process known as 'retracking.' For LRM, waveforms are traditionally fitted with the Brown–Hayne model (Brown 1977; Hayne 1980; Tokmakian et al. 1994; Thibaut et al. 2010; Zaron and DeCarvalho 2016), a well-established analytical model based on theoretical scattering principles. The analytical SAMOSA formulation (Ray et al. 2015) is the equivalent physically-based model to simulate SAR ocean waveforms. SAMOSA is currently the baseline model in the operational Copernicus Sentinel-3 ground-processor, although many other analytical, numerical and empirical methods are still being actively investigated (e.g., Boy et al. 2016; Dinardo et al. 2018, 2021).

Sea surface height (SSH) is derived from the echo arrival time, which indicates the distance traveled by the pulse from the radar to the surface and back. Significant wave height (SWH) is derived from the slope of the leading edge (LRM) or the width of the echo (altimeter SAR mode). Finally, wind speed ( $U_{10}$ ) is related to the maximum reflected power which relates to the normalized radar cross section at normal incidence ( $\sigma_0$ ).

When SSH and SWH are parameters of the fitted models, these are direct outputs of the waveform fitting process. However, for wind speed,  $U_{10}$  has to be inferred from the retrieved backscatter coefficient  $\sigma_0$ . Wind speed estimates are based on Eq. (3) combined with the assumption that the slope pdf is characterized by a Gaussian function. The variance parameter of the slope pdf is known as the mean square slope (mss) of the surface, which is supported by the ocean waves generated by the wind. However, in practice, wind retrieval relies on empirical algorithms that relate the measured  $\sigma_0$  to the wind speed, built either through match-ups between altimeter  $\sigma_0$  and independent wind data (Witter and Chelton 1991; Gommenginger et al. 2002; Gourrion et al. 2002) or with look-up tables tuned against the output from numerical weather prediction (NWP) models (Abdalla 2012). In some cases, wind speed algorithms attempt to account for the mss also having second-order dependencies on sea state, resulting in multi-parameter inversions that usually invoke altimeter significant wave height (Gourrion et al. 2002; Lillibridge et al. 2014).

**2.2.3.3 Performance and Limitations** Much like the principles used to retrieve the geophysical ocean parameters from the reflected echoes themselves, the evaluation of altim-

eter SWH and  $U_{10}$  observations is detailed in many publications. Validation typically involves altimeter match-ups with buoys, weather stations and platforms or other satellites. Comparisons with numerical model output are also common. Evaluation against independent ground-truth is generally considered the gold standard, but results are sensitive to methodological choices and the quality and quantity of fiducial data. In situ wind and wave observations are globally sparse, mostly sited within 50 km of land and almost exclusively in the North Hemisphere. Ensuring that in situ point measurements are representative of wind and wave conditions sampled by the satellite has led to the practice of constructing match-up datasets with maximum separation criteria of 50 km and 30 min between satellite and in situ data. Accordingly, the uncertainties (root mean square error, RMSE) of altimeters operating in LRM are of the order of 0.2 m for significant wave height and 1.0 m/s for wind speed (Table 3).

SAR mode altimetry brings considerable advantages over LRM in terms of improved precision (noise) in 1 Hz along-track SWH (~1.5fold reduction) and finer along-track spatial resolution (~300 m), resulting in particular in useful improvements in coastal regions (Gommenginger et al. 2011; Fenoglio-Marc et al. 2015; Boy et al. 2016; Abdalla et al. 2018). Figure 4 shows two altimeter SWH tracks across atolls in the Central Pacific by Jason-2 LRM (blue) and Cryosat-2 SAR mode (cyan). While SAR mode presents visibly reduced along-track noise in SWH and quasi-continuous records up to 1 km of land, LRM is characterized by large anomalies and data loss within 10–20 km of land that is typical of Ku-band pulse-limited altimeters (Benveniste et al. 2019). In the last decade, major efforts in coastal altimetry have significantly improved the quantity and quality of LRM altimeter data near land (Deng and Featherstone 2006; Cipollini et al. 2010, 2017; Vignudelli et al. 2011; Birol et al. 2021) including now for sea state (Passaro et al. 2014; Schlembach et al. 2020).

In the open ocean, LRM SWH can show along-track variability on scales less than 200 km, with important variations down to 10 km, that are associated with small-scale ocean currents (Ardhuin et al. 2017). The uncertainty in LRM SWH can be considerably reduced by introducing de-noising techniques (Quilfen and Chapron 2019; Dodet et al. 2020). The finer along-track resolution of SAR mode altimetry makes it prone to additional sensitivities to small-scale ocean phenomena, notably long-period waves when these propagate in the direction of altimeter tracks (Aouf and Phalippou 2015; Moreau et al. 2018; Rieu et al. 2021). Impacts on SAR SWH includes biases (~0.2 m) in swell conditions and increased 1 Hz SWH noise that also depends on the period of long waves. New processing and sampling continue to be proposed to mitigate these effects and reduce the risk of contamination of the long-term high-quality sea surface topography record (Moreau et al. 2021; Buchhaupt et al. 2021; Egido et al. 2021).

## 2.2.4 SAR Imagery

**2.2.4.1 History and Evolution** The first Synthetic aperture radar (SAR) system launched in space for scientific applications was that carried by the Seasat (NASA) to monitor the Earth's surface on global scales at high resolution. In addition to a radar altimeter, a wind scatterometer and a microwave radiometer, a visible and infrared radiometer, Seasat carried an L-band SAR. Unfortunately, the mission lasted for only 100 days. However, many of the now existing operational SAR ocean applications (ship detection, sea-ice detection, ocean wave measurements and ocean wind speed) have been demonstrated with Seasat data (Fu and Holt 1982). The launch of ERS-1 (C-band) satellite by ESA in 1991 initiated the provi-

**Table 3** Estimated uncertainty (RMSE) in LRM altimeter significant wave height and wind speed as reported in the literature

LRM	SWH RMSE (m)	U10 RMSE (m/s)	Missions	Notes
Zieger et al. (2009)	0.18	1.17	GS, E1, TX, E2, GFO, J1, N1	195 buoys (NDBC); match-up within 50 km, 30 min
Calafat et al. (2017)	0.17	0.99	C2 (LRM), J2	89 buoys (NDBC), > 40 km from land; match-up within 20 km, 30 min
Dodet et al. (2020)	0.23	–	E1, TX, E2, GFO, J1, N1, J2, C2, SA, J3	73 buoys (various), > 200 km from land; match-up within 50 km, 30 min

Key to abbreviations: GS (Geosat), E1 (ERS-1), TX (TOPEX), E2 (ERS-2), GFO (Geosat Follow-on), J1 (Jason-1), N1 (Envisat), J2 (Jason-2), C2 (Cryosat-2), SA (SARAL AltiKa), J3 (Jason-3). NDBC refers to the US National Data Buoy Center (<https://www.ndbc.noaa.gov>)

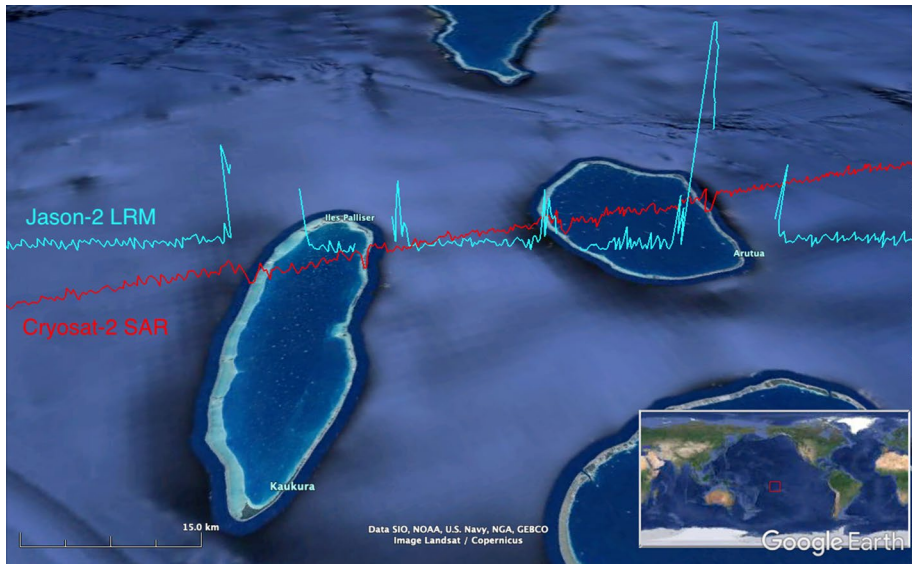


**Fig. 4** Altimeter transects across Palliser islands atolls in French Polynesia the Central Pacific showing the significant wave height measured by the Jason-2 Low-Resolution Mode altimeter (cyan) and the Cryosat-2 altimeter operating in SAR mode (red). Note the anomalous spikes and data loss at the water-land interfaces with LRM compared to the continuous records obtained in SAR mode

sion of operational services in Europe, with routine and global acquisition of imagettes over the open ocean used for measuring and assimilating 2D swell spectra. Since then, numerous spaceborne SARs have been orbiting the Earth, operating in C-, X- and L-bands. The imaging capacity of SAR systems and the processing capabilities have increased substantially since 1978. The increased transmitted bandwidth has improved the spatial resolution down to meters, and the phased array antenna technology has increased the extent of coverage up to 400 km swath width. Consequently, present SAR systems are very flexible in terms of spatial resolution, polarization, swath width and operation modes. In comparison to other systems presented here, the SAR missions cannot provide continuous acquisitions due to on-board memory and down-link capacities, and the acquisition modes are exclusive. These limitations imply a strategy to organize the acquisition planning and solve the potential conflicts with respect to the mission priorities (i.e., targeted applications).

To date, SAR images collected from space over the ocean are routinely used to estimate the spectral properties of ocean waves, the surface velocity, or the surface wind. For each of these applications, the measurement principles and performances are described here below.

#### 2.2.4.2 Surface Ocean Waves from SAR

##### (1) Principles of Measurement

The SAR is a two-dimensional imaging system that can produce images of the ocean surface with a high spatial resolution. In the range direction (across-track), the sampling of the backscattered signal is achieved by using the frequency modulation of the chirped radar

signal, with the resolution in distance controlled by the frequency bandwidth. In the other direction (azimuth i.e., along-track direction), successive echoes acquired by the antenna over the same ocean scene are separated by their Doppler shift.

In the highest resolution mode (typical resolution at the surface of about 10 m), this acquisition is usually carried out in the so-called wave mode (WM) which combines a high resolution, small sized image (typical size of  $10 \times 10$  or  $20 \times 20$  km), and non-continuous sampling (every 100–200 km along the track)- the exact configuration depending on the mission.

The principles of wave spectra estimation from SAR observations are as follows.

Close to the range direction (across-track), the wave imaging process is the same as for a real aperture radar (RAR). Over the ocean, it is characterized by the modulation in backscatter due to the long wave induced varying surface tilt (local relative orientation) and straining (local roughness modulation). In that sense, the imaging of ocean waves by a very high-resolution radar instrument (SAR, RAR) is commonly described on the basis of a two-scale model: waves shorter than the resolution cell mostly contribute to the composite Bragg resonant backscattering mechanism, as they ride on a weakly random sea of much longer waves. The short waves (waves within the resolution cell) are only described through their statistical average properties (elevation and slope variances, elevation spectrum amplitude and directionality). These directly contribute to the wind-dependent mean radar cross section over the scene. The shortest components are usually wind-generated waves that overlay more deterministic modulating longer waves to produce measurable local contrasts. These observed spatial modulations of the backscatter intensity,  $\sigma_o(\underline{x})$  are supposed to be linear and small compared to the mean radar cross section,  $\sigma_o$ :

$$\sigma_o(\underline{x}) = \sigma_o \cdot \left[ 1 + \int \left( T(\underline{k}) \cdot z(\underline{k}) \cdot e^{j\left(\frac{k \cdot r - \omega_{|\underline{k}|} \cdot t}{\omega_{|\underline{k}|}}\right)} + c.c. \right) d\underline{k} \right] \quad (8)$$

where  $\xi(\underline{x}) = \int \left( z(\underline{k}) \cdot e^{j\left(\frac{k \cdot r - \omega_{|\underline{k}|} \cdot t}{\omega_{|\underline{k}|}}\right)} + c.c. \right) d\underline{k}$  is the surface elevation caused by the long waves,  $T$  is the modulation transfer function, and  $\omega_{|\underline{k}|}$  is the deep-water dispersion relation. The second term in the square brackets is the modulation of radar cross section which results from different factors contributing to the formation and/or the degradation of satellite SAR ocean wave images. Details on these imaging processes are given in Appendix 2. In the spaceborne configuration, the most important ones are those due to long-wave-induced varying surface tilt (tilt modulation), straining of short waves along long wave profiles (hydrodynamic modulation) and velocity bunching caused by the apparent shift in location due to scatterer motion on the surface. Depending on the motion scatter statistics, the velocity bunching mechanism is either a constructive or destructive imaging process so that it induces important nonlinearities between the image backscatter modulations and the wave slopes. This nonlinearity is characterized in the spectral domain by a cutoff in wavelength in the azimuth direction (along-track), which can be estimated from the image itself (see Appendix 2). This azimuth cutoff is governed by both the satellite  $R/V$  ratio ( $R$  being the distance and  $V$  the speed of the satellite), and the sea state and wind conditions. For typical spaceborne missions like Sentinel-1, the global average azimuth cutoff wavelength is around 220 m. In many cases, this limits the detectability of the wind-sea spectrum.

Hasselmann and Hasselmann (1991) and Krogstad (1992) proposed closed form expressions of the ocean-to-SAR spectral transform to relate the 2D Fourier transform of the SAR image to the 2D ocean wave spectrum. Different inversion algorithms were then developed (Engen et al. 1994; Hasselmann et al. 1996; Engen et al. 2000; Mastenbroek and de Valk 2000; Schulz-Stellenfleth 2005; Collard et al. 2005; Shao et al. 2015). Because of the nonlinear relationship between SAR spectra and wave spectra, such retrieval algorithms attempted to reconstruct the a priori ocean wave spectrum (first-guess estimation) by minimizing the difference between the theoretical SAR image spectra and the satellite observed SAR image spectra.

Breakthroughs were further introduced by Krogstad (1992) and Engen and Johnsen (1995) for the inversion of SAR images in wave spectra, with two innovations: (1) a way to separate the nonlinear and linear parts in the spectral domain and to approximate the nonlinear part with a filter function that can be estimated from the image itself (see Appendix 2), (2) a way to apply the inversion on image cross-spectra between two SAR single-look images (looking at the same ocean surface) instead of considering the Fourier transform of multi-look images. The advantage of this new method is first that it does not rely on a first guess estimate of the wave spectra as previously, and then that inversion applied on cross-spectra enables to minimize the speckle contribution and to remove the 180° ambiguity in the wave propagation direction.

This is the approach implemented in both the ASAR Envisat Wave Mode Level 2 and the Sentinel-1 WV Level 2 processors, where the nonlinear part of the Modulation Transfer Function (MTF) is estimated from a look-up table as a function of wind speed, wind direction and wave age (see Sentinel-1 Ocean swell wave spectra—OSW algorithm definition<sup>5</sup>).

In Fig. 5 are shown examples of SAR image cross-spectra simulated using the equations given in Appendix 2 for a given ocean wave spectra synthesized for a wind speed of 8.6 m/s at an angle of 45 degrees to the radar line-of-sight.

An example of the Sentinel-1B image cross-spectra and the derived SAR wave spectra is shown in Fig. 6.

To overcome the complex physical relationship between SAR images and wave spectra, several authors have proposed wave parameter estimation methods without explicit retrieval of wave spectra, but based on empirical models using either conventional multi-parameter least-square fit methods (Schulz-Stellenfleth et al. 2007) or neural network approaches (Stopa and Mouche 2017). Schultz-Stellenfleth et al. (2007) estimated 22 coefficients of a quadratic model function to estimate the significant wave height, mean period, and wave height associated with different spectral bands and wave power. These 22 parameters of the SAR image include the radar normalized cross section, the image variance, and 20 parameters computed from the SAR image variance spectrum using a set of orthonormal functions. Following this approach, Li et al. (2011) extended the method to analyze ENVISAT data and Romeiser et al. (2015) employed a similar method to estimate wave parameters from RADARSAT observations in tropical cyclones. Pleskachevsky et al. (2016, 2019) and Shao et al. (2015) developed parametric models which empirically relate SWH to both spectral and statistical properties of the image; mostly focusing on analysis of large-sized images in coastal zones from either the TerraSAR-X mission or from Sentinel-1 in wide swath mode.

<sup>5</sup> [https://sentinel.esa.int/documents/247904/4766226/S1-TN-MDA-52-7445\\_Sentinel-1%20Level%201%20Detailed%20Algorithm%20Definition\\_v2-4.pdf/83624863-6429-cfb8-2371-5c5ca82907b8](https://sentinel.esa.int/documents/247904/4766226/S1-TN-MDA-52-7445_Sentinel-1%20Level%201%20Detailed%20Algorithm%20Definition_v2-4.pdf/83624863-6429-cfb8-2371-5c5ca82907b8).



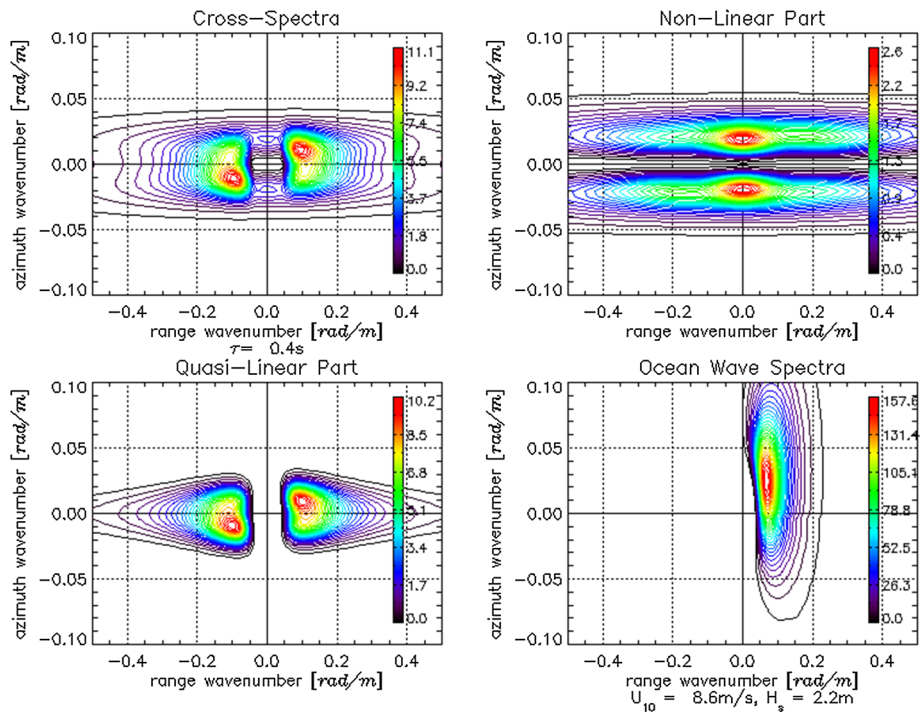


**Fig. 5** Upper left: SAR image cross-spectra,  $|P(\underline{k})|$ . Upper right: Nonlinear part of SAR image cross-spectra,  $|P_{\text{nl}}(\underline{k})| \equiv |P(\underline{k}) - P_{\text{ql}}(\underline{k})|$ . Lower left: Quasi-linear part of SAR image cross-spectra,  $|P_{\text{ql}}(\underline{k})|$ . Lower right: Ocean wave spectra,  $S(\underline{k})$ . See Appendix 2 for the definition of the different terms

Stopa and Mouche (2017) extended the idea of Schulz-Stellenfleth et al. (2007) by using a neural network method to empirically relate SAR image properties to SWH and wave periods. The neural network was trained using collocated data generated from the Wave-Watch III (WW3) numerical model (Ardhuin et al. 2010) and independently verified with observations from altimeters and buoys. They tested two approaches on Sentinel-1A images; in the first one, they decompose the shape of the image spectrum into orthogonal components, similar to what was proposed by Schultz-Stellenfleth et al. (2007). In the other one, they proposed the simplification of the parametric model by reducing the number of input parameters to 6 (normalized radar cross-section azimuth cutoff, normalized variance, skewness, peak wave length, and peak direction of the SAR image). A refinement of the first approach of Stopa and Mouche (2017) was also proposed by Quach et al. (2021) who used a neural network trained using altimeter SWH data. In an approach which is much more blind, a convolutional neural network was used by Sihan et al. (2020) to establish an empirical relationship between the SAR image (expressed as normalized radar cross) and SWH without needing to calculate feature parameters from SAR images.

All these methods currently remain at a relatively low (research) technology readiness level and do not replace the spectral inversion algorithms currently used by the Sentinel-1 SAR processing center to deliver operational products. However, the algorithm of Stopa and Mouche (2017) is implemented in the latest version of the Sentinel-1 Level 2 processor.

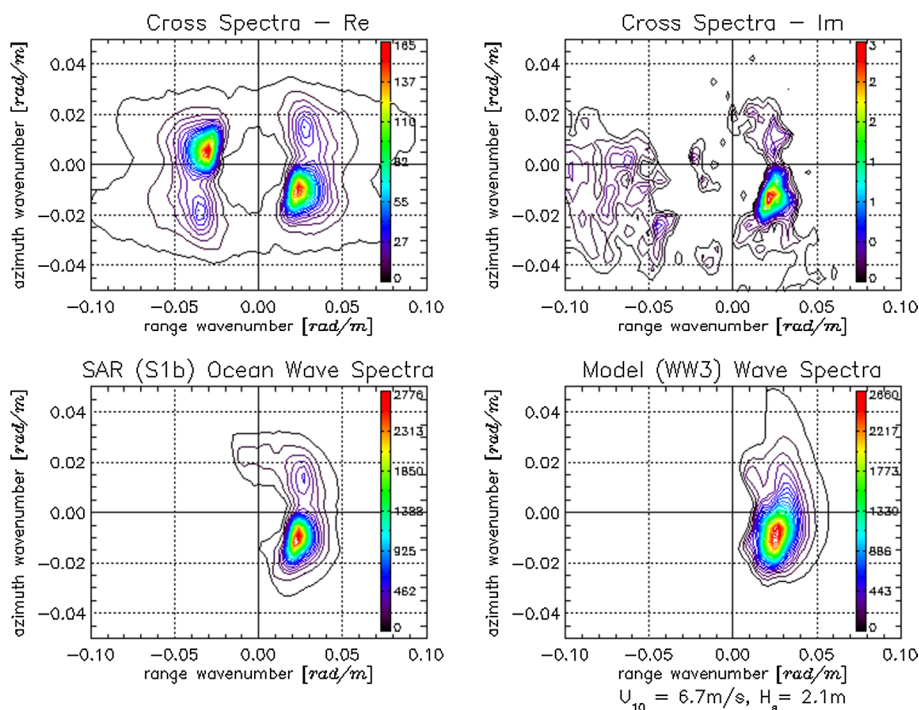


**Fig. 6** Upper left: Observed SAR (Sentinel 1-B) image cross-spectra—real part,  $\Re\{P_{SAR}\}$ . Upper right: Observed SAR image cross-spectra—imaginary part,  $\Im\{P_{SAR}\}$ . Lower left: Retrieved SAR ocean wave spectra,  $S$ . Lower right: Collocated Wave Watch III (WW3) model wave spectra. See Appendix 2 for details

## (2) Performance and Limitations

Starting with the ERS-1 mission, and continuing with the ENVISAT mission, as well as now with the Sentinel-1 missions, wave spectra are operationally provided over the open ocean thanks to imagettes collected with the so-called Wave Mode (called WM for ERS and ENVISAT or WV for Sentinel-1). With the Sentinel-1 mission, the so-called Stripmap mode is also compatible with the estimation of wave spectra.

For these missions, the wave spectra are estimated as explained above, using the quasi-linear inversion of image cross-spectra, combined with an empirical parameterization of the nonlinear term. Extensive geophysical validation of these ocean wave spectra has been performed from the Envisat ASAR WM instrument and currently from the Sentinel-1 WV instrument (Hadjuch et al. 2021). Considering the wave spectra within the spectral domain resolved by the SAR, the overall performance of the mean wave spectral parameters is listed in Table 4 for the two swaths of Sentinel-1 WV mode, where the reference is taken from hindcasts from WW3. Further validation of wave parameters based on cross-assignment of wave partitions between SAR wave spectra and WW3 spectra can be found in the ESA annual report (Hadjuch et al., 2021).

The scatterplots of effective SWH (i.e., significant wave height computed within the spectral domain resolved by the SAR) between Sentinel-1B and WW3 are shown in Fig. 7 for the two swaths of WV mode.

**Table 4** Performance of Sentinel-1b WV ocean wave spectra parameters with respect to WaveWatchIII

Wave spectra parameter	Bias	RMSE	Mean	Swath
Significant wave height	−0.03 m	0.4 m	1.5 m	wv1
Mean wave period	0.7 s	0.8 s	10 s	wv1
Mean wave direction	−0.7°	39°	—	wv1
Significant wave height	0.1 cm	0.5 m	1.5 m	wv2
Mean wave period	0.6 s	0.9 s	10 s	wv2
Mean wave direction	0.7°	35°	—	wv2

Number of spectra is 25 K globally distributed, and time period is one month. The parameters are computed within the spectral domain resolved by the SAR for both Sentinel-1 and WW3

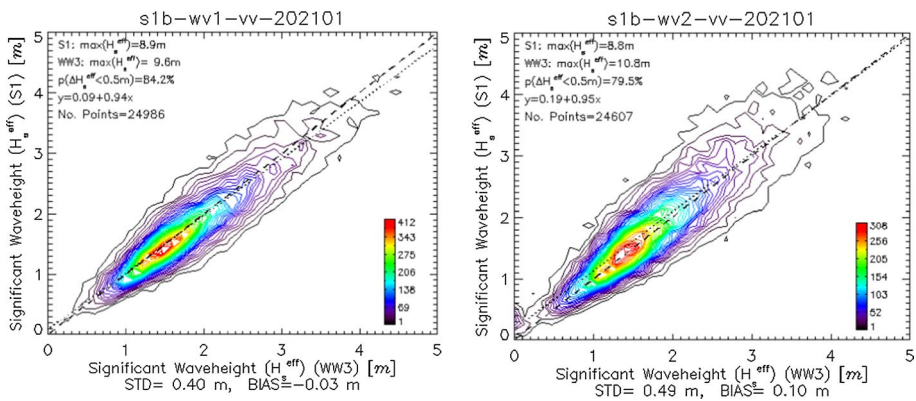


**Fig. 7** Scatterplot of effective significant wave height obtained from Sentinel-1b WV wave spectra versus that obtained from the WAVEWATCH III numerical wave model. Left: Swath WV1, Right: Swath WV2. These histograms were obtained from one month of global data (January 2021)

Because systematic SAR acquisition in a specific wave mode is mainly switched-on away from the coastal zone, results on the assessment of SAR wave spectra or wave parameters based on in situ buoy observations are relatively scarce. However, using the method initially developed by Collard et al. (2009), Wang et al. (2022) were able to assess the significant wave height of the swell part with buoy data. This research was undertaken using the so-called “fireworks technique,” which consists of propagating the swell properties extracted from the SAR spectra back toward the swell generating zone (gathering all the swell measurements originating from the same storm event) and then forward in time along their propagation path, until swell reaches the coast. This method allows a significant increase in the spatial and temporal collocations with in situ reference data. However, it is limited to assessing swell wave heights and relies on some physical assumptions such as neglecting wave-current interactions. Figure 8, taken from Wang et al. (2022), illustrates the results obtained using this method with a 4-year database of Sentinel-1A/B observations. A bias and RMSE of 0.18 m and 0.5 m were reported in this comparison, and a similar positive bias was found when the same approach was used but with the WW3 model as the reference. Overall, the method allowed Wang et al. (2022) to propose an empirical correction on the estimation of the swell wave height from the Sentinel-1 SAR WM.

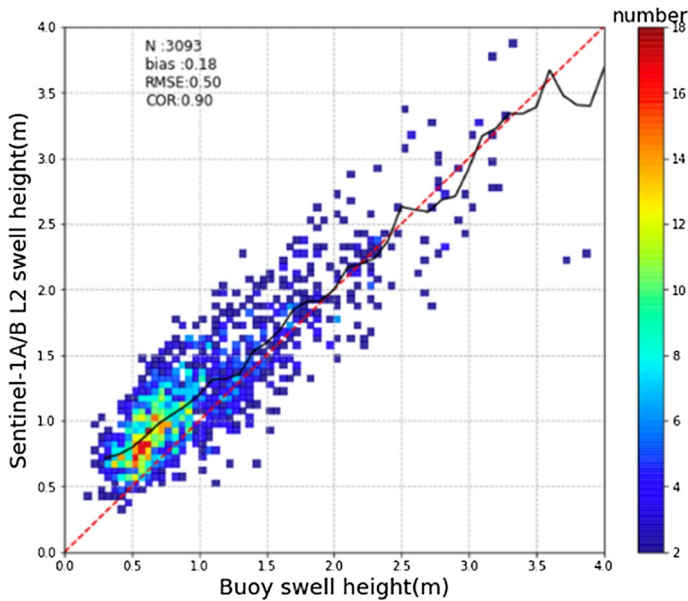


**Fig. 8** Significant wave height of the swell part estimated from for S-1A/B against buoy data, with collocations based on the “fireworks technique.” The data set includes about 4 years of data (2016–2020)—From Wang et al. 2022

Concerning methods that are not based on a spectral inversion technique, one can cite the results of Stopa and Mouche (2017) who showed that their methods provide reasonable accuracy on SWH, for conditions up to 13 m (bias less than 0.25 m, RMSE from 0.50 to 0.70 m depending on the control data set and number of input variables). Results on the wave periods are also promising, although the authors mention that more work is still necessary to improve the empirical model. According to Quach et al. (2021), SWH was obtained from SAR Sentinel-1 observations with 0.3-m RMSE relative to independent altimeter observations.

In parallel to the systematic validation of SAR wave products, experiments on assimilating SAR wave spectral parameters into numerical wave model show a positive impact on the model output (see Sect. 3.1.1 and e.g., Abdalla et al. 2010; Aouf et al. 2012; Aouf et al. 2021).

**2.2.4.3 Surface Current from SAR** Synoptic maps of ocean surface wind, waves and current from space are important inputs to better characterization and parameterization of oceanic mesoscale and sub-mesoscale dynamics, as well as in support of advances in ocean–atmosphere research and modeling activities (Bourassa et al. 2019). In coastal ocean areas, the current is usually measured from in situ surface drifters (Lagrangian), fixed moorings (Eulerian) using acoustic Doppler Current Profilers (ADCP) or land-based High Frequency (HF) radar (see Ardhuin et al. 2009a; Röhrs et al. 2015). However, these measurements are irregular in space and time, with coverage only over a limited area, yielding observation gaps. Spaceborne SAR missions such as TerraSAR-X (Romeiser et al. 2010), Tandem-X (Romeiser et al. 2014), Envisat (Chapron et al. 2005;

Johannessen et al. 2008) and Sentinel-1 (Moiseev et al. 2020a, b) have shown the capability to provide measurements of the radial component of Lagrangian mean velocity vector.

The phase information in the ocean backscatter recorded with a SAR can be used to obtain radial velocity, which has been shown to provide valuable information on the near surface wind speed and ocean surface current. Two techniques are used to derive the radial velocity from SAR measurements; the Along-Track Interferometry (ATI) and the Doppler Centroid frequency (DC).

### (1) Concept of Along-Track Interferometry (ATI)

The concept of the Along-Track Interferometry (ATI) technique is to measure the received phase signal difference between two SAR observations of the same surface shifted in space or time or both. The space or time shift is called the baseline. In ATI, this is achieved by measuring the phase difference between two complex SAR images (master ( $I_M$ ) and slave ( $I_S$ )) acquired near simultaneously with a physical baseline separating the two antennas along track. In order to preserve coherency between these two ocean images, the baseline or equivalently the time shift must be small, i.e. less than 200 m or 0.03 s, respectively. For an ideal ATI system, the phase difference  $\Delta\phi$  can be achieved from the product of the two complex SAR images and expressed as:

$$\begin{aligned}\Delta\phi(\underline{x}, t + \Delta t) &= \arg \{ I_M(\underline{x}, t) I_S^*(\underline{x}, t + \Delta t) \} \\ &= 2\pi f_{dc} \cdot \Delta t = n \underline{k}_r \cdot \Delta \underline{V} \cdot \frac{B_{\parallel}}{V_s} \\ &= n \underline{k}_r \cdot \underline{V}_s \cdot \frac{B_{\parallel}}{V_s} - n \underline{k}_r \cdot \underline{U} \cdot \frac{B_{\parallel}}{V_s}\end{aligned}\quad (9)$$

where  $\Delta t$  is the time shift between observations of master and slave,  $f_{dc}$  is the Doppler frequency,  $\Delta \underline{V} = \underline{V}_s - \underline{U}$  is the relative velocity vector between satellite and moving scatterer,  $B_{\parallel}$  is the along-track baseline,  $\underline{V}_s$  is the satellite velocity vector,  $\underline{U}$  is the surface scatterer velocity vector,  $\underline{k}_r$  is the radar wavenumber vector, and  $n = 1$  for a bistatic case and  $n = 2$  for a monostatic case. The first term on the right-hand side of the last line of Eq. (9) is the orbit/attitude term (i.e., geometric), while the second term is the geophysical contribution caused by the motion of scatterer on the surface. We shall later see that the geophysical term consists of an artifact velocity of the imaging process, and a genuine velocity from the Lagrangian mean surface current.

### (2) Concept of Doppler Centroid Anomaly (DCA)

The concept of the Doppler Centroid Anomaly (DCA) technique is to estimate the Doppler Centroid (DC) frequency from the azimuth spectra of a single-look complex (SLC) SAR image (or from complex raw SAR data) (Bamler 1991; Engen and Johnsen 2015). For high-resolution DC estimates, it is recommended to use SLC data to avoid biases caused by variations in intensity within the estimation area. The estimated DC can be expressed as:

$$f_{dc} = \frac{1}{\pi} \underline{k}_r \cdot \underline{V}_s - \frac{1}{\pi} \underline{k}_r \cdot \underline{U} + f_{dc}^{\text{ant}}(\beta) \quad (10)$$

where  $f_{dc}^{ant}$  is the contribution from the antenna electronic mispointing depending on the off-boresight angle ( $\beta$ ), while the two other terms on the right-hand side of Eq. (10) are the same as for the ATI. The second term on the right-hand side of Eq. (10) is called the Doppler Centroid Anomaly (DCA) and represents the geophysical contribution to the estimated DC. As for the ATI, the geophysical term contains an artifact velocity caused by the imaging process, and a genuine velocity from the Lagrangian mean surface current. In that sense, the ATI and the DCA techniques measure the same geophysical quantity, but the contributions from system effects differs in general. This has recently been demonstrated by comparing Sentinel-1 and Tandem-X surface velocity measurements (Elyouncha et al. 2022).

### (3) Surface Current Retrieval

Equations (9) and (10) show that the DC frequency, or the ATI phase recorded over the ocean, differ from the values predicted by satellite orbit/attitude and antenna electronics. These differences in DC or ATI phase are a direct measure of the line-of-sight (radial) velocity of the moving scatterer on the ocean surface. They are thus sensitive to surface currents induced by wind drift (Ekman), ocean waves (Stokes drift), tides (tidal) and ocean topography (geostrophic). Unfortunately, to a first order, the geophysical DCA and ATI signals are both governed by an artificial velocity (the so-called wind/wave DC bias), which in many cases obscures the underlying true Lagrangian mean surface current velocity.

Any retrieval of the underlying ocean surface current from DCA or ATI measurements requires the prediction and removal of the wind/wave DC bias (Chapron et al. 2005) from the geophysical signal. The most commonly used approach is to neglect any wind/wave/current interaction and predict and remove the wind/wave DC bias from the measured DCA followed by converting the residual DCA to a line-of-sight current velocity projected to ground range:

$$v_{gr} = \frac{-\pi}{k_r \sin \theta} (f_{dca} - f_{dc}^{bias}(\underline{U}_{10}, H_s; \theta)) \quad (11)$$

where  $f_{dc}^{bias}$  is the wind/wave DC bias parameterized to show its dependency on wind, wave and imaging geometry. There exist both physical-based models for  $f_{dc}^{bias}$  (Chapron et al. 2005; Johannessen et al. 2008; Romeiser and Thompson 2000; Pedersen et al. 2005; Said et al. 2015; Mouche et al. 2008) and empirical ones (Mouche et al. 2012; Moiseev et al. 2020a b; Moiseev et al. 2022).

The model of Chapron et al. (2005) interprets the net velocity induced by the near-surface wind as the mean line-of-sight velocity that the radar-detected scatter elements feel when riding on the longer waves. As the scatter elements are tilted by longer waves, the NRCS varies along the wave profiles due to modulation effects (tilt- and hydrodynamic), leading to correlation with horizontal and vertical orbital velocities. These modulation effects are elegantly formulated by expressing the wind/wave DC bias as:

$$f_{dc}^{bias} = \frac{k_r}{\pi} \frac{\langle (u \sin \theta_i - w \cos \theta_i) \sigma_o(\theta_i + \Delta \theta_i) \rangle}{\langle \sigma_o(\theta_i + \Delta \theta_i) \rangle} \quad (12)$$

where  $k_r$  is the radar wavenumber,  $u$  and  $w$  are the horizontal and vertical velocities,  $\sigma_o$  is the NRCS,  $\theta_i$  is the local radar beam incidence angle,  $\Delta \theta_i$  represents the effect on  $\theta_i$  due to local tilt induced by the longer waves and the brackets stand for mean values. We note



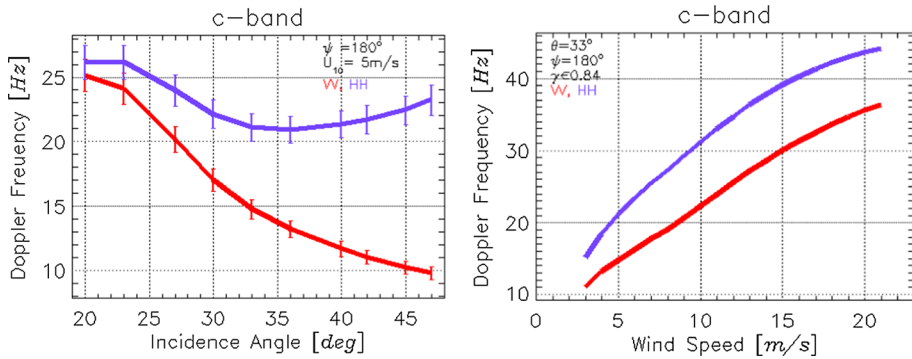


**Fig. 9** Left: Simulated Doppler centroid anomaly (DCA)  $f_{dc}^{\text{bias}}$  (in Hz) as function of incidence angle for VV (red) and HH (blue) polarizations. The wind speed is fixed at 5 m/s and the radar look direction is upwind. The vertical bars reflect the variation in DCA with a change in wave age of 10%. Right: Simulated DCA as function of wind speed for VV (red) and HH (blue) polarizations at an incidence angle of 33 degrees. The radar look direction is supposed to be upwind

from Eq. (12) that the DCA model implicitly requires a backscatter ( $\sigma_o$ ) model. Several backscattering models have been applied in the literature to support SAR Doppler analysis (Johannessen et al. 2008; Romeiser and Thompson 2000; Said et al. 2015, Mouche et al. 2008). It is basically through the backscatter modulation that the polarization and incidence angle dependencies enter into the expression for the wind/wave DC bias.

Despite the potential of SAR to measure ocean surface currents, there are limitations and several challenges related to the utilization of DCA and ATI measurements such as:

- The dynamic range of DCA is relatively small ( $\pm 60\text{Hz}$ ).
- The DC contributions from antenna and satellite attitude/orbit are difficult to predict to the required accuracy, and the signal may obscure the geophysical signal.
- Accurate calibration of the DC and ATI signal is difficult for open ocean areas.
- The ATI phase coherence limits the available range of along-track baseline (Zebker and Villasenor 1992; Engen and Johnsen 2015).
- The DCA and the ATI are biased by the apparent velocity signal from surface waves (the so-called wind/wave DC bias). This signal is often much larger than the mean Lagrangian surface current signal.
- A geophysical model function (GMF) is required, which precisely describes the geophysical processes that contribute to the measured DCA or ATI.
- The DCA from a mono-static SAR or the phase from an ATI system provides only a line-of-sight component of the surface velocity field.

User requirements on the surface current are stringent, with a relative performance error of 0.1 m/s and a dynamic range of 0.1–5 m/s at a resolution down to  $5 \text{ km}^2$  (see requirements from WMO<sup>6</sup>). It is thus mandatory to have a good GMF to predict the wind/wave DC bias, and very precise estimates of local wind vector and the sea state.

<sup>6</sup> [https://space.oscar.wmo.int/variables/view/ocean\\_surface\\_currents\\_vector](https://space.oscar.wmo.int/variables/view/ocean_surface_currents_vector).



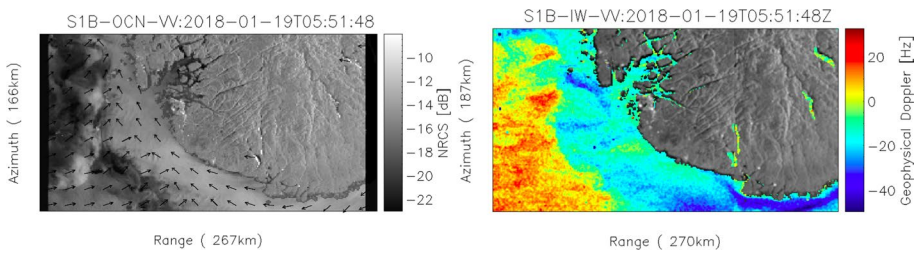


**Fig. 10** Left: intensity image from the S1-B in the Interferometric Wide Mode acquired at south-west coast of Norway; overlaid is the wind direction (black arrows). Right: Doppler centroid anomaly from the same data take, showing the signature of the wind front on the left side of the image and the Norwegian Coastal current in the lower right part of the image. The size of the image is 267 km × 166 km

The dependency of the DCA on the imaging geometry, polarization, wind field and sea state are shown in Fig. 9. Figure 10 shows images of NRCS and DCA as measured by Sentinel-1 in the interferometric wide swath mode with clear signatures of the wind/wave DC bias and the underlying mean Lagrangian surface current.

**2.2.4.4 Wind from SAR** To date, the only official and operational ocean surface wind product is part of the ESA/Copernicus Sentinel-1 C-band SAR product family. This Level 2 (L2) ocean product also includes ocean waves (see 2.2.4.2) and radial surface velocity measurements (see 2.2.4.3.2). All Sentinel-1 scenes acquired over the ocean are processed into the Level-2 Ocean product and disseminated through the Copernicus hub.<sup>7</sup>

As defined, the only parameter used in the wind algorithm of ESA to inverse the SAR signal into an ocean surface wind field is the measured NRCS in co-polarization (VV or HH). In fact, this approach is directly derived from scatterometry (see Sect. 2.2.2) and relies on GMF between the NRCS and surface wind speed and direction. However, the SAR instruments and mission peculiarities are very different from those of scatterometers, yielding other challenges in order to estimate the two ocean wind vector components (speed and direction). Existing SARs have one single antenna pointing in the satellite across-track direction. This means that there is only one viewing angle per wind vector cell (WVC), i.e., one single NRCS measurement in co-polarization whereas the GMF depends both on the wind speed and direction, leading to an under-constrained inverse problem. For operational purposes, the usual approach is to use the wind direction from a NWP model to further constrain the wind inversion. In the existing L2 Ocean product, this method relies on a Bayesian approach from Portabella et al. (2002) to merge the NRCS information computed at 1 km and the wind vector from the NWP interpolated at 1 km. The cost function is thus:

$$J(U_{10}, \theta) = \left[ \frac{\sigma_0^{pp} - \text{GMF}^{pp}(U_{10}, \theta)}{\Delta \sigma_0^{pp}} \right]^2 + \left[ \frac{U_{10}^{\text{NWP}} - U_{10}}{\Delta U_{10}^{\text{NWP}}} \right]^2 \quad (13)$$

With  $U_{10}^{\text{NWP}}$  the a priori wind field associated to  $\Delta U_{10}^{\text{NWP}}$  error, and  $\Delta \sigma_0^{pp}$  the NRCS error (pp is the index for the SAR polarization condition).

<sup>7</sup> see <https://sentinels.copernicus.eu/web/sentinel/missions/sentinel-1/data-products>.

The way forward is to derive the wind speed and direction from the radar-measured quantities by adding constraints to the inversion scheme in order to minimize the use of ancillary wind from NWP. To this aim, two families of approaches exist, based on the idea that SAR provides much more information than just NRCS in co-polarization at 1 km resolution.

The first approach is to rely on the analysis of the NRCS at high resolution (tens or hundreds of meters) to detect features aligned with the wind direction, and use them instead of, or in conjunction with, the NWP information. Several methods have been tested, including wavelet analysis (Du et al. 2002; Zechetto 2018], local gradients (Koch 2004; Zhou et al. 2017) and Fourier analysis (Gerling 1986). This approach mainly assumes that rolls are organized in the marine atmospheric boundary layer along with the wind direction. However, there have been several sets of evidence showing that the rolls and the wind are not aligned. Moreover, there are situations when they cannot be detected in the SAR image (Wang et al. 2020) and/or do not exist in the marine atmospheric boundary layer, preventing any wind direction estimate. For example, depending on the atmospheric stability, the dominant atmospheric signature can be linked to convective cells (Stopa et al. 2022). Convolution neural networks have also recently been used to capture the relationship between wind direction and textures in the SAR image, possibly including patterns that are different and more complex than streaky patterns of the roll signatures.

- The second approach is to rely on other radar parameters to constrain the wind inversion. The proposed methods use one of the following information:
- Geophysical Doppler information in co-polarization: the geophysical Doppler anomaly (see (2)) has a dominant component from the local sea-state at C-Band with a dependency to the wind-sea direction complementary to the NRCS. Based on a GMF which relates Doppler anomaly to wind speed and direction as a proxy for the local sea-state, Mouche et al. (2012) demonstrated how the geophysical Doppler signature derived from Envisat/ASAR helps to constrain the wind direction retrieval, leading to a more realistic wind field in complex situations such as low-pressure systems or atmospheric fronts. However, as explained in the previous section, the Doppler anomaly is also impacted by other geophysical phenomena than just the local wind sea, such as the underlying ocean surface current (Chapron et al. 2005) or waves (Moiseev et al. 2020a, b) not in equilibrium with the surface wind. Taking into account the impact of such phenomena on the Doppler anomaly is still an active domain of investigation.
- Normalized radar cross section in cross-polarization: the strong relationship between the cross-polarization NRCS and the wind speed has been demonstrated with Radar-SAT-2 with images acquired over buoys in quad-polarization by Vachon and Wolfe (2011). In particular, the wind direction dependency was found to be weaker than in co-polarization and the wind speed dependency stronger. This led Zhang and Perrie (2012) to propose using this new cross-polarized channel for wind speed estimate in Tropical Cyclones with Sentinel-1 and Radarsat-2 SAR. Mouche et al. (2017) further suggested combining the two channels (co- and cross-polarized) to take advantage of their complementary characteristics; the co-polarization NRCS being more efficient at low wind speeds while the cross-polarization NRCS takes over for high wind speeds when its signal-to-noise ratio becomes significant. This allowed the first estimate of ocean surface wind speed from space at high resolution in the vortex of category-5 hurricanes (Mouche et al. 2019).

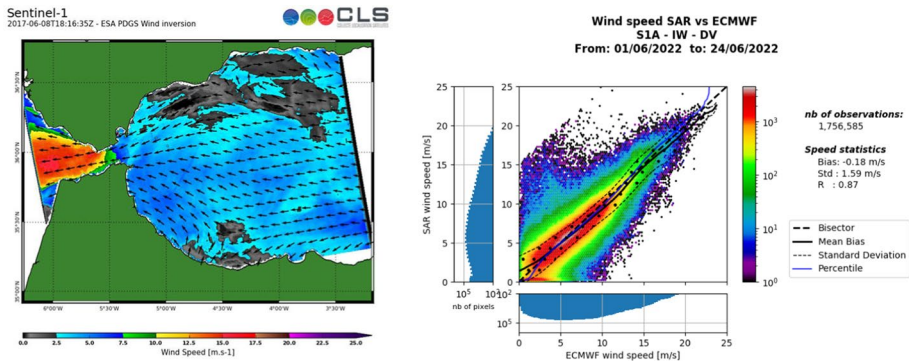


**Fig. 11** **a** Surface Wind measurement field from SAR -Sentinel-1 observations on June 8th 2017, over the Strait of Gibraltar. From ESA website <https://sentinels.copernicus.eu/web/sentinel/user-guides/sentinel-1-sar/product-types-processing-levels/level-2>. **b**: density plot of SAR vs ECMWF reanalysis wind speed by Sentinel 1A ESA L2 products in polarization VV and acquisition mode Interferometric Wide Swath from June 1st 2022–June 24th 2022. Courtesy of Charles Peureux

- Co-and-cross-phase coherence (CCPC): the relationship between the CCPC computed from VV and VH channels and the wind direction has been presented by Zhang et al. (2012) with Radarsat-2 and then further documented with respect to wind speed and direction by Longepe et al. (2021). In particular, an odd and significant azimuthal modulation has been found, increasing with both wind speed and incidence angle. Translated into a GMF, this opens perspectives for including this new radar parameter in the cost function to constrain the wind field retrieval.
- SAR image cross-spectrum of wind-driven waves : with the improved spatial resolution, recent SAR such as Sentinel-1 can now detect short-scale wind-waves (in equilibrium with the wind) signature. Li et al. (2019) proposed a method (called MACS for MeAn Cross-Spectra) based on the filtering of SAR image cross-spectra in the range of wavelengths between 15 and 20 m allowing to capture both the radar cross-section variability and its time evolution. Thanks to the contribution of intermediate waves, Li et al. (2019) showed that this spectral information is sensitive to wind speed and direction. In particular, the sign of the imaginary part of MACS (IMACS) is considered as a promising criterion to reduce the wind direction ambiguity in the inversion of high-resolution wind fields from SAR imagery.

### Performance and limitations

Figure 11a shows an example of wind field retrieval in a region of variable wind (Mediterranean Sea, Gulf of Gibraltar). Figure 11b shows a statistical comparison of winds derived from the SAR of Sentinel-1A in the interferometric wide swath mode, against winds from the ECMWF analysis, obtained over 24 days of June 2022. The bias is small ( $\sim 0.18$  m/s) and the standard deviation slightly larger than that from scatterometer winds. Note that performance is seasonal; typically, the mean bias oscillates around 0.1 m/s with a  $\pm 0.25$  m/s amplitude, and the root mean square difference oscillates around 1.6 m/s with a  $\pm 0.2$  m/s amplitude.

## 2.2.5 Near-Nadir Scatterometry

**2.2.5.1 History and Evolution** The choice of a near-nadir looking real-aperture configuration was proposed in the 1990s to measure directional spectra of ocean waves (Jackson 1981; Jackson et al. 1985a) as an alternative approach to that based on SAR-images. A space-borne concept with one rotating antenna at near-nadir incidence was proposed by Jackson et al. (1985a), but not implemented in space at that time. Later in the 2000s, the same concept with a rotating antenna at  $10^\circ$  incidence was combined with a nadir measurement (Hauser et al. 2001). Finally, this real-aperture rotating concept was selected for the CFOSAT mission with the surface wave investigation and monitoring (SWIM) instrument combining five off-nadir beams (around approximately  $2^\circ$ ,  $4^\circ$ ,  $6^\circ$ ,  $8^\circ$ , and  $10^\circ$  incidence) and one nadir-beam. The novelty of this mission is also that it provides ocean measurements of the significant wave height, the full directional wave spectra with wavelengths in the range of about [30, 500] m and the associated dominant directions and wavelengths.

The same kind of geometry (near-nadir incidence, scanning geometry) with an additional Doppler capability was also proposed for the SKIM project proposed for the Earth Explorer 10 mission (but not selected).

**2.2.5.2 Principle of Wave Measurements** The main idea is that at near-nadir incidence (typically around  $8\text{--}10^\circ$  from nadir), the normalized radar cross section is sensitive to the local slopes of the sea surface, but almost insensitive to small-scale roughness effects produced by the wind, and to hydrodynamic modulations resulting from interactions between short and long waves. Hence, in absence of image degradation as encountered with SAR systems (see Sect. 2.2.4.2), and thanks to the filtering induced by the choice of a large footprint in azimuth (i.e., much larger than the typical scale of the long waves), the modulations of the normalized radar cross section can be linearly related to the slope of the long-waves which propagate along the look direction. The amplitude of these modulations is maximum when the antenna looks in the direction aligned with the wave propagation direction. At angles close to  $8^\circ\text{--}10^\circ$  incidence this modulation is to the first order proportional to the slopes of the long waves. This means that the wave slope spectra are linearly related to the signal modulation spectra (after speckle correction and system response is taken into account). The  $360^\circ$  azimuth scanning then enables a construction of the full directional spectrum.

Details on the theoretical basis of this concept can be found in Jackson (1981), Jackson et al. (1985a, b). Hauser et al. (2017) presented the principle of wave spectra inversion in the configuration of SWIM, whereas a first validation based on the initial data sets processed from SWIM observations is discussed in Hauser et al. (2021).

**2.2.5.3 Performance and Limitations** Since CFOSAT is so recent, its performance still needs to be evaluated in detail after accumulating a sufficient quantity of collocated observations; however, an initial evaluation of SWIM measurements is presented in Hauser et al. (2021). For SWH from nadir, before any correction for cross-calibration with other missions, the bias with respect to Jason-3 was found to be very small (less than 1 cm) with a standard deviation of 0.35 m. As for the wave spectral parameters, Hauser et al. (2021) showed, using a comparison to model data, that the best configuration of SWIM measurements is from the  $10^\circ$  beam, as it minimizes the speckle effect and the possible non-homogeneities of the backscatter coefficient within the footprint. For this  $10^\circ$  beam configuration, Haoyu et al., (2021) established that, compared to buoy observations, SWIM can provide the spectral peaks of the main partitions with a RMSE of 0.9 s and  $20^\circ$  for the peak period (converted

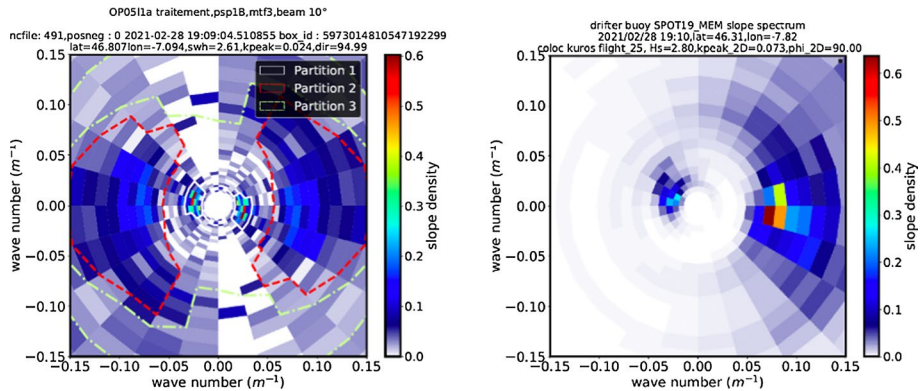


**Fig. 12** Example of a 2D wave slope spectra (energy density as a function of the wave number of the waves in a polar plot representation) obtained from SWIM **a** compared to a spectrum estimated from a collocated Spotter buoy **b**. The data set was obtained in the Bay of Biscay on February 28th, 2021. In (a)-left plot- the  $180^\circ$  ambiguity in the propagation direction is not removed. This case corresponds to mixed sea conditions with swell and wind sea propagating in opposite directions. The significant wave height is of about 2.1 m. The contours in Fig. 12 **a** display the wave spectrum partitions extracted from the SWIM data (first partition with white contours, second partition with red contours)

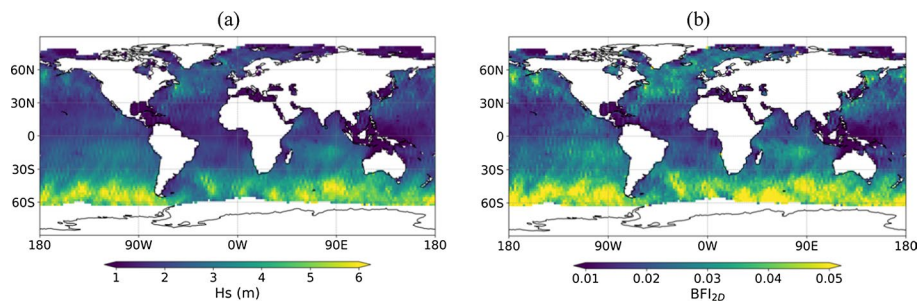


**Fig. 13** Maps of **a** significant wave height and **b** Benjamin-Feir Index as estimated from the SWIM wave spectra measurements—The parameters are estimated as averaged values of the month of September 2022. Courtesy of E. Le Merle

from the peak wavelength) and peak direction, respectively. Ying et al. (2022) also show that the mean omni-directional spectra derived from the  $10^\circ$  incidence beam of SWIM compare very well with mean spectra from buoys, with a correlation coefficient above 0.90 for conditions with significant wave height greater than 2 m in cases of swell and greater than 2.5 m in cases of wind sea. In the other conditions, the reduction in correlation is attributed to weak nonlinear effects due to range bunching (especially for observations from the  $6^\circ$  beam and young wind sea) or to parasitic peaks at low wavenumbers due to the amplification of the remaining speckle noise.

Figures 12 and 13 illustrate typical results obtained with SWIM. In Fig. 12 an example of a directional wave spectrum is shown and compared to a spectrum obtained from collocated buoy measurements. This case illustrates the capacity of SWIM observations to provide the directional properties of the ocean waves. Figure 13 shows an example of maps of two parameters estimated from SWIM observations collected over 13 days: the significant wave height and the Benjamin-Feir index (BFI, a parameter defined by Janssen and Bidlot



2009 and Mori et al. 2011) to characterize the probability of occurrence of extreme waves). The BFI combines three parameters, which have been estimated with the SWIM wave spectra: the significant slope (ratio of significant wave height to dominant wavelength), the directional spread and the peakedness of the wave spectra in the frequency domain. As such, Fig. 13 presents the first map of BFI index ever derived from space-borne measurements and shows the potential of these CFOSAT observations.

**2.2.5.4 Surface Velocity Measurements** Measurement of the centroid Doppler shift in the back-scattered echoes of a SWIM-like instrument can also provide an estimate of near-surface ocean velocities, as demonstrated with airborne observations by Marié et al. (2020). As described for SAR systems in Sect. 2.2.4, these velocities are identical to, but noisier than those provided by across-track interferometric systems that require more complex setups (Romeiser et al. 2014). Compared to typical SAR systems, near-nadir incidence angles are better suited for applying the Kirchhoff approximation, and this gives a Doppler velocity as the ratio of the mean slope velocity and an effective mean square slope that is a function of the radar frequency (Nouguier et al. 2018). This means that the Doppler velocity is a vector sum of a wave-induced Doppler that arises from the correlations of slopes and line-of-sight velocities, and the near-surface current that comes into the dispersion relation of all the waves that contribute to the slope spectrum. For average wind and wave conditions, the magnitude of the wave-induced Doppler is of the order of 2.6 and 2.2 m/s for Ku- and Ka-band respectively (Marié et al. 2020). Given the broad range of wavelengths that contribute to the mean square slope, the current measurement, which is obtained by subtracting the wave-induced Doppler from the measured Doppler velocity, is a convolution of the current profile over the top two meters. A next-generation SWIM-like instrument with Doppler measurements capability could therefore provide the projection of the near-surface current on the measurement azimuth, with the current vector obtained by combining different azimuths (Ardhuin et al. 2019a). The current measurement is generally improved by measuring waves as short as 30 m, hence resolving most of the spectral components that contribute to the surface Stokes drift. Such a concept has been a focus for the global mapping of mesoscale currents and Stokes drift (ESA 2019).

## 2.2.6 Recent Trends and Perspectives

Satellites form an essential part of the global observing system to both measure and monitor surface wind, waves and currents for scientific and operational applications, however several important aspects still remain beyond the capability of today sensors. Moreover, a number of grand challenges exist in integrating the knowledge acquired by earth observation into earth system models.

The first limitation of present satellite capability relates to temporal sampling. Contrary to most ocean variables, winds and waves are rapidly evolving phenomena, where conditions can change markedly in a matter of hours. While the global coverage, spatial resolution and accuracy of satellite observations offer satisfactory capability for the measurement of waves, the temporal sampling of ocean winds remains inadequate. User surveys frequently highlight requirements for hourly to sub-hourly observations (WMO<sup>8</sup>) driven by various operational and scientific imperatives (diurnal variability, hurricane dynamics,

<sup>8</sup> <https://space.oscar.wmo.int/variables/>.

mesoscale wind systems, NWP requirements, etc.). This need for more frequent wind observations has stimulated the development of “New Space” solutions like GNSS-Reflectometry, which exploits bi-statically reflected signals of opportunity from Global Navigational Satellite Systems like GPS and Galileo to derive information about the Earth’s surface. GNSS-R for ocean winds was successfully demonstrated on board the UK TechDemoSat-1 mission (Foti et al. 2015; Unwin et al. 2016) and later with the NASA CYGNSS constellation (Ruf et al. 2018). Recent research revealed the critical importance of GNSS-R calibration to account for instrument and platform effects linked to the bistatic scattering geometry, platform attitude and spatial and temporal changes in GNSS direct power levels (Hammond et al. 2020). Once calibrated, GNSS-Reflectometry can provide valuable wind speed information (RMSE  $\sim 2$  m/s for winds  $< 20$  m/s) with successful examples also of hurricane winds observed with TechDemoSat-1 (Foti et al. 2017) and CYGNSS (Saïd et al. 2021). GNSS-R is relevant also to Earth Observation applications such as soil moisture, freeze–thaw state over permafrost, inundation and wetland mapping and above-ground biomass that are the primary objectives of ESA’s second Scout mission, HydroGNSS, due for launch in 2024 (Unwin et al. 2021). The use of navigation signals of opportunity and multi-platform, multi-static, sensing to address multiple monitoring needs presents GNSS-Reflectometry as a paradigm shift for Earth Observation.

The second limitation of present satellite capability relates to the growing recognition of the fundamental role in the global Earth System of wind/wave/current interactions and ocean surface dynamics at scales below 10 km (Lapeyre and Klein 2006; Lévy et al. 2012; Klein et al. 2019; Villas Bôas et al. 2019; D’Asaro et al. 2020). High-resolution satellite images of sea surface temperature and ocean color reveal an abundance of ocean fronts, vortices, swirls, and filaments at horizontal scales less than 10 km that permeate the global ocean, especially near mesoscale jets and eddies, in coastal seas and close to sea ice margins. These sub-mesoscale phenomena are associated with intense vertical ocean velocities—orders of magnitude greater than average—that connect the turbulent air-sea boundary layer and the ocean interior. Small scales also mediate exchanges between the land, the ocean and the cryosphere, with intense and highly variable processes that support strong interactions not just with the atmosphere, but also with coastlines, underwater bathymetry or sea ice. These small-scale phenomena shape condition the pathways, dispersion and lateral transports of terrestrial freshwater, nutrients, oil, plastics and other pollutants, which are highly relevant to natural habitats, the economy and society. To date, single satellite sensors cannot provide the comprehensive observations of surface winds, waves and currents needed to make progress. SEASTAR is a new mission concept based on three-beam along-track SAR interferometry (Gommenginger et al. 2019) that proposes the delivery of high-quality, high-resolution imaging of two-dimensional surface current and wind vector fields, as well as directional wave spectra to observe and quantify these fast-evolving processes on daily to multi-annual scales, across different ocean conditions and latitudes, in order to confront models and support research on submesoscale dynamics, vertical processes and wind-current-wave interactions in coastal, shelf- and ice-covered seas.

In addition to the exploitation of satellite missions with a primary objective of ocean monitoring, opportunities offered by other missions are being explored and new applications of these datasets proposed. For example, Kudryavstev et al. (2017a) show that detailed information of surface ocean waves can be obtained from the Copernicus Sentinel-2 multi-spectral instrument (MSI) measurements. Although this mission is dedicated to land surface mapping, in coastal regions MSI can provide the directional spectra of ocean surface waves with a high spatial resolution under particular conditions (cloud-free areas, and appropriate geometrical configuration between the sun, the sensor, and the ocean wave



field) based on modulations due to waves in the surface brightness data from optical multi-channel images in the sun glitter area. This has been further exploited by Kudryavstev et al. (2017b) with the analysis of wave transformation (wave/current interaction) in the Agulhas current region. Using the information provided by the multi-channel configuration (observations of the same area separated in time by about 1 s), Yurovskaya et al. (2019) have also demonstrated the potential of these Sentinel-2 observations to estimate the surface currents at small scales without any assumption on the geostrophic nature of these currents. Another interesting development is in the estimation of surface wave properties from the Ice, Cloud, and land Elevation Satellite 2 (ICESat-2). Indeed, this satellite provides high-resolution height estimates of the Earth's surface from a photon counting LiDAR instrument onboard that collects data over various surfaces including open ocean and marginal ice zones. Klotz et al. (2020) show that under particular conditions (waves more or less aligned with the satellite track), the estimate of dominant wavelength and significant wave height from the analysis of height variations along the track is consistent with independent references from buoys or model reanalysis.

### 2.2.7 Overview of the Sensor Capabilities and Satellite Missions

Each sensor type has its own capabilities and limitations in terms of parameter measurement, coverage, resolution, sensitivity, and accuracy. In Tables 5, 6, and 7 an overview of these characteristics for each sensor type and for wind (Table 5), waves (Table 6), and surface current measurements (Table 7) is shown. Of course, these characteristics also depend on the platform parameters (orbit, altitude, pointing accuracy, etc.) and sensor generation, and are given below only for the typical configurations of the current satellite missions.

These tables also show that different types of sensors can complement each other to overcome intrinsic limitations of each of them individually. However, these opportunities are mostly obtained by using collocated observations from different satellite missions at cross-over points, as the missions that carry several instruments are scarce. This is illustrated in Fig. 14 which presents the timeline of the main satellite missions launched since 1985 with an objective on wind, waves or current measurement.

Figure 14 shows that the current era is highly favorable for wind and wave measurements, with at least 18 missions providing observations on wind and/or waves. This is expected to increase over the coming years with the continuation of the European Commission Copernicus series, and EUMETSAT MetOp programs in particular.

## 3 Ocean Weather and Climate

Historically, weather forecasts were traditionally made by meteorologists based only on an analysis of conventional observations, many of which were land-based. In recent decades, the development of satellite observations and the introduction of numerical weather prediction (NWP) methods using data assimilation and atmospheric circulation models, allowed weather prediction a few days ahead. Increasingly powerful computers continued to allow the development of more sophisticated models, providing the basis of a so-called quiet revolution in NWP, with the skill of forecasts improving by approximately one day per decade, such that faithful forecasts for more than a week ahead have become feasible (Bauer et al. 2015).

**Table 5** Main characteristics of the wind measurement capabilities depending on the sensor type

Parameters	Microwave radiometry			Radar altimetry		Wind scatterometry		SAR (Synthetic Aperture Radar)		GNSS Reflectometry	
	Wind speed, wind direction for certain configurations only	Wind speed only	Wind speed and wind direction	Wind speed only for the nadir track	Wind speed only	Wind speed and wind direction	Wind speed only	Most often only wind speed (not direction)	Wind speed only	Wind speed only	Wind speed only
Typical sampling at the surface	~ 50 km	~ 7 km (1 Hz), only along the nadir track	10–50 km	–	–	Several hundred of kms	20–500 km	A few hundred of meters	25–50 km	Multiple tracks across several hundred of kms	Low
Typical swath perpendicular to the satellite track	Few tens of km	–	–	–	–	Moderate, will increase with future sensors providing cross-polarized signals	Low	–	–	–	–
Sensitivity to extreme winds	High, even in rain conditions for low-frequency radiometers	Low	–	–	–	Of the order of 0.5–1 m/s, Ribal and Young 2020, Vogelzang and Stoffelen 2021	0.7 m/s, speed	–	–	–	–
10 m wind (U10s) accuracy	Less than 1 m/s in rain-free conditions (Bourassa et al., 2019)	1 m/s,	–	–	–	–	–	–	–	2.1–2.3 m/s (Bu et al. 2020)	–
Specifically designed for wind measurement?	No	No	Yes	No	No	Yes	No	No	No	No	No

**Table 6** Main characteristics of the wave measurement capabilities depending on the sensor type

	Radar altimeter	SAR (synthetic aperture radar)	Near-nadir scatterometry (SWIM-type)
Parameters	Significant wave height	Directional wave spectrum	Directional wave spectrum
Typical sampling at the surface	~ 7 km (1 Hz), only along the nadir track	~ 20 km every 100 km	90 km
Typical swath perpendicular to the satellite track	–	–	180 km
Sensitivity	Good sensitivity for wave heights from about 1 m	Detectability is limited to waves longer than 200 m in wave-lengths	Sensitive to waves for wavelength in [70–500 m] Limitations at low sea state ( $H_s < 1.8$ m)
Wave measurement accuracy	0.12 m to 0.16 std on SWH, depending on the mission (Dodet et al. 2022)		
Specifically designed for wave measurement?	No	Yes, for the SAR wave mode	Yes

**Table 7** Main characteristics of the current measurement capabilities depending on the sensor type

	SAR (synthetic aperture radar)	Interferometric SAR	Near-nadir Doppler scatterometry (SKIM design)	Medium incidence scatterometry (WaCM, SCA or STREAM designs)	Doppler SAR interferometry (SEASTAR concept)
Parameters	Total surface current velocity projected on the line of sight	Total surface current velocity, projected on the line of sight	Total surface current velocity, projected on the line of sight, and directional wave spectrum	Total surface current velocity and wind stress, projected on the line of sight	Total surface current vector and Ocean surface vector wind
Typical sampling at the surface	2 km	1 km	30 km for current vectors, 70 km for wave spectra	10 km	1 km
Typical swath perpendicular to the satellite track	200–500 km	200–500 km	300 km (proposed, with conical scan)	1000–2000 km (proposed, with conical scan)	150 km
Specifically designed for current measurement?	No	No	Yes	Yes	Yes

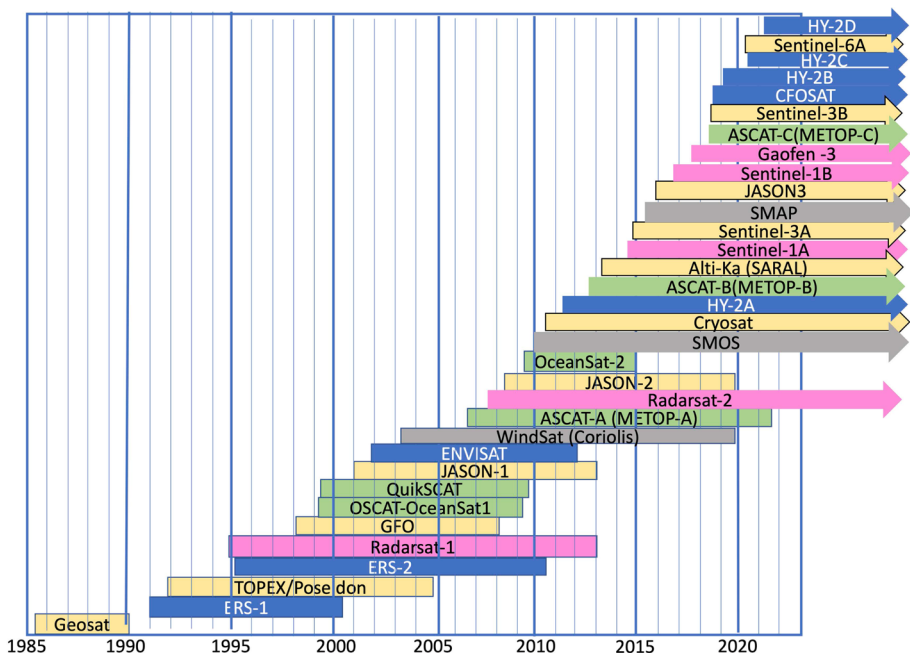


**Fig. 14** Timeline of the main satellite missions launched since 1985 delivering specific products on ocean surface wind, and/or waves. The name of the mission or of the instrument (and mission in parenthesis) is plotted in a chronologic way. The color of the segments and arrows refer to the radar altimeter missions (yellow), wind scatterometer missions (green), SAR missions (pink), microwave radiometer missions (gray) whereas the blue color is for multi-instrument missions which carry a combination of at least two of these instrument types. This figure starting in 1985 does not mention the pioneer satellite dedicated to oceanography Seasat, in operation for 3 months in 1978. It does not mention neither Nscat (on ADEOS) and Rapidscat (on ISS) because there were in operations for less than 2 years. Different countries and agencies are involved in the missions illustrated here: Canada (CSA), China (CNSA), Europe (ESA, EUMETSAT, European Commission), France (CNES), India (CSIRO), USA (NASA/JPL, NOAA). See also Appendix 1. More details on these missions can be found on <http://database.eohandbook.com/>

Numerical weather prediction (NWP) systems consist of complex numerical models that represent the dynamics of the atmosphere, the physical processes, and interactions that occur within it. Today, such systems also include other processes within the Earth system influencing the weather, such as ocean and land processes. This is an ever-evolving area of development, as ever more components are added to represent the interactions between these different processes, with the aim of providing an ever more comprehensive representation of the Earth system. In this context, the ocean surface is a particularly important component of the Earth System, where the sea state, in particular, is determined by the action of winds, with interaction of the waves with surface currents, and feedbacks from waves and surface currents on both the atmosphere and the ocean (Janssen and Bidlot 2018; Breivik et al. 2015). The use of satellite-based observations of wind and waves in predictive models is also essential for forecasting storm surges, which represent a major risk in the coastal areas.

Due to its extensive monitoring capabilities, Earth Observation from space plays an essential role in the initialization and improvement of these integrated Earth system models, which provide global fields of geophysical parameters required for climate change

monitoring, generating future climate projections and for guiding adaptation and mitigation. The current abundance of global ocean Earth observation datasets, and its future complement, are therefore very important for supporting the development of credible Earth system models, through both data assimilation and verification.

### 3.1 Use of Satellite observations of Surface Wind and Waves for Weather Prediction

#### 3.1.1 Data Assimilation for Numerical Weather Prediction

It is well-known that the skill of numerical weather prediction (NWP) systems generally degrades with the forecast range due to error growth with time. The predictability of the smallest scales is the least, while large scales are more predictable at the medium forecast range.

It is the role of data assimilation methods in NWP to help in minimizing these shortcomings, by combining the latest set of observations with a short-range numerical prediction to obtain an optimal estimate of the current state of the atmosphere and other components of the Earth system, termed an analysis. This analysis is used as the initial conditions for the next weather forecast. Accurate analyses are an essential component to good atmospheric forecasts. Analyses of surface waves can also improve wave forecasts.

Observations are unevenly distributed both spatially and temporally, as well as being subject to errors. As such, they do not provide a complete and accurate global representation of the state of the Earth system at a given point in time. However, a reasonable estimate of that state can be obtained from a short-range forecast based on the previous analysis and thus on previous observations. Data assimilation adjusts that forecast slightly, in a physically consistent manner, as it attempts to match the latest observations as closely as possible, taking into account uncertainties in the observations and the short-range forecast.

With the increase in powerful computers, more variables and finer spatial scales are described by the models, so that more spatially dense observations are needed for their initialization. Moreover, atmospheric dynamics dispersion relationships dictate that these finer scales evolve faster than the larger scales, hence also putting more demanding constraints on the timeliness and temporal sampling requirements of the global observing system (WMO<sup>9</sup>).

Different mathematical techniques can be used to combine Earth system observations with short-range forecasts. There are two broad classes of data assimilation methods. The first class consists of instantaneous assimilation (also called sequential assimilation) where corrections are undertaken at a local scale and at one time step, such as optimum interpolation (OI). Sequential methods are characterized by their simplicity and low computational cost, which makes them very attractive in operational forecasting. However, the corrections are not constrained to be consistent with the time evolution of the atmospheric dynamics. The second class takes into account the time evolution and comprises both so-called 4-D variational methods and the Kalman filter (KF) methods. For further information and discussion of these different data assimilation techniques, their benefits and limitations, the interested reader is referred to Lorenc et al. (2015). An intricate part of data assimilation obviously relies on how the observations are used to inform (i.e., change) the NWP model state. The NWP background error covariances play a crucial role in the spatial

<sup>9</sup> <https://space.oscar.wmo.int/variables/>.

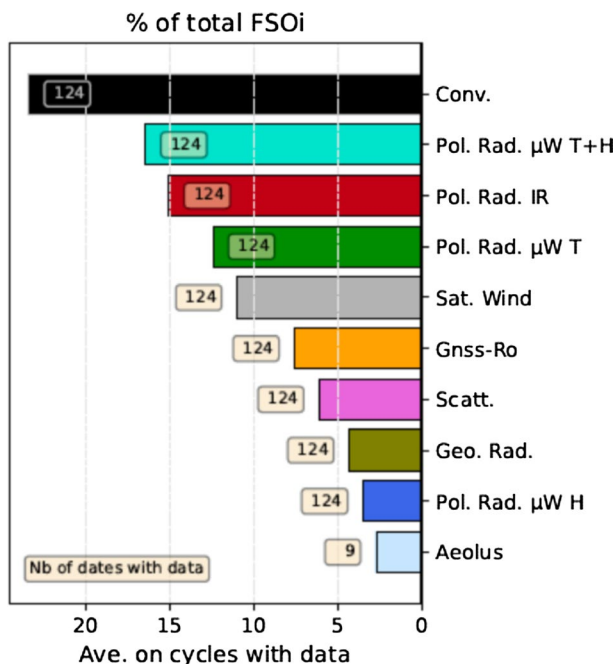


**Fig. 15** Relative contribution of data assimilation to error reduction of a 24-h meteorological forecast with the numerical model ARPEGE, operational configuration (Météo-France). The contribution of scatterometer observations is shown in pink color (winds from ASCAT of MetOp-A and MetOp-C, HSCAT on HY-2B and HY-2C, broadcasted by the EUMETSAT OSI SAF, used in this configuration). The metrics of error reduction by data assimilation is the Forecast Sensitivity Observation Impact (FSOI), moist energy norm/moist adjoint used—see Chambon et al. (2022), and Cardinali (2009) for details on this metrics. The figure is plotted for the month of October 2022. Figure from <http://www.meteo.fr/special/minisites/monitoring/FSOI/index.html>, with copyright authorization by Météo-France

and temporal filtering properties, i.e., to set the deterministic spatio-temporal scales of the NWP model error (e.g., Mile et al. 2021). In addition, the estimated error variances and observation density are critical in determining the balance of weights between modeled and observed information, where too low a weight afforded to the observations minimizes its impact on the analysis and forecast, whereas too high a weight afforded to the observations may result in spurious analysis noise due to overfitting, degrading the subsequent model prediction (Stoffelen et al. 2020b).

**3.1.1.1 Assimilation of Wind Observations** In the tropics, and elsewhere on scales less than approximately 500 km, 3D turbulence dictates the atmospheric dynamics, which implies that wind observations are most effective for the initialization of these scales in terms of forecast skill (Stoffelen et al. 2005). Moreover, ocean vector winds are essential inputs to ocean wave, storm surge and ocean circulation forecasts.

Data assimilation formalisms provide a so-called “Best Linear Unbiased Estimate,” implying that no local biases should exist between observations and model in NWP data assimilation. However, Belmonte and Stoffelen (2019) and Fig. 2 suggest NWP model wind biases may reach large values, depending on physical parameterization errors associated with the atmospheric boundary layer, moist convection and dynamical model closure



and fluxes, among others. When large systematic errors exist, further optimization is recommended prior to using wind scatterometer data in global and regional models (Stoffelen and Vogelzang 2021; Stoffelen et al. 2020b). Nevertheless, despite these shortcomings, scatterometer winds do contribute substantially and beneficially to ocean and atmosphere numerical weather prediction and analysis (e.g., Laloyaux et al. 2016; Stoffelen et al. 2013b; Isaksen and Stoffelen 2000; Stoffelen et al. 2015; Chambon et al. 2022). This is illustrated by Fig. 15 which shows the contribution of satellite data assimilation (and in particular assimilation of scatterometer observations) to error reduction in the atmospheric forecast. Figure 15 is based on the “Forecast sensitivity observation impacts” (FSOI) analysis method applied here on the estimated global moist energy of the atmosphere with a moist adjoint technique (see Cardineli 2009; Chambon et al. 2022 for details on this method) and estimated here from 24-h forecast fields of the French global atmospheric circulation model ARPEGE for the month October 2022. It shows that scatterometer observations contribute to about 6% of the error reduction due to assimilation of satellite observations. Chambon et al. (2022) also mention that although the impact of scatterometer winds is limited to low levels, it is kept at longer forecast ranges compared to other observations. Furthermore, they provide unique observations of the ocean surface wind vector in certain areas (particularly in the tropics and Southern hemisphere).

**3.1.1.2 Assimilation of Altimeter Wave Height Observations** The launch of the ERS-1 satellite in 1991, with the capability of near real-time dissemination of radar altimeter significant wave height (SWH) observations, highlighted the potential for the operational assimilation of such data. One of the earliest efforts to utilize this capability was the work done by Lionello et al. (1992) who implemented the instantaneous sequential data assimilation technique known as optimum interpolation (OI) to assimilate altimeter SWH into the third-generation ocean Wave Model WAM (Wamdi group 1988). The OI sequential data assimilation method is an attractive scheme for operational forecasting due to its low computational cost. While this method was discarded in operational weather forecasting in favor of variational analysis like 3D-Var and 4D-Var, OI is still in use for operational wave data assimilation for several reasons. Firstly, variational analysis requires the knowledge of the model adjoint and the tangent linear version which are not available for the wave model in its final state (this was explored for earlier versions of the WAM model like those of De las Heras et al. (1994) and Hersbach (1998) but are not usable for the current model version). Secondly, the volume of wave data to be assimilated is not substantial and so it remains compatible with an OI scheme. Voorrips and de Valk (1997) compared the results of the variational approach with an OI method and did not observe any particularly advantage for the more complex variational method (presumably because of not having optimally calibrated the tangent-linear model). Even if there was an improvement with variational method, this improvement would be absorbed by the necessary ad hoc assumptions made to distribute SWH analysis increments over the whole wave spectrum (see below).

Although the wave forecast skill depends on the numerical wave model itself, it is also fundamentally determined by the quality of the driving wind field. Therefore, the use of the wind as the control variable in the wave data assimilation scheme may present itself as a strong candidate. This implies the adjustment of the wind field such that an optimal agreement with the observations for SWH is obtained. This is achievable for the waves generated by the local wind (wind waves) where updates to the wind field can be obtained in the context of a single time step approach. However, in the case of swell, this approach does not work because the swell was generated by remote storms hundreds or thousands

of kilometers away and some time (e.g., few days ago). The assimilation of altimeter SWH observations data represents an additional challenge because it only provides information on the integral over the frequency and direction of the wave spectrum, whereas modern wave models are based on a spectral description. Applying the assimilation method results in a wave height correction (analysis increments) which must be translated to a corresponding change in the local wave spectrum. For wind-waves, this is easily done by using the evolution laws for wind-generated waves, as obtained from idealized model runs. However, for swell, it is assumed that the mean wave steepness is invariant during the transformation, which may be plausible, but in practice this assumption is hard to justify (Lionello et al. 1992; Greenslade 2001).

Presently, most global weather centers with wave modeling capabilities are using OI or related schemes to assimilate significant wave height from several altimeters like Jason-3, Sentinel-3 family and Sentinel-6. The SWH data provided by the radar altimeter (RA) missions are subject to quality control a quality control procedure to eliminate any erroneous, inconsistent or suspicious observations. Footprint contamination by land, ice and slicks results in erroneous altimeter measurements. The accepted RA data are then averaged along the track to form super-observations (in a process referred to as “superobbing”) with scales compatible with the model scales. This is important in order to prevent the introduction of small-scale variability, which cannot be handled by the model that has rather smooth fields. RA and model background (also called the first guess) SWH are merged in the OI scheme to produce the SWH analysis increments. The corrections are then distributed over the whole wave spectrum based on the assumptions related to wind-sea (wind-waves) and swell conditions.

Besides the operational assimilation of SWH in wave models based on the OI method, several research studies have been undertaken to develop and test alternative methods. For example, a multi-time Kalman Filter (KF) method was developed by Voorrips et al. (1999), which allows for the provision of error statistics on the model variables. The KF propagates a forecast error covariance matrix which gives further information on the model state. However, such techniques require additional computational requirements, which then has implications for the required number of model integrations. For wave data assimilation systems, some simplifications are required to reduce the cost of such methods (Voorrips 1998).

The beneficial impact of the satellite altimeter SWH assimilation on the significant wave height forecasts have also been shown to be substantial, particularly at short lead times, and in the coastal regions (Saulter et al. 2020). The relatively short ‘system memory’ of the wave data assimilation system suggests that wave data assimilation is best performed in a rapidly cycling short-range forecast system, on the basis of timely satellite observations.

**3.1.1.3 Assimilation of Spectral Information on Ocean Waves** The wave mode of the synthetic aperture radar (SAR) provides a wealth of information regarding the detailed description of the surface sea state with global coverage. Unfortunately, SAR is not able to sense the whole spectrum of ocean waves, especially in the azimuthal direction and misses quite a large range of short waves. However, the resolvable part of the spectrum (typically for wavelengths longer than 200 m) can be very useful in a wide range of oceanic applications including data assimilation in ocean wave models.

For the first time, the ERS-1 and -2 missions (launched in 1991 and 1995, respectively) provided SAR spectra (Level 1b product) on a Near Real-Time and global ocean coverage basis, thanks to their wave mode (WM) which provided spectra every 100 km along the

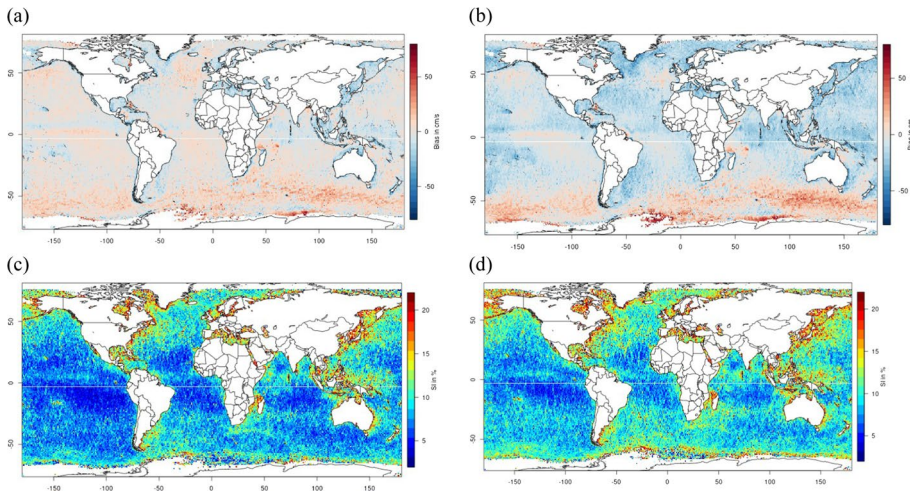


**Fig. 16** Mean Bias **a, b** and scatter index **c, d** between the MFWAM model SWH and altimeter SWH from Jason-3, Saral and Sentinel-3A altimeters for the period July to December 2019. **a** and **c** with assimilation of SWIM observations (i.e., nadir SWH and spectral parameters) **b** and **d**: without assimilation. From Aouf et al. 2022

track. The inversion of the SAR spectrum to the ocean wave spectrum before assimilation was a challenge. The iterative MPI-M (Max Planck Institute for Meteorology) nonlinear mapping scheme (Hasselmann and Hasselmann 1991; and Hasselmann et al. 1996) was initially used to obtain the ocean wave spectra. With this method, in spite of the required use of a first-guess from the wave model to initialize the inversion, the assimilation of SAR WM Level 1b SAR spectra proved to be beneficial for wave forecasting (e.g., Abdalla et al. 2004, 2006).

ESA started to produce WM Level 2 ocean wave spectra from SARs onboard the ENVISAT and Sentinel-1 family based on the method proposed by Chapron et al. (2001). This method does not require a first-guess estimate for the inversion, thanks to the quasi-linear approximation used. This is quite a noticeable evolution as the inversion of such observations before their assimilation is completely independent of the model results. However, it was shown that careful quality control filtering is needed to eliminate erroneous and suspicious data (Johnsen 2005; Aouf et al. 2006).

The implemented assimilation procedure itself is based on the assimilation of the main parameters (energy, mean period and mean direction) of wave systems identified from a partitioning scheme applied to the directional wave spectra (Hasselmann et al. 1997; Voorrips et al. 1997; Aouf et al. 2006). For this, the full spectrum is first divided into several wave systems using a so-called “watershed” method (e.g., Hasselmann et al. 1997; Hanson and Phillips 2001). The scheme separates both the model and SAR directional wave spectra into a set of distinct wave systems. The different wave systems are characterized by their total energy, mean frequency and mean propagation direction. These integrated parameters of the partitioned systems are assimilated using a simple Optimum interpolation (OI) scheme following a cross-assignment procedure to correlate the observed systems with the modeled first-guess (FG) ones. The analysis (AN) integrated parameters obtained from the OI scheme are used to construct the AN spectra by resizing and reshaping the FG spectra. Both Meteo-France and ECMWF have

developed the assimilation schemes for the operational forecast system, assimilating first SAR ENVISAT wave spectra, and have shown their positive impact in the prediction (Aouf and Lefèvre 2012). Today, Meteo-France operationally assimilates spectral wave data from Sentinel-1 (SAR) and CFOSAT/SWIM (Real Aperture Radar). As discussed in Sect. 2.2.5.2, thanks to its real-aperture concept, SWIM can resolve dominant wavelengths up to about 70 m, i.e., shorter than the 200-m cutoff limit of the SAR. This is an interesting complement to SAR not only in terms of spatio-temporal sampling but also for observations of short swell and wind wave situations (for significant wave heights larger than about 1.8 m, see Sect. 2.2.5.2 and Hauser et al. 2021). In addition, the nadir looking beam ( $0^\circ$  incidence angle) is used for producing SWH from the altimetry signal. It was demonstrated by Aouf et al. (2019) and Aouf et al. (2021) that assimilation of SWIM directional wave spectra has a positive impact on ocean wave analysis and forecasts. With the current operational assimilation, the bias between the SWH from the Meteo-France WAM (MFWAM) model and independent altimeter observations was shown to be reduced compared to a no assimilation case, particularly in the Southern Ocean area (see Fig. 16a, b). The same conclusion was reached for the scatter index (Fig. 16c, d), with a mean reduction of the scatter index of 15% in high and mid-latitudes and of 22% in the tropics. Furthermore, it was shown that assimilation of spectral information decreases the bias on the dominant period compared to buoy observations (National Data Buoy Center -NDBC) by 0.01 s, and significantly decreases the scatter index on the dominant period (compared to NDBC buoys): for example, for cases with dominant periods larger than 10 s, the scatter index on the dominant period is 12.4% with assimilation of SWIM spectral information instead of 13.8% with assimilation of SWIM SWH and 14.5% without assimilation. In a study focused on the Southern Ocean, Aouf et al. (2021) showed that in this region, where conditions of non-fully developed wind seas are frequent, assimilation of wavelengths and directions in addition to the SWH not only corrects the significant wave height from biases compared to SWH from altimeter match-ups but also significantly corrects the wave age, and the dominant wavelength predicted by the model. This study also showed that assimilation of directional information helps the model to control the transition between wind waves and mature sea regimes. It was also revealed that assimilation of spectral information affects the predicted atmospheric drag coefficient, dissipation of wave energy, and turbulence intensity in the upper layer of the ocean. Therefore, assimilation of spectral parameters is expected to substantially improve the descriptions of ocean/atmosphere coupling in terms of both momentum and gas flux transfer which remain still poorly represented in climate models.

**3.1.1.4 Assimilation in Coupled Earth System Models** Many operational systems use separate data assimilation systems for the atmosphere, ocean, waves, and land surface and sea ice. This will produce an inconsistent analysis as the data assimilation systems are independent from each other. Coupled data assimilation aims to ensure the analysis of different Earth system components is consistent. This can be achieved by allowing the observations to influence the analysis in several Earth system components by changing the initial conditions of each Earth system component in a way that is physically consistent with the other components. The Earth system interactions between the atmosphere, ocean and waves mean that continued advances in data assimilation and modeling of winds, waves and currents will continue to deliver improvements in numerical weather prediction as well as in wave and ocean predictions (see e.g., Laloyaux et al. 2016).

### 3.1.2 Use of Satellite Observations to Validate or Improve Earth System Models

In addition to assimilation, space-borne observations are very useful for the validation of Earth system models and in tuning their parameterizations.

As an example, thanks to the estimation of swell energy decay along its propagation path obtained from SAR images (Ardhuin et al. 2009b, 2010), the source and dissipation terms of the wave energy balance equation have been recently updated in several main wave prediction models (WW3, WAM). Wave observations from altimetry have also recently been used to assess the spatial resolution required for an oceanic circulation model coupled to a wave model for the purpose of reproducing the spatial gradients of significant wave height across the current due to wave-current interactions (e.g., the study on the Agulhas current by Marechal and Ardhuin 2021).

On the atmospheric side, it is known that global NWP model wind vector components show a lack of natural wind variability (see comments in Table 2), particularly in the meridional wind component variability (Belmonte and Stoffelen 2019). Conversely, specific wind scatterometers (and in particular ASCAT) has the ability to measure the extreme divergence and convergence associated with the updrafts and downdrafts in tropical moist convection (Priftis et al. 2021), while a global NWP model does not show these (King et al. 2022). Moist convection processes typically have a 30-min time scale and cannot be traced by initialization in NWP over the ocean. Moreover, rain cells are small in size. The collective effect of moist convection is therefore parameterized in NWP models to capture the vertical exchanges of mass, momentum and energy. Another source of small-scale exchanges over the ocean is furthermore associated with local sea surface temperature gradients and can be detected by averaging wind differences over a few days, since the mesoscale ocean conditions are stable, after blurring over a scatterometer footprint. Such multi-day averaging will remove scatterometer and atmospheric model wind differences due to the transient weather, but will highlight differences related to stationary ocean conditions. Such geographical biases may also appear due to other systematic errors, for example, in the boundary layer parameterization and dynamical model closure (e.g., atmospheric model diffusion operators); see Trindade et al. (2020). The atmospheric model 10-m stress-equivalent wind errors do not only appear at small scales, but also on larger scales as shown in Fig. 2 (Belmonte and Stoffelen 2019). These errors are detrimental in Earth system modeling, as they cause biases in ocean forcing, wave and storm surge prediction, and because they are associated with important modes of variability in the tropics and elsewhere, affecting air-sea exchanges and hence earth system dynamics. For all these situations, satellite observations are very useful to better diagnose the limits of the models and further improve their representation.

### 3.1.3 Storm Surge Forecasting

Besides winds and waves, storm surges are among the deadliest and most costly natural disasters, particularly impacting low-lying areas. Timely wind and surge information and short update cycles can also be critical for the accurate prediction of storm surge levels, such as for the large storm surge in Venice on November 2019. This surge was severely under-predicted, in part due to not considering the most recent ASCAT winds (Giesen et al. 2021). Therefore, numerical prediction of wind, waves and storm surge



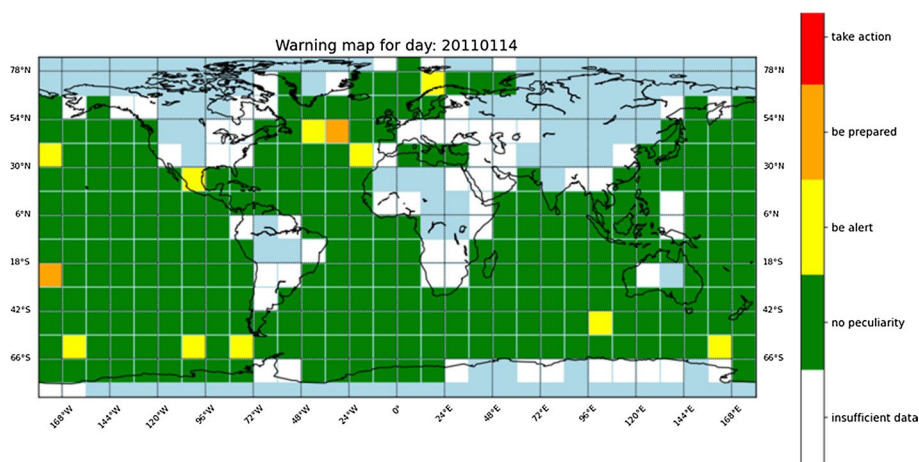


**Fig. 17** Example early-warning map for large differences between scatterometer observations and wind vector short-range ECMWF wind forecasts, based on more than a decade of local monthly exceedance probabilities. The largest differences are in yellow and orange. Based on this type of map, alerts can be activated for nowcasting applications and on-the-fly as new scatterometer observations come in

are usually integrated, such that the improved winds obtained through data assimilation of satellite observations are optimally exploited (e.g., Caires et al. 2018).

Coastal storm surge due to tropical cyclones can be particularly devastating in embayments that are poorly protected against high water levels. Dullaart et al. (2020) use Earth observation data to assess modeled tropical cyclones and subsequent storm surge forecasts. For Hurricane Irma, the modeled coastal storm surge height increased from 0.88 m with the ECMWF ERA-Interim reanalysis wind and wave fields (Berrisford et al. 2011) to 2.68 m with the more recent ECMWF ERA5 reanalysis (Hersbach et al. 2018), compared to an observed surge height of 2.64 m, with the same authors finding that further increases in model resolution results in a better representation of the wind fields and associated storm surges, especially for small sized tropical cyclones. These recent and future advances in storm modeling contribute to the accuracy of early-warning systems and coastal flood hazard assessments at the global-scale. For climate research, extreme event trends will also become more credible.

Storm surge models have been further improved on continental shelves by analyzing a several decades of altimeter sea heights (Zijl et al. 2013), which have been exploited to improve the surge model bottom friction and bathymetry.

### 3.1.4 Nowcasting

Due to the continuous improvements in NWP, the role of the weather forecaster continues to evolve. Today, in nowcasting applications, observations acquired in near-real time are used to monitor the forecast performance of NWP products. It is estimated that over a hundred different satellite instruments contribute to the NWP forecast and therefore forecasters cannot monitor all of the corresponding sensor data for detecting forecast errors. Instead, local forecast errors are detected in real time by automated quality control tools, as satellite observations are received in a timely manner. For example, Fig. 17 shows a global warning chart of local areas where the short-range ECMWF forecast is anomalously different from

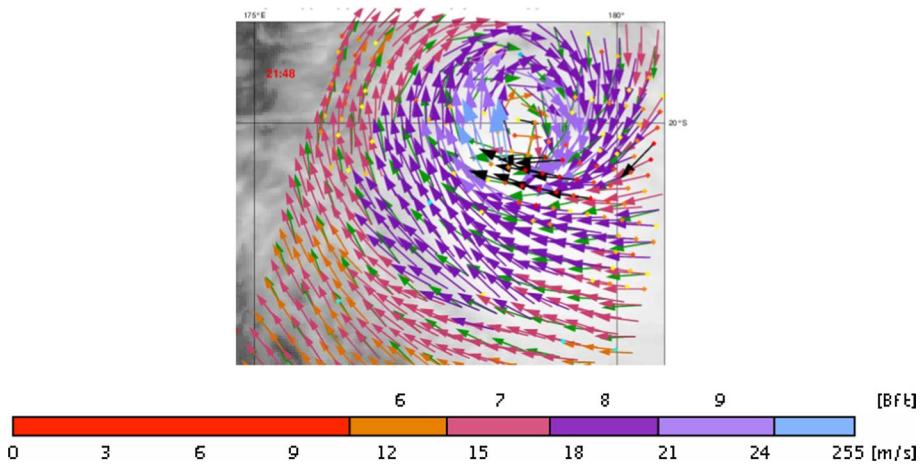


**Fig. 18** Wind field from the ASCAT-B scatterometer (arrows with color scale) and from the ECMWF numerical weather prediction model (green arrows) overlaid on the infrared satellite image (from meteorological satellite Himawari). The scatterometer and model winds are from 28 December 2019 21:48, while the Infrared image is from 21:30 UTC. The scatterometer winds are colored according to the Beaufort scale as shown with the color bar. The black arrows are plotted where the KNMI QC flag is raised (MLE > 18). The colored dots give the value of the Maximum Likelihood Estimator (MLE), which indicates how well an observation fits the GMF. High MLE values indicate high spatial wind variability in the wind vector cell, WVC

the latest ASCAT scatterometer wind vector observations. Each tile in this map can be used as the basis for providing an automated alert using the current instrument data and the NWP forecast products.

### 3.1.5 Improving Characterization and Forecast of Extreme Events

Tropical cyclones (TCs), extra-tropical storms and polar lows have major impacts on damage and human safety in coastal areas from extreme precipitation, extreme winds and storm surge. TCs are of great concern because of both their frequency and impact. For example, half of the 15 weather disasters of 2019 with over \$1 billion of damage were related to TCs.

TCs are often defined in terms of wind intensity and size, where size is usually specified as the maximum radial extent of wind speed thresholds such as the maximum, 64-, 50-, and 34-knot winds (kt; 1 knot = 0.514 m/s), and radius of maximum wind speed. The Dvorak Technique (Dvorak 1984), a subjective analysis of infrared cloud patterns, forms the basis of these wind intensity estimates and has been augmented in the Atlantic and sparingly elsewhere with aircraft-based observations such as dropsondes and winds derived from the airborne Stepped Frequency Microwave Radiometer (SFMR, Uhlhorn and Black 2003; Uhlhorn et al. 2007; Klotz and Uhlhorn 2014; Sapp et al. 2019).

In addition, ocean surface wind field estimates from scatterometer algorithms (Polverari et al. 2021; Stoffelen 1998; Figa-Saldaña et al. 2002; Misra et al. 2019) have been providing valuable wind observations in and around TCs since the early 2000s (Isaksen and Stoffelen 2000; Brennan et al. 2009)- see Fig. 18. Performance of existing scatterometers is curtailed by extreme winds (i.e., saturation above 70 kt) and Ku-band scatterometers also



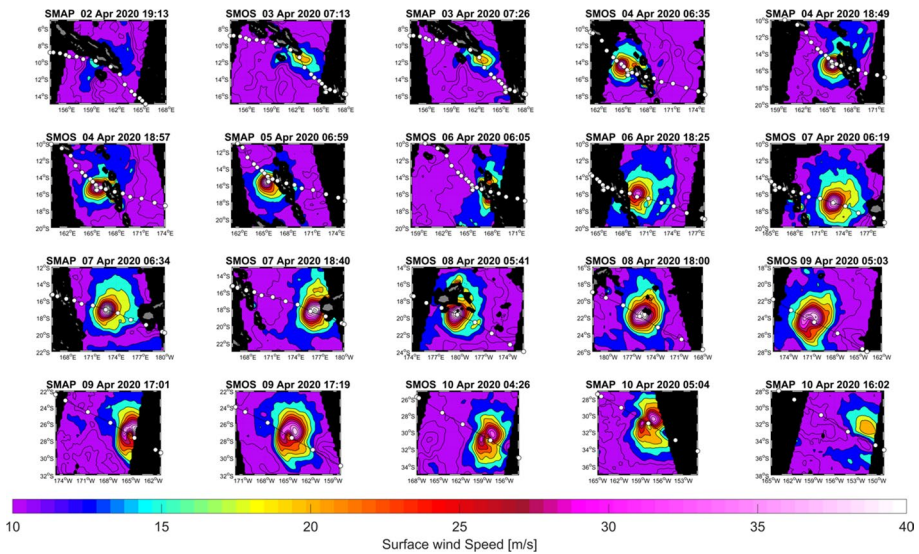


**Fig. 19** Successive (time is evolving from left to right and from top to bottom) maps of surface wind speed measurements provided by SMOS and SMAP L-band sensors during lifetime of Category 5 severe Tropical Cyclone Harold in the South Pacific in April 2020

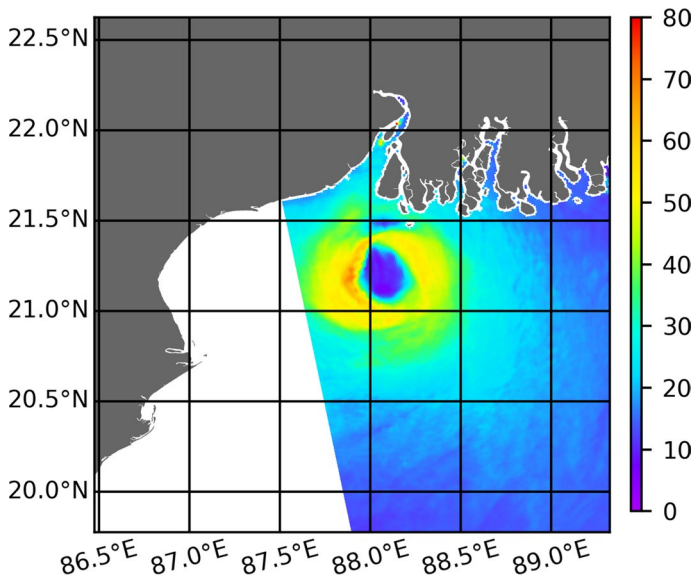


**Fig. 20** Wind speed map obtained from a SAR image during the tropical cyclone Matmo (23rd TC of the JTWC western North Pacific 2019 season) on 09 Sep 2018 12:12 UTC immediately prior to landfall near Calcutta, India. Wind speed intensity in  $\text{m s}^{-1}$  is given by the color bar

suffer from the presence of rain clouds that prevent reliable estimates of extreme winds. Furthermore, since all these microwave sensors are on low-orbit platforms (i.e., polar

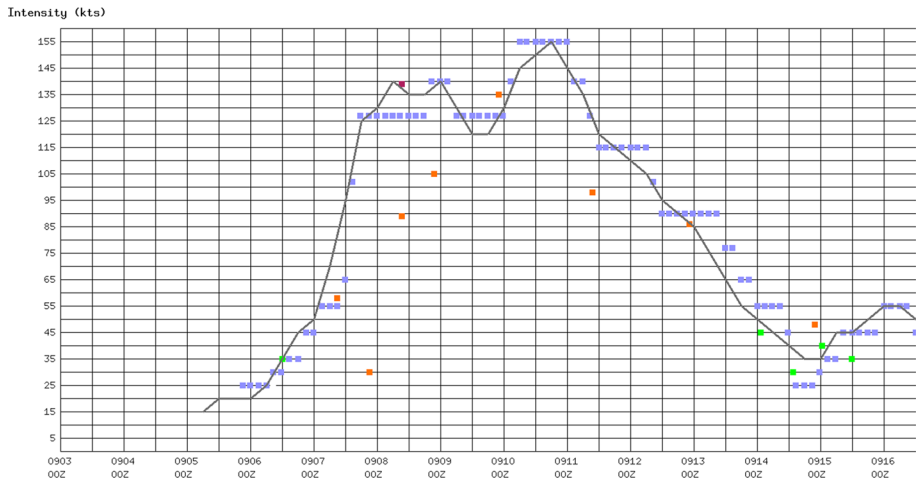


**Fig. 21** Intensity (kt) versus Time (month and day) estimated from the Dvorak method (light blue squares), ASCAT (green squares), SMAP (orange squares), Sentinel1 SAR (purple square), along with Joint Typhoon Warning Center intensity (black line) for Chanthu (19th TC of the 2021 western North Pacific season)

orbiters with limited swath), the frequency of passes over a given TC from a single satellite is low. To begin to address operational needs, the individual scatterometers and radiometers operating at any time must be used together in a so-called virtual constellation, requiring a dedicated effort for intercalibration between wind products from these sensors (CEOS<sup>10</sup>). At extreme wind speeds, brightness temperatures from microwave radiometers and, in particular, those in L-band, are of particular interest because of their good sensitivity even at very high winds. Therefore, algorithms have recently been developed using L-Band and multi-band radiometers (see Sect. 2.2.1).

In recent years, the joint typhoon warning center (JTWC) has been using SMAP and SMOS data to aid with their analysis of surface winds and intensity and this information is being saved on the automated tropical cyclone forecasting system (Sampson and Schrader 2000) for best track preparation. Figure 19 shows an example of the wind field evolution during 8 days of the lifetime of the severe tropical cyclone Harold (South Pacific in 2020), obtained thanks to a rather dense and coherent coverage with combined measurements from SMOS and SMAP.

Detection of high surface wind intensity associated with small intense tropical cyclones traditionally present challenges for radiometers and scatterometers due to resolution constraints (e.g., L-band derived winds have approximately 40 km footprints). New SAR observations have demonstrated their capability to measure high winds near the centers of even these very small intense TCs (Mouche et al. 2017). Thanks to their higher resolution (about 50 m) combined with a dual-polarized mode (co- and cross-polarized channels), SAR observations can provide wind speed estimates of up to 160 kt, and allow the detection of the local maximum winds in the eyewall belt (Fig. 20 and Combet et al. 2020), including when adjacent to coastal areas. However, SAR measurements also suffer from shortcomings in conditions of extreme rain ( $> 80 \text{ mm h}^{-1}$ ) that impact on the wind speed

<sup>10</sup> <https://ceos.org/ourwork/virtual-constellations/osvw/>.

estimates (Mouche et al. 2019), similarly to C-band scatterometers. Most importantly, the number of SAR observations is limited. The SAR swath width is approximately 500 km and scene acquisitions must be ordered 48 h in advance, which requires accurate TC forecasts to acquire a scene that includes a TC center. Since SAR wind speeds are new to operations, challenges also exist relating the high-resolution instantaneous wind speeds to the one- and 10-min temporal average TC intensities used by the TC warning centers.

Recent improvements in the space-borne retrieval algorithms discussed above are expected to be incorporated after detailed assessment, into operations by TC warning centers such as the Regional Specialized Meteorological Centers and the Joint Typhoon Warning Center (JTWC) in Honolulu. An example of SAR products used in such operations is discussed in Jackson et al. (2021).

Cross-calibration of winds from individual sensors and algorithms also remains a challenge. The usual approach is to use as reference in-situ wind speeds measured by dropsondes deployed from aircraft flights above the tropical cyclones. This in-situ reference data has traditionally been applied to the airborne stepped frequency microwave radiometer (SFMR, Uhlhorn and Black 2003; Uhlhorn et al. 2007; Klotz and Uhlhorn 2014; Sapp et al. 2019), to Dvorak wind estimates (Dvorak 1984) and to most passive satellite ocean winds. However, recent results indicate that these dropsonde wind measurements and in-situ moored buoy observations are inconsistent in the overlapping range of 15–25 m s<sup>-1</sup> (Polverari et al. 2022). Stoffelen et al. (2020a) further documents the inconsistencies between extreme winds from passive radiometers and scatterometers and present a way forward for the cross-calibration of space-borne sensors at different spatial resolutions.

Figure 21 illustrates both the potential and challenge of using wind speed estimates from individual sensors and algorithms to estimate the intensity of the super-typhoon Chanthu, which occurred in 2021 in the western North Pacific. Subjective intensity estimates from the Dvorak technique (Dvorak 1984) are displayed along with intensity estimates based on remotely sensed data. It is immediately apparent there can be large differences between the subjective Dvorak analysis and the analysis from remotely sensed measurements. These large differences can be seen in intensity estimates from the 40-km resolution L-Band sensor SMAP, probably due to the limited coverage and resolution not fully adapted for this small and intense TC. Also seen are the intensity estimates using ASCAT winds for intensities under 70 kt (i.e., not during the maximum intensity). The single Sentinel-1 SAR pass for this case was directly over the TC center and captured the small radius (< 40 km) of maximum wind and the high winds. Operational forecasters are learning how to use these intensity estimates for their subjective real-time estimates (Knaff et al. 2021). To help with this task, cross-calibration of space-borne products should be improved with a particular interest on the radial extent of maximum wind at different thresholds (e.g., 64-, 50-, and 34-knot winds), taking into account that other parameters like wind intensity present more challenges due to sampling or resolution.

New and future capabilities will help to develop more satellite-based tools for operational needs, and for collecting climatological datasets of extreme winds. Therefore, continued efforts are needed to strive for more frequent, timely, and accurate surface wind estimates in extreme wind environments. The current generation of wind scatterometers, SAR and L-band radiometers have already proved their utility, but new generation scatterometers will improve on the current suite. For example, the scatterometer of second generation planned by EUMETSAT (Stoffelen et al. 2017a) to be carried by MetOp-NG will use, in addition to a co-polarization channel, the cross-polarization (HV) channel whose signal does not saturate at high wind speeds.

### 3.2 Wind, Waves and Surface Current Observations as Key Factors of the Earth System

The three essential climate variables of wind, waves and surface currents play different roles in the Earth system, and are able to be characterized with very different degrees of accuracy. From a general (large-scale) climate perspective, surface winds are probably the most important variable as they are a leading contribution to air-sea fluxes of heat and gases, with a direct impact on the Earth energy balance (Hansen et al. 2011).

This importance of wind, waves and currents is able to be described via that the air-sea turbulent flux for any quantity  $X$ , as approximated with a bulk expression of the form:

$$\text{Flux} = \rho C_X (X_a - X_o) |\mathbf{U}_{10N} - \mathbf{U}| \quad (14)$$

where  $\rho$  is the air density  $C_X$  is the “exchange coefficient” for any variable  $X$ ,  $X_a$  and  $X_o$  are the values of the variable  $X$  on either side of the interface, atmosphere or ocean,  $\mathbf{U}_{10N}$  is the neutral wind at 10 m height, a horizontal vector, and  $\mathbf{U}$  is the surface current vector. This type of flux law is generally applicable to gases, momentum, sensible heat, and latent heat (which is the evaporation flux times the specific latent heat for water vaporization). In particular, the drag coefficient relates the wind speed to the momentum flux, also known as “wind stress.” It is known that this drag coefficient increases with wind speed, at least for winds between about 5 and 25 m/s, but that it is also modified by wave conditions (wave age, and/or significant slope); see Drennan et al. (2003), Brumer et al. (2017), Zhao and Li (2019) for reviews.

Overall, Eq. (14) indicates that ocean surface wind (or wind stress) is critical to exchanges of heat, mass, and momentum and thus largely influence ocean mixing and transport and by consequence, water mass formation (water with temperature, salinity and density characteristics) and ocean circulation (Waugh et al. 2013).

Besides their contributions to the  $C_X$  exchange coefficients, waves are also important in the way that they (among other effects):

- determine near-surface ocean mixing via breaking and Langmuir circulation (Noh et al. 2004; d’Asaro et al. 2014), which can bring a strong modification of air-sea fluxes by changing the near-surface ocean properties,
- define the energy levels at the shoreline. Wave energy is a key element in extreme sea levels and impacts on man-made infrastructure. The coastal wave climate is also a key element in the nearshore habitability by marine species (Denny et al. 2004), and human usage of coastal areas (Kamphuis et al. 2020), the dominant shaping agent of coastal morphodynamics (Anthony 2015; Cox et al. 2020),
- interact with sea ice and icebergs, with complex interactions with different types of ice that include the breakup of ice floes, the erosion of icebergs, and attenuation of waves by floating ice (Liu and Mollo-Christensen 1988; Ardhuin et al. 2020).

Likewise, ocean currents have an explicit contribution to air-sea fluxes, since, as is seen in Eq. (14), these depend on the displacement of the air relative to the surface motion. This contribution, although limited because the wind speed is generally an order of magnitude larger than the surface current, can be very important where currents are strong and the wind is weak, such as along the Equator. Even where it is weak, this effect constitutes a “current feedback” that is a dominant term in the work of the wind and the dynamics of eddies (Dewar et al. 1987). Taking currents into account for estimating the air-sea flux is

critical for predicting the ocean eddy kinetic energy and the path of western boundary currents (Renault et al. 2016a, 2016b).

Surface currents also influence the Earth system and its climate in two important ways: firstly by transporting ocean properties—and the large-scale current properties are dominant in that regard—and secondly by inducing the mixing of different water masses at the surface and subsurface. Geostrophic currents are routinely estimated from measurements of sea level anomalies using satellite altimeters (paper within the same special collection), and a mean dynamic topography derived from a combination of satellite gravimetry and in situ drifters (Mulet et al. 2021). Estimates of surface transport have used these geostrophic currents and estimates of wind-driven currents for a wide range of applications. However, in some regions, such as the Equatorial Atlantic, the seasonal evolution of the mixed layer heat content cannot be explained without vertical mixing (e.g., Foltz et al. 2019).

For mixing, all spatial and temporal scales are important, many of which are not yet observed from space, in particular the near-inertial currents with periods of 12 h to a few days (function of the latitude), and that dominate the surface current field in regions like the north-east Pacific. These motions have typical spatial coherence scales of a few hundred kilometers, making it possible to be mapped from space with a single Doppler scatterometer with a swath width of 300 km or more (Ubelmann et al. 2021). Doppler scatterometers have the potential to access the full surface current vector at scales larger than 10 km (Rodriguez 2018; Arduin et al. 2019b), which can be extended down to 1 km with along-track interferometry synthetic aperture radar (ATI-SAR), as proposed by Gommenginger et al. (2019). Tracking wave dispersion from space in sequences of optical imagery can also produce currents at a resolution of 1 km (e.g., Kudryavtsev et al. 2017a), and in principle it should be able to produce estimates of vertical current shear that are important for vertical mixing (Arduin et al. 2021).

The processes related to small spatial scale air-sea interaction and mixing are strongly tied to gradients in the wind vector, which impact vertical motion in the ocean and atmosphere (Shi and Bourassa 2019) and therefore change the properties of the ocean and atmospheric mixed layer, and in turn the large-scale air-sea interaction (O'Neill 2012; Shi and Bourassa 2019) and weather (Parfitt et al. 2016).

In summary, all the above-mentioned processes couple two major dynamical components of the Earth system, namely, the atmosphere and the ocean that are themselves strongly linked to cryosphere and terrestrial processes.

In this context, one of the challenges for satellite observations is to provide turbulent fluxes instead of state variables like wind, waves and currents. Although some advances have been made in this sense, for example by providing stress-equivalent wind speed from scatterometer observations, this objective remains challenging. One of the main issues is the lack of in situ direct measurements of turbulent fluxes that are necessary to build and/or assess the appropriate inversion methods.

Nevertheless, satellite observations are very useful when studying the interaction between the atmosphere and the ocean. For example, based on the combination of a three-way coupled ocean-wave-atmosphere modeling system for the Gulf Stream region, and wind scatterometer measurements, Shi and Bourassa (2019) concluded that comparisons between modeled equivalent neutral winds and satellite winds estimated from scatterometer can be used to assess wind stress parameterizations and wind stress-related feedback in coupled models.

Such data can also be used to study the interaction between waves and currents, which are of interest not only because of their induced risk of rough conditions for operations at sea, but

also because they greatly modify the ocean's vertical and horizontal transport, particularly in coastal regions, and hence may impact bio-productivity. Daniele, (2017) showed from model studies verified against altimeter significant wave heights that current gradients can be the primary source of variability in significant wave heights at scales less than 200 km, including important variations down to 10 km.

Satellite-based scatterometers can capture wind variability on the oceanographic mesoscale, but currently lack the spatial resolution to measure wind vector variability associated with sub-mesoscale processes. In contrast, SAR observations have the potential for such small-scale studies. Although the possibility to detect, from SAR images, the surface manifestation of rolls in the atmospheric boundary layer, atmospheric fronts, convection-induced downdrafts, and surface currents has been known since a long time (Fu and Holt 1982; Sikora and Young 1995; Young and Sikora 2005), it is only recently that this potential has been exploited in a systematic and quantitative way. For example, Wang et al. (2020) analyzed atmospheric boundary layer rolls properties from 2 years of surface roughness images from the SAR of Sentinel-1A and 1B using an automated image classification. They could estimate that rolls locally induce surface wind speed fluctuations of 8%. Based on the classification of SAR image texture proposed by Wang et al. (2020), Stopa et al. (2022), showed how coherent structures identified in the SAR images of surface roughness can be used to get information on the stratification of the marine boundary layer. From a 5-year data set, they related the occurrence of shallow convective cells or wind streaks to the stratification state of the marine boundary layer, characterized by the bulk Richardson number. Ayet et al. (2021) illustrated how high-resolution images of ocean surface roughness as provided by SAR, combined with theoretical and high-resolution numerical models, can provide physical insights into the air-sea interactions happening in intense ocean frontal regions. It is anticipated that these small-scale variations winds (identified as roughness modification in the SAR images) are important for ocean biological and chemical processes (Bourassa et al. 2019), and that observations of winds at small-scales can be very useful for improving our understanding and management of ocean resources. All these studies pave the way toward a more systematic use of SAR observations to characterize the marine boundary layer, in close interaction with the ocean surface and subsurface.

Ocean winds, and in particular coastal winds, follow a diurnal cycle and furthermore, mesoscale wind phenomena in the atmosphere have an evolution lifetime of only a few hours, implying a need for 3-hourly global wind coverage for meteorological forecasting applications. Such data is needed to observe the coupling of coastal winds and currents described above. Presently, despite several scatterometers in space, a gap still exists in the temporal sampling (between 0:00 and 5:30 Local Solar Time (LST) and 12:00 and 17:30 LST). In addition, not all scatterometer missions deliver the required timeliness for regional NWP and now-casting applications. This is a subject of ongoing attention in the international meteorological community.

It is therefore evident that high spatial and temporal resolution satellite observations aid in characterizing processes, such as air-sea exchanges of energy, momentum and gases. We are presently at a stage where, to go beyond case studies on this topic, researchers are developing methodologies and analyses based on large sets of observations from a diversity of sensors and combining them with numerical approaches.



### 3.3 Contribution of Satellite Observations for Evaluating Trends and Variability of Surface Wind and Wave Parameters

While climate is changing rapidly, it is important to evaluate long-term trends and variability of a large number of parameters characterizing our planet, including surface wind and waves, which play an important role in the air/sea exchanges (and in turn, the climate evolution), contribute to the rapid modification of the polar region, and impact the wave and storm surge intensity in coastal regions.

The description of the wave climate is also critical information for a wide range of applications, including ocean and coastal engineering. Indeed, the design of any ship, offshore platform or coastal infrastructure (harbor, shipping terminal, coastal defenses against flooding, etc.) is based on the properties (height of waves, drag and inertial forces, impact forces, scouring potential, etc.) of events that may occur during the lifetime of the asset. Including safety margins, it means that the design can be based on the expected maximum wave height that occurs with a return period of 50 years, 100 years, or, for some sectors of the Dutch coast 10,000 years. Given the large interannual variability of maximum wave heights and winds, in particular in the tropics due to tropical cyclones, a 100-year return value for a wave height can be more than 30% higher than a 10-year return value, and long-time series are necessary to obtain necessary climatology of extreme events.

Of course, the modest length of satellite records cannot be the only source of information for studies on trends and variability: we only have 35 years or so for scatterometers and altimeters, a little less for SARs, and just data since 2018 for SWIM on CFOSAT. In particular, for most of the ocean, estimated trends are still impossible to separate from the interannual variability (Dobrynin et al. 2015). However, satellite observations are almost unique in providing a global verification of atmospheric and sea state models, in particular in the open ocean. These satellite observations can be used either for model bias corrections, based on remotely sensed wind speeds (Trindade et al. 2020) and wave heights (e.g., Caires and Sterl 2005) and/or use in the assimilation scheme of the reanalysis. The resultant fields are then able to be used to monitor the atmospheric and oceanic trends and variability over several decades (up to a century), with the same version of the atmospheric or oceanic model, including the same assimilation scheme of the available observations. In this context, satellites are a source of extensive and detailed measurements over long periods, provided that they can generate well-calibrated and homogeneous series of observations.

Important efforts have been deployed in recent years to reprocess and reanalyze long series of satellite wave observations (Dodet et al. 2020; Ribal and Young 2019; Timmermans et al. 2020) with a twofold objective: (1) reducing the noise of sea state parameters, and combining seamlessly different satellite sensors (standard and high-resolution altimeters, scatterometers, Synthetic Aperture Radars), (2) proving multi-decadal statistical series of both wind-sea and swell and analyzing the trends and variability in relation with large scale climate patterns, such as El Niño. The main results obtained in the last 10 years on the analysis of long time series of wind or waves observations are summarized below.

A first analysis of trends in wind speed and wave height estimated from altimeter data was carried out by Young et al. (2012). This study based on a 20-year data set evidenced some contradictions between the trends found in the 100-year return period of wind speed and that of significant wave height. It showed that longer-duration data sets were required to make more definite conclusions. Following these first attempts, important efforts have been deployed for producing cross-calibrated and validated (against in situ measurements) significant wave

heights based on multi-satellite missions over the multi-decadal history of the altimeter era (Ribal and Young 2020; Dodet et al. 2020).

Although such time series are still short for some of the climatological analyses, this is an important step forward in the use of satellite data for climatological applications. However, Timmermans et al. (2020) showed that estimating robust trends and variability in the significant wave height from these data remains a challenge: using four climatology data records, including the two satellite datasets mentioned above (Dodet et al. 2020; Ribal and Young 2020), they highlighted differences in the magnitude and distribution of the changes, demonstrating the need for further progress in the calibration and quality control of altimeter data, as well as on qualification of long time series of buoy data. Estimation of bias between different sets of observations and random errors for each type of observation also need to be carefully evaluated before these data are used for climate assessments (Dodet et al. 2022).

More generally, one must still be cautious in the interpretation of mean trends of mean and extreme values of surface wind and waves. On the one hand, as shown by Meucci et al. (2019), reanalyses may lead to spurious trends of the mean values due to the assimilation of an increasing number of observations over time. On the other hand, the global sampling by satellite observations is not homogeneous with time (more observations at the present time than in the 90 s) and not always compatible with the model sampling, at least for altimeter observations. Haoyu et al. (2020) showed in particular that the 90th and 99th percentiles of wind speed and wave height monthly distributions from altimeter observations are significantly underestimated compared to their counterpart from the ERA5 reanalysis, when the sampling of satellite data is taken into account. This issue is however slightly attenuated when analyzing annual extreme values of oceanic wind speed and wave height. Young and Ribal (2022) also show that the trends in significant wave height estimated from a multi-mission dataset are sensitive to the method of data intercalibration (altimeter versus buoys or altimeter versus altimeter).

For trends in wind speed estimated from scatterometer, Stoffelen et al. (2015) used collocation results to verify the accuracy of global climate trends from scatterometer, buoys and NWP models. They concluded that the global buoy network is insufficient to determine global trends to an accuracy of 0.1 m/s per decade (as recommended by GCOS<sup>11</sup>), while scatterometers are generally stable and able to provide such accuracy. Several groups have subsequently developed methodologies to assess the consistency multi-mission observations of winds from different scatterometer missions (Verhoef et al. 2017; Belmonte and Stoffelen 2019; Ribal and Young 2020) or from a combination of scatterometer and radiometer missions (Wentz et al. 2017; Ricciardulli et al. 2021), but there is not yet a common approach used at the international level to reprocess all the available satellite-based wind data sets.

Differences in instrumental corrections, processing, calibration and quality control still remain important sources of uncertainty in the trends in wind speed and wave height obtained with different satellite products. Given the high level of precision required to draw conclusions on climatological trends of wind speed and wave height on a global or regional scale, there are not yet definitive conclusions on this subject nor on the physical processes that could explain such trends.

<sup>11</sup> <https://gcos.wmo.int/en/essential-climate-variables/surface-wind>

## 4 Ocean and Coastal Applications

### 4.1 Context of Ocean and Coastal Applications

Containing over 97% of its water, and covering over 70% of its surface, the ocean is essential to supporting and sustaining life on Earth. It influences our weather and our climate (Schmitt 2018), is important for the provision of food and bio-resources (Naylor and Burke 2005), and integrates an economy (comprising sectors as broad as energy, health, leisure, minerals and transport) on which the future welfare and prosperity of humankind depends (OECD report 2016). Understanding ocean dynamics is therefore essential to many industries—such as shipping, hydrocarbons / renewables and fisheries—whose interests include monitoring and the modeling of wind, waves, and currents (as well as other variables) to promote more safe, efficient and successful operations and mitigate adverse impacts on navigation, exploration and coastal communities. At the same time, government agencies and coastal managers tackling the pressures of human activity in environmentally sensitive and highly urbanized nearshore areas also require information on related changes and hazards—such as coastal erosion, pollutant dispersal and water safety—to inform their own decision-making. Since most, if not all, of these requirements can be met by remote sensing techniques (McCarthy et al. 2017; Melet et al. 2020), and both the cost and the availability of satellite data has improved in recent years, measurements of wind, waves, winds and current obtained from space-borne assets are increasingly being incorporated in applications by users keen to draw on their benefits, often with high-density global coverage, collected in a near-synoptic manner.

As with any application, the choice of the optimum type of satellite data to use must be informed by the aim of the work, and the particular parameters and processes needing to be sampled and studied. This is typically dependent on a set of considerations, for example:

- The specification requirements of the application—for example, if needing optical or microwave measurements, the spectral wavebands/frequency bands of interest, as well as the spatial and temporal resolution of the data;
- The availability, cost and coverage of the data;
- The lead time from order to delivery of the data;
- The level of processing undertaken on the data;

Often, this decision is a compromise between multiple aspects, such as:

- Temporal resolution—the repeat orbit pattern determines the frequency that areas of ocean can be surveyed by an individual satellite, and sensors that measure a wide swath rather than just at nadir typically support more regular broad-scale monitoring. Very high spatial resolution satellites can often be tasked quickly, and pointed from several orbits, to increase temporal resolution, but this is a trade-off against cost;
- Spatial resolution—the correlation length scales of the parameter of interest and its associated variability are important for establishing suitability, with these also influenced by instrument design and revisit time;
- Spectral resolution—the demands of different spectral wavebands/frequency bands affect the specific features able to be detected, and sensors with higher spectral resolution typically have lower spatial resolution;

- Cost—higher resolution data is typically more expensive than lower resolution data, and the cost of more highly processed datasets are similarly more expensive than less highly processed ones;
- Expertise—The benefit of cheaper, less processed, data must be balanced with the greater time and knowledge requirement from the user alongside, potentially, the need to handle greater data volumes versus being supplied with analysis ready data.

For further information and discussion, the interested reader is referred to Lavender and Lavender (2016).

It has been acknowledged earlier in this paper (Sect. 3.1) that much of the benefit of data from satellites lies in its direct use within numerical weather and climate reanalysis/prediction models—for example, in terms of data assimilation, post-processing or verification. Example applications for specific ocean and coastal use cases, as well as example derived products and services, and discussion of future needs for these types of information are described in detail in the following parts.

## 4.2 Offshore Industry

Satellite measurements of ocean wind, waves and currents are employed across a range of applications in the offshore industry, often as one component in integrated metocean information systems (Smith 2006). Here, the use of the term ‘metocean’ acknowledges the role of both meteorology and oceanography in supporting operational planning for the maritime transport and energy sector, which are responsible for driving much of the real-time applications of Earth observation (EO) data (Le Traon et al. 2015). However, understanding changing climate conditions is also becoming increasingly important, with long time series satellite datasets complementing the use of in-situ measurements and numerical modeling for the prediction of extreme event occurrence (Takbashi et al. 2019).

Of fundamental importance to offshore applications are the data to enable:

- Ship routing and voyage planning (e.g., Davidson et al. 2009)
- Supporting critical and complex weather-sensitive activities such as cable-laying, pipe-laying, or movement of exceptional loads (e.g., Steele et al. 2021)
- Site selection, as well as the design, installation, operations/maintenance and decommissioning of offshore platforms, including hydrocarbons and renewables (e.g., Medina-Lopez et al. 2021)
- Management of production from fixed and floating platforms (e.g., Aird 2018)
- Compliance and insurance (e.g., DNV-GL AS 2018<sup>12</sup>)
- Safety of port infrastructure (e.g., Steele et al. 2019)

Since 80%, by volume, of all international trade in goods is carried by sea (UNCTD 2021), with 11 billion tons transported each year by a fleet of 62,100 vessels (UK Government 2021), routing and safety remain priority applications. For these vessels, operating on passages with more exposure to heavy weather, including trans-ocean routes, the safe and efficient progress of these vessels is necessarily dependent on accurate, real-time sea state information with high spatial and temporal resolution. Extreme winds and waves

<sup>12</sup> [https://issuu.com/dnvgi/docs/dnv\\_gl\\_annual\\_report\\_2018](https://issuu.com/dnvgi/docs/dnv_gl_annual_report_2018).

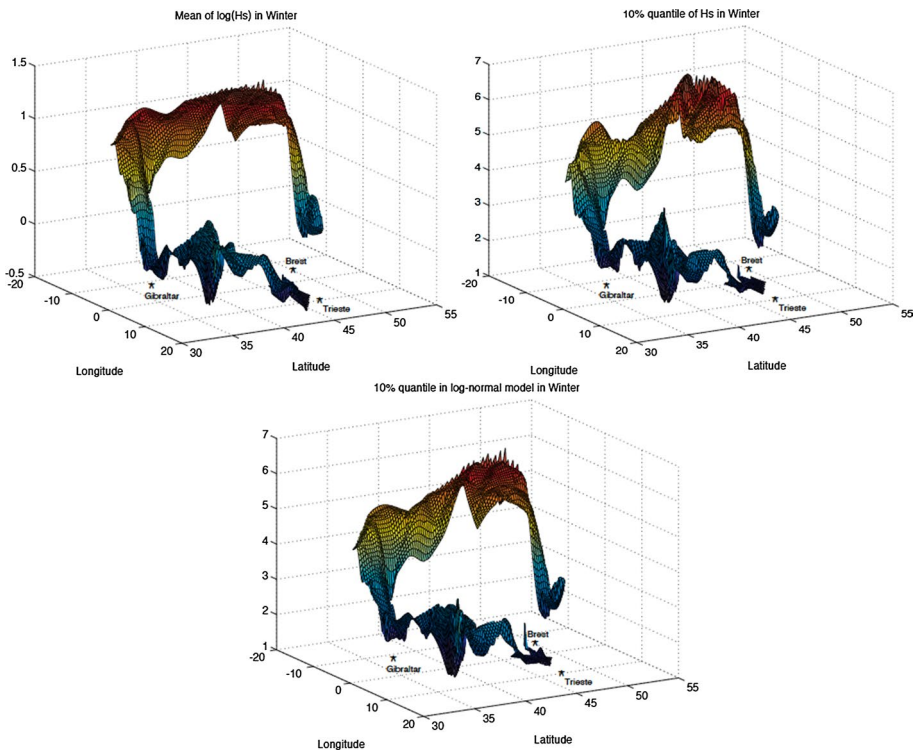


**Fig. 22** Analysis of satellite altimeter significant wave height  $H_s$  data along an example, the Rotterdam–Trieste, route. Top left: mean of  $\log(H_s)$  for winter. Top right: Estimated 10%  $H_s$  quantile for winter. Bottom: 10% quantile from a log-normal model reconstructed from data. From Cotton et al. (2000)

can directly impact on stability (particularly in combination with adverse currents), resulting in an average of 1,382 cargo containers being lost each year—with catastrophic events accounting for half of these losses (see the World Shipping Council<sup>13</sup>). At the same time, high sea state can indirectly impact the well-being and effectiveness of the crew. Mitigating the impact of adverse conditions demands effective ship routing to avoid the worst of the weather, while also potentially benefiting from advantageous surface currents to either increase speed or decrease fuel consumption on passage. Of course, the extent to which conditions may be described as excessive depends on the type of vessel and the mode of its operations—with those engaging in heavy lifting or subsea installation activities needing to adhere to strict operational weather limits. As these limits are typically very low (e.g., winds less than 15 knots or waves less than 2.5 m significant height,  $H_s$ ), and the cost of unplanned termination very high (e.g., millions of dollars for aborting a subsea cable or pipeline installation), accurate metocean information (including wind, waves and currents) is essential (Cotton et al. 2000; Steele et al. 2021). This is particularly true of vessels reliant on dynamic positioning, such as when undertaking drilling, diving or craning, as

<sup>13</sup> <https://www.worldshipping.org/news/world-shipping-council-containers-lost-at-sea-report-2022-update-published>.

these operations are sensitive to directional swells and strong currents. Meteorological and oceanographic information supporting these operations mainly relies on numerical predictions, the majority of which assimilate spaceborne data (see Sect. 3.1); for example, wind assimilated in atmospheric models which are used to force the wave prediction, or significant wave height (as well as, recently, directions and wavelengths of dominant swells) assimilated directly. Today, ocean models assimilate the geostrophic component of currents derived from altimeter missions, but not surface current estimated without assumption on geostrophy. With the development of spaceborne projects dedicated to a direct estimate of surface current, this may come in the future. Although models forced by observations are essential in this domain, several demonstrator applications also choose to directly use satellite-based ocean wave data. Cotton et al. (2000) illustrated the interest of this approach; for example, in ship design, assessing post-event damage or describing the wave climate along specific shipping routes (see Fig. 22). Providing a long time series of wave parameters from space is also important in this domain to evaluate the probability of the most extreme conditions in a changing climate era (see Sect. 3.3).

As with the global reliance on shipping, provision of energy is also critical to our modern economy. Although a sector traditionally focused on hydrocarbon extraction (i.e., sub-sea oil and gas), the power and scale of the world's ocean also make the offshore environment attractive for renewable electricity generation directly: energy from the movement of the ocean waters (from waves and tidal currents) can be converted via the use of underwater turbines and other devices, while, as on land, wind can be harnessed over the open sea—often with a higher generation potential (Kaldelis and Kapsali 2013). In terms of applications, these generation cases share many similarities with their oil and gas equivalents, including benefitting from the experience of offshore exploration and production moving to deeper waters (a much more hostile weather environment), requiring the use of floating platforms tethered to the seabed. For both the hydrocarbon and renewable industry, accurate metocean information (including winds, waves and currents) is essential across all stages of the project life cycle; from site selection, design/certification, installation, operation/maintenance to eventual decommissioning (ORSIG 2018):

- Statistics on sea state are necessary for engineering design. These are in the form of values of the return period (e.g., 1 yr, 10 yr, 50 yr, 100 yr) for relevant variables, and can be estimated by fitting statistical models to climate information derived from model reanalysis or satellite data (mainly significant wave height for this latter).
- For floating platforms that have an increased sensitivity to waves and currents, it is important to quantify the dynamic response of the structure to the environment, and so characterizing additional components, such as the full wave energy spectra, is needed. This information is derived from model reanalysis data (which generally use satellite data for assimilation and/or validation);
- Localized and high-resolution nowcasting and forecasting of metocean conditions is critical during installation, operations/maintenance and decommissioning. Again, this information is derived from model data (but may use satellite data for assimilation/validation), however, there is also a requirement for supplementing long-term knowledge of expected workable conditions (e.g., ‘weather windows’ or ‘downtime’ analysis) to support operational planning.

To maximize the relative advantages of available data types, offshore industry operators typically prefer a single source of information that integrates several original inputs. Consequently, the contribution of EO data varies between use cases, albeit these are usually



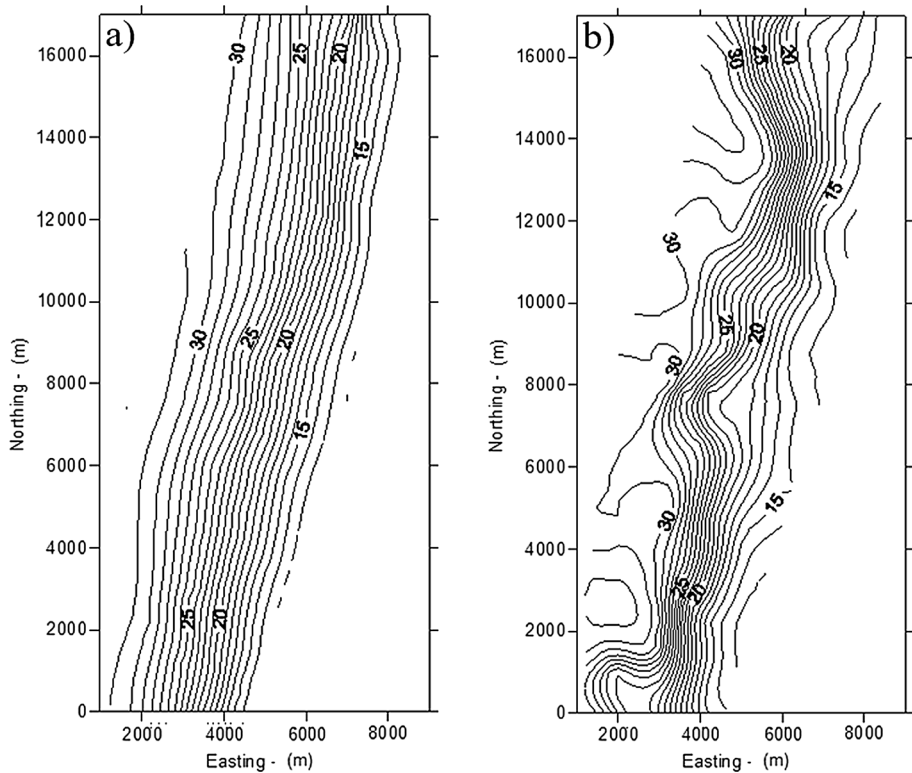


**Fig. 23** Maps of bathymetry for an study site in Western Europe (Aveiro site, northwestern Portugal) from **a** situ measurements, **b** SAR-images using the Pereira et al. (2019) method. The size of the studied domain is about 17 km in latitude (vertical axis) and 6 km in longitude (x-axis). Bathymetry contours are given every 1 m and range between 13 and 32 m. From: Salameh et al. (2019)

biased toward the earlier stages of the project life cycle. At present, the main benefit of satellite data is seen as being the capability to provide long timeseries with global coverage under all conditions, with the need for high spatial and temporal resolution data being met by models. In addition, Stevens et al. (2021) suggest further potential for these data in:

- Improving temporal consistency of reanalysis datasets;
- Reducing the swell-related uncertainty in global models;
- Supporting the validation of wave energy resource modeling, using shoreward along-track data;
- Verifying the spectral shape for early validation of deep-water modeling for floating structures;

Acknowledging that wind, waves and currents are often only part of the broader decision-making context for both the maritime and offshore industry, augmenting these data with additional complementary space-borne information (e.g., sea ice, sea-level etc.; Ranchin et al. 2020) obtained from optical (visible and thermal radiometry) and radar (SAR imaging and along-track altimetry, scatterometry) technologies have the potential for amplifying the benefit to users; particularly when data from satellites is integrated into

downstream products by combining with in-situ measurements, as well as physical, biological or socio-economic models to complement situational awareness.

### 4.3 Coastal Zone Management

The coastal zone represents the transition between the terrestrial and marine environments (Melet et al. 2020), in which the global human population, and therefore activities, are disproportionately concentrated (Small and Nicholls 2003; McGrannahan et al. 2007; Neumann et al. 2015). As such, these areas offer important services of societal, economic and biological value (Martinez et al. 2007) that, in the context of the projected increases in coastal population over the coming years, make measurements of variables affecting coastal hazards by space-borne assets an increasingly essential component of effective coastal management.

Mitigating the costly impact of flooding or loss of critical infrastructure demands accurate information about the dynamic state of the coast (e.g., sediment volume or shoreline position) to enable appropriate decisions regarding resilience and protection to be made accordingly (Davidson et al. 2007; Steele et al. 2019), with high spatial and temporal measurements of bathymetry typically a prerequisite to monitoring and modeling associated coastal changes (Holman et al. 2013; Melet et al. 2020). Traditional techniques such as land-based, ship-based and airborne surveys offer very accurate measurements of bathymetry (e.g., up to a few centimeters). However, such methods are best suited to relatively small areas and are constrained by logistical challenges and high cost (Salameh et al. 2019). In contrast, space-borne techniques offer an often convenient and cost-effective approach to collecting continuous near-synoptic measurements of bathymetry, particularly in hazardous or remote regions where the revisit time of the satellites allows storm impacts to be rapidly sampled, quantified and assessed on individual event timescales (enabling appropriate interventions to be enacted). While it is true that retrieval methods from such instruments were often based on radiative transfer modeling approaches applied to optical images, satellite observations from SAR or optical satellites are increasingly being used to estimate bathymetry relying on the inversion of the dispersion relation resulting from linear wave theory (e.g., Poupardin et al. 2016; Bergsma et al. 2019; Almar et al. 2019), or on surface features induced by interaction with bottom topography (e.g., Alpers and Hennings 1984). Figure 23 presents the bathymetry estimated by Salameh et al. (2019) from analyzing the wave transformation with depth from Sentinel-1 SAR images, using the method of Pereira et al. (2019). The relative error of the water depth compared to in situ measurements was estimated by Salameh et al. (2019) to be between 6 and 10% for water depths between 15 and 30 m. Similarly, exploiting the specificity of Sentinel-2, with two images acquired quasi-simultaneously in different spectral bands, De Michele et al. (2021) developed a method for estimating bathymetry based on the joint measurement of ocean wave celerity and wavelength, while Najar et al. (2022) recently extended this method with a machine learning approach based on both color information and wave kinematics as inputs to the deep learning model. Such data have a direct application in coastal vessel navigation, with the evolution of bathymetric contours identified from these EO information also able to be used to quantify trends in coastal variability directly (e.g., Luijendijk et al. 2018), or assimilated in coastal models (e.g., Davidson et al. 2019).

Wind and sea-state observations also have an important role in characterizing and modeling potential vulnerability, in particular due to storm surge effects (Dukhovskoy and Morey 2011; Duncan et al. 2019).

Experts in satellite data are continuing to develop methods that will increase the accuracy, resolution or repetition of wind/wave measurements/products in the coastal zone. A spatial resolution of 500 m for the wind and waves seems to be reachable from SAR and/or altimetry. They will also extend the number of variables that can be derived from space, in particular providing surface current maps from SAR (Gommenginger et al. 2019; Moiseev et al. 2022). Over the coming years, Turner et al. (2021) confidently anticipated the combined benefits of global coverage, access to an archive of routine and repeated measurements that already span several decades, and the opportunities for automated and “always on” monitoring of present conditions will further drive a substantial uptake in use of satellite data for coastal applications. Although not yet quite matching the accuracy of land-based and ship-based sensors, the continued improvement in spatial and temporal resolution of space-borne instruments promises significant potential for providing additional information and insights to inform coastal management, with advances in algorithms (including machine learning, e.g., Danilo and Melgani 2019; Sagawa et al. 2019) and the development of techniques that shift our capabilities from ‘simple’ individual snapshots of the bathymetry toward seamless three-dimensional monitoring of the complete, evolving, coastal zone (e.g., Bergsma et al. 2021) particularly exciting in this respect (Turner et al. 2021).

Of course, issues of resilience and protection are not only relevant to the built environment, but also to the management of the health of the coastal ecosystem underpinning the blue economy, as well as the safety of the communities whose livelihood and leisure largely depend on it (Rayner et al. 2019). Of fundamental importance to coastal applications are the data to support trajectory modeling in studies of transport of plankton, fish eggs and larvae to aid stock assessment (e.g., Röhrs et al. 2014); pollutant dispersion such as marine litter (e.g., van Sebille et al. 2020); oil spill tracking to assist clean-up operations (e.g., Jones et al. 2016); as well as the planning of search and rescue missions (e.g., Breivik et al. 2013), among others. Such use cases need near real-time information on surface currents and surface winds—often, in addition, waves—to properly account for the advection and modification of particles within their leeway drift predictions. EO information is either able to be processed and used as forcing for Lagrangian simulations directly, or assimilated in coastal models to predict the fate of these objects. As with all remote sensing opportunities, the increasing prevalence of large constellations of satellites promises a significant potential for providing new data.

The augmentation of wind, wave and current measurements with additional complementary space-borne information (e.g., ocean color, temperature, communications; Melet et al. 2020)—such as that used for the monitoring of the broader non-metoccean aspects affecting water quality monitoring (e.g., Chawla et al. 2020), pollutant (e.g., Viatte et al. 2020) and oil spill detection (e.g., Fingas and Brown 2018) as well as search & rescue target identification (e.g., Kanjir et al. 2018)—are essential to realizing truly integrated (and data-driven) approaches to effective coastal management. A cross-sectional view on the use of space observations to monitor and study coastal areas, estuaries and deltas is presented by Laignel et al. (2023). in this special issue.

#### 4.4 Future Prospects

In terms of both offshore industry and coastal zone management applications, it is possible to identify a several unifying priorities for the use of EO and satellite data:

- Maintaining the existing observational timeseries. Users have highlighted that a primary benefit offered by satellite data is the long (and consistent) time series that exists, with the potential to also support the application of new techniques that make use of third-party signals not originally designed for the purpose for which they can be employed.
- Providing higher spatial / temporal resolution data. Users commonly identify a need for higher resolution data, in space and time, which represents a challenge for EO acquisition, even with the increased number of satellite altimeter and SAR missions now operating. For example, Ardhuin et al. (2019c) specified the following requirements for global to regional wave climate data: 3-hourly measurements; 25 km resolution, uncertainty in SWH of 10 cm / 5% and long-term stability in SWH of 5 cm/decade. This is difficult for along-track measuring sensors, but new missions with swath measuring capability (CFOSAT, SWOT) should offer improvements.
- Development of instrumentation/techniques to support emerging / evolving requirements, such as the provision of full wave energy spectra in engineering applications.
- Augmentation with a range of measured and modeled oceanographic data, which needs to be interoperable and translatable to derive relevant metrics to support simple multivariate decision-making by non-experts; for example through integration with metocean information systems.

## 5 Conclusions

In this paper we have presented how satellites provide essential observations of wind, waves and surface currents in three domains: (1) monitoring and modelling the atmospheric and oceanic conditions at a global scale, (2) to contribute to research studies on the coupled atmosphere/ocean system, and on evaluation of the impact of climate change, (3) to support applications dedicated to users of the open and coastal ocean. With more than 30 years of satellite missions defined to measure wind, waves and currents at the ocean surface, most space-borne sensors and inversion methods can be considered as mature. However, progress is still expected in several domains thanks to interesting advances in instrumental concepts. For example, a better characterization of extreme events like tropical cyclones will be possible in the future thanks to the choice of polarimetry diversity on future wind scatterometers (with cross-polarization the most sensitive to high wind) and to a more systematic use of low-frequency microwave radiometer measurements. A better characterization of the air/sea exchanges will also be possible with missions which will simultaneously provide measurements of wind, wave surface currents (projects WacM-Odysea in the USA, Rodriguez et al. 2019), Seastar in Europe, Gommenginger et al. 2019) and eventually combined with other important parameters of the air/sea exchanges like the sea-surface temperature (Harmony project in Europe, López-Dekker et al. 2019). In parallel, the development of new inversion methods applied to the most recent altimeter or synthetic aperture radar missions, will allow better spatial resolution of sea-state parameters, which will benefit the characterization of non-homogenous conditions (coastal zones including, e.g., coral reef islands, fronts, eddies, marginal ice zone, etc.) and the associated need to protect the fragile environments under the pressure of climate change. It must also be recalled here that new perspectives are sometimes opened by new techniques applied to remotely-sensed observations not originally designed for the purpose for which they were defined. For example, the GNSS constellation of satellites primarily used for navigation,

are generating signals that are reflected off the sea surface (radio occultation and scatterometry) can be related to sea state. Multi-band optical images acquired quasi-instantaneously, such as on the Sentinel-2 mission, also offer promises opportunities for providing more systematic details on wave evolution and/or bathymetry. Lidar measurements defined for sea-ice monitoring can provide interesting by-products on waves. Finally, the development of new services based on a wide-open access to a long archive of satellite products (e.g., the Copernicus Marine Service, see Le Traon et al. 2019) will continue to facilitate the use of these observations for a wide range of applications either in research or oriented toward the blue economy.

## Appendix 1: List of sensors and satellite missions mentioned in this paper

In the Table of this Appendix, we provide the list of sensors and satellite missions mentioned in the paper and include the name of agencies responsible of the sensors, as well as the period of measurements.

More details can be found in the data base maintained by the CEOS (Committee on Earth Observation Satellites) (<http://database.eohandbook.com/>).

Platform Acronym	Instruments mentioned in the text	instrument agency, country	Start/end Dates
ADEOS-I	NSCAT (NASA Scatterometers)	USA	1996–1997
ADEOS-II (Advanced Earth Observing Satellites)	Quikscat		2002–2003
Aqua	AMSRE (Advanced Microwave Scanning Radiometer EOS)	NASA (USA) and JAXA (Japan)	In operation since 2002
CFOSAT (China France Oceanography SATellite)	SWIM (Surface Waves Investigation and Monitoring) SCAT (Scatterometer)	CNES (France) and CNSA (China)	In operation since 2018
Coriolis	Windsat	DoD (USA)	2003–2020
Cryosat-2	SIRAL (SAR Interferometer Radar Altimeter)	ESA (Europe)	In operation since 2010
CYGNSS	DDMI (Delay Doppler Mapping Instrument)	NASA & NOAA (USA)	In operation since 2016
DMSP, (Defense Meteorological Satellite)-satellite series F	SSM/I Special Sensor Microwave Imager on F-8 to F-15 SSM/IS Special Sensor Microwave-Imager / Sounder on F16–F19	NOAA and DoD (USA)	Successive satellites in operation since 1987
Envisat	ASAR (Advanced SAR) Radar altimeter	ESA	2002–2012
ERS-1/2 (European Remote Sensing Satellites -1/2)	SAR, altimeter	ESA	1991–2000

Platform Acronym	Instruments mentioned in the text	instrument agency, country	Start/end Dates
FY3-E, FY3-H, FY3-I	WindRAD (Wind Radar)	CNSA (China)	In operation since 2021
GCOM (Global Change Observation Mission-Water)	AMSR2 (Advanced Microwave Scanning Radiometer 2)	JAXA (Japan)	In operation since 2012
GFO (Geosat Follow-on)	Radar altimeter	NASA (USA)	1998–2008
GPM (Global Precipitation mission)	GMI (GMP Microwave imager)	NASA (USA)	In operation since 2014
Harmony	Passive Synthetic Aperture Radar	ESA (Europe)	Launch expected in 2029
HY2	ALT (Radar Altimeter) SCAT (Scatterometer)	CNSA (China)	In operation since 2021
HydroGNSS	GNSS Reflectometer	ESA (Europe), UKSA (UK)	Launch expected in 2024
Icesat-2 (Ice, Cloud, and land Elevation Satellite 2)	ATLAS (Advanced Topographic Laser Altimeter System)	NASA (USA)	In operation since 2018
ISS (International space station)	RapidScat	NASA (USA)	2014–2016
Jason 1 to 3	Altimeters POSEIDON -2 (Jason-1), POSEIDON-3 (Jason-2), POSEIDON-3B (Jason-3)	CNES (France)	Jason 1: 2011–2013 Jason 2: 2008–2019 Jason 3: in operation since 2016
Metop A-B-C	ASCAT (Advanced Scatterometer)	EUMETSAT, ESA (Europe)	Metop-A: 2006–2021 Metop-B: In operation since 2012 Metop-C: In operation since 2018
Oceansat-2	Scatterometer	ISRO (India)	In operation since 2009
Oceansat-3			In operation since 2022
QuikSCAT	Seawinds scatterometer	NASA (USA)	1999–2018
RADARSAT- 1	Synthetic Aperture Radar	CSA (Canada)	1994–2013
RADARSAT-2			In operation since 2007
SARAL	AltiKa (Ka-band Altimeter)	CNES (France)	In operation, since 2013
Scatsat-1	Scatsat-1	ISRO (India)	2016–201
Seasat	SAR, altimeter, Scatterometers Radiometer SMMR (Scanning Multi-Channel Microwave Radiometer)	NASA (USA)	1978- 1978
Seastar	SAR (squinted along-track interferometry)	ESA (Europe)	Under study for an Earth Explorer satellite (Phase 0)
Sentinel-1 (A-B-C-D..)	SAR	ESA (Europe)	Series started in 2014
Sentinel-2 (A-B-C-D...)	Optical multi-spectral Instrument	ESA (Europe)	Series started in 2015
Sentinel-3 (1-B-C-D..)	SAR radar altimeter (SRAL)	ESA (Europe)	Series started in 2016



Platform Acronym	Instruments mentioned in the text	instrument agency, country	Start/end Dates
Sentinel-6 Michael Freilich (A-B)	Poseidon-4 SAR Radar Altimeter	ESA (Europe) & CNES (France)	Operational since 2020
SKIM	Doppler near-nadir incidence scatterometer	ESA (Europe)	Abandoned (proposed as an Earth Explorer satellite)
SMAP Soil Moisture Active Passive	L-Band Radiometer	NASA (USA) & CSA (Canada)	Operational since 2015
SMOS Soil Moisture and Ocean Salinity	Microwave Imaging Radiometer using Aperture Synthesis (MIRAS)	ESA (Europe)	Operational since 2009
SWOT Surface Water Ocean Topography	Ka-band Radar Interferometer (KaRIN)—Interferometric altimeter	NASA (USA) and CNES (France)	Launch planned in 2023
Tandem-X	SAR	DLR (Germany)	In operation since 2010
TerraSAR-X	SAR	DLR (Germany)	In operation since 2007
Topex	Altimeters (Topex and Poseidon-1)	NASA (USA) and CNES (France)	1992–2006

## Appendix 2: Principles of wave estimation from SAR images

Effects and properties that contribute to the formation and/or the degradation of satellite SAR ocean wave images are summarized here-below:

- *Tilt modulation* variation in backscatter due to the local modification of the relative incidence angle by long wave slopes. The longer waves locally modify the exact plane of incidence, producing a local change in cross section (following the geometrical characteristics of the instrument).
- *Hydrodynamic modulation* variation in backscatter due to the non-uniform distribution of scatterers (i.e., short waves) along a long wave profile. Existing parameterizations of this phenomenon are still subject of on-going active research efforts and usually follow weakly nonlinear theory solutions (Alpers et al. 1981; Alpers and Hasselmann 1978; Hasselmann and Hasselmann 1991). Because the radar cross section at medium incidence (typically 10–25°) is not very sensitive to the short waves, the hydrodynamic effect on the signal modulation can be generally neglected for observations at these incidence angles.
- *Constructive azimuth velocity bunching* deterministic misregistrations in the azimuth direction, associated with long wave orbital motions, leading to an apparent constructive redistribution of the backscatter intensity along the azimuth direction.
- *Destructive azimuth velocity bunching* random misregistrations in the azimuth direction, associated with long wave orbital motions, leading to possible significant degradation in the azimuth resolution, leading to distortions of the resulting SAR ocean image spectra (nonlinear relationship between SAR image spectra and ocean wave spectra).
- *Range elevation bunching* misregistrations associated with long wave slope variations. When the angle of incidence is smaller than the slope of the waves (i.e., for incidence

angles of a few degrees, depending on sea-state) the iso-range plane of the radar signal may cut the rough surface at multiple points, like a long surfboard in choppy seas. This induces misregistrations which are proportional to the surface elevation and depend on the nominal instrument incidence angle. However, it is acknowledged that this range bunching effect can be neglected for observations at incidence angles larger than about  $10^\circ$  (Jackson 1981).

- *Acceleration smearing* in the SAR image associated with relative scatterer velocity changes during the SAR integration time.
- *Azimuth smearing* reduced along-track resolution associated with both the unresolved random scatter motions and the limited scatter lifetime during the SAR integration time (finite scene coherence time).
- *Speckle* multiplicative noise in the SAR images due to the coherent processing. Its statistical characteristics will depend upon the chosen look summation technique. The inter-correlation (cross-spectral) technique will help to almost entirely remove the speckle distribution in the spectral domain.
- *System transfer function* point target response characteristics that lead to varying sensitivity over the spectral domain.

The tilt ( $T_m^{\text{tilt}}$ ), the hydrodynamic ( $T^{\text{hydr}}$ ) and the range elevation bunching ( $T^{\text{rb}}$ ) are the dominant processes contributing to the Real Aperture Modulation (RAR) function  $T_m^{\text{RAR}}$ :

$$T_m^{\text{RAR}} = T_m^{\text{tilt}} + T^{\text{hydr}} + T^{\text{rb}} \quad (15)$$

Applying the Bragg approximation for the short waves on a two-scale scattering model, based on a geometric optical solution for a perfect conducting surface: the linear backscatter RAR modulation transfer function (MTF) can be separated into two parts, one geometrical MTF caused by surface tilting and one MTF caused by hydrodynamic interactions. Under this assumption, the right-hand side terms of (Eq. 15) can be expressed as a function of radar parameters (incidence, polarization), surface parameters (wavenumber of the tilting waves), and relaxation rate of the Bragg waves (Alpers et al. 1981; Alpers and Hasselmann 1978; Hasselmann and Hasselmann 1991).

An alternative semi-parametric model of the RAR MTF has been proposed to retrieve ocean wave spectra from SAR images (see Johnsen et al. (2022)). It makes use of an empirical GMF function (the so-called CMOD GMF) to relate the  $\sigma_m$  observations to wind speed (Stoffelen et al. 1997; 2017a). This technique is sought to avoid uncertainty associated with the use of a pure-Bragg scattering model, and offers an efficient alternative for C-band SAR data. In this model, the RAR MTF amplitude is proportional to the local derivative of relative cross section along the long wave phase, and explicitly dependent on the wind field through the CMOD function:

$$T_m^{\text{RAR}}(\underline{k}) = \frac{1}{\sigma_m} \frac{\partial \sigma_m}{\partial \theta} \cdot \left\{ ik_x + \frac{k_x^2}{|\underline{k}|} \tan \theta \right\} \quad (16)$$

where  $\underline{k}_r$  is the radar wavenumber vector,  $k_x$  its component along the range-direction,  $\theta$  is the radar beam incidence, and  $\sigma_m$  is the CMOD radar cross-section model function.

To complete the SAR imaging mechanism, the induced Doppler shifts, mainly associated with the longer wave orbital velocity field, must be considered as a very crucial mapping process. This is the velocity bunching mechanism. The motion effect strongly influences the SAR imaging mechanism by affecting the complex backscatter signals.

Doppler shifts associated with the longer wave orbital velocities can also potentially contribute to an additional constructive modulation mechanism (Alpers et al. 1981). In such a case, the so-called velocity bunching mechanism may help to image swell wave components in the along-track direction. This constructive mechanism is especially efficient under low wind conditions (relatively deterministic phase component redistribution). The velocity bunching effect is controlled by the range-to-velocity ratio and the relative radial component of the scatterers' velocity. The corresponding azimuth position shift of the scatterer is given as (Alpers and Rufenach 1981):

$$\xi_y = \frac{R}{V} U_r \quad (17)$$

where  $R$  is the range distance from satellite to target,  $V$  is the satellite velocity,  $U_r$  is the orbital velocity of the target projected into the radar look direction. The velocity bunching mechanism is fully controlled by the non-dimensional azimuth wavenumber,  $k_y \equiv k_y \rho_{\xi_y, \xi_y}(0)^{1/2}$ , where  $\rho_{\xi_y, \xi_y}$  is the covariance function of the azimuth shift  $\xi_y$ , and  $k_y$  is the wavenumber component in azimuth direction (Krogstad 1992). In the case of small to moderate  $k_y$ , the imaging is constructive and the velocity bunching MTF can be written as (Alpers et al. 1981):

$$T^{\text{vel}}(\underline{k}) = \frac{R}{V} \omega_{|\underline{k}|} \left\{ \frac{k_x}{|\underline{k}|} \sin \theta + i \cos \theta \right\} \quad (18)$$

A breakthrough in understanding SAR ocean wave imaging was achieved with the paper by Hasselmann and Hasselmann (1991) introducing a closed form expression relating the underlying 2D ocean wave spectra to the 2D SAR image spectra, taking into account both real aperture and velocity bunching mechanisms. This closed form expression was denoted **“the ocean-to-SAR spectral transform.”** This derivation was later elegantly reformulated by Krogstad (1992), and used to study the nonlinearity of the SAR wave imaging process. Finally, the next breakthrough was achieved when the formalism of Krogstad (1992) was extended by Engen and Johnsen (1995) to provide a closed form of the **ocean-to-SAR cross-spectral transform**. This work, which takes into account the entire wave phase velocity field is also of fundamental importance in the SAR measurements, as earlier shown on airborne SAR imagery by Vachon and Raney (1991). Engen and Johnsen (1995) defined the cross-spectra between two intensity-detected looks as:

$$P_{\text{SAR}}(\underline{k}, \tau) = \frac{1}{\langle I^{(1)} \cdot I^{(2)} \rangle} \langle I^{(1)}\left(\underline{k}, \frac{\tau}{2}\right) \cdot I^{(2)}\left(\underline{k}, -\frac{\tau}{2}\right) \rangle \quad (19)$$

where  $I^{(1)}\left(\underline{k}, \frac{\tau}{2}\right)$  and  $I^{(2)}\left(\underline{k}, -\frac{\tau}{2}\right)$  are the Fourier transforms of the two intensity detected look images, and  $\tau$  is the look separation time. Even for the short integration time ( $\tau = 0.8\text{s}$ ) of standard spaceborne SAR stripmap modes, a significant phase shift  $\left(\omega_{|\underline{k}|} \cdot \tau\right)$  is achieved for the long wavelengths of the spectra.

The ocean-to-SAR cross-spectra formalism enables, on the one hand, the elimination of the speckle noise contribution (Engen and Johnsen 1995) and, on the other hand, the removal of the  $180^\circ$  directional ambiguity of the imaged harmonic wave components. Such a crucial breakthrough concerning the potential use of cross-spectral analysis between SAR individual looks is now commonly adopted to improve the analysis of

SAR ocean wave data. The methodology shows that the exact propagation direction of swell systems is achieved for 90% of the measurements (as long as the signal-to-noise ratio is sufficiently high). Such a methodology has been fully validated, was applied to the Envisat ASAR Wave Mode (WM) and now also to the Copernicus Sentinel-1 WV mode images.

The general expression of the ocean-to-SAR cross-spectral transform can be written as (Engen and Johnsen 1995):

$$P(\underline{k}, \tau) \approx \frac{1}{(2\pi)^2} \int d\underline{x} e^{-i\underline{k} \cdot \underline{x}} e^{k_y^2 (\rho_{\xi_y \xi_y}(\underline{x}, \tau) - \rho_{\xi_y \xi_y}(0, 0))} \{1 + \rho_{II}(\underline{x}, \tau) - \delta(\underline{x})\} \quad (20)$$

where  $\rho_{II}$  is the covariance function of the RAR image, and  $\tau$  is the inter look-separation time.

From (20), a simplified quasi-linear version can be derived as:

$$P^{\text{qlin}}(\underline{k}, \tau) = \frac{1}{2} e^{-k_y^2 \rho_{\xi_y \xi_y}(0, 0)} \left\{ |T(\underline{k})|^2 e^{-i\omega|\underline{k}| \tau} S(\underline{k}) + |T(-\underline{k})|^2 e^{+i\omega|\underline{k}| \tau} S(-\underline{k}) \right\} \quad (21)$$

where  $T(\underline{k})$  is the total SAR MTF written as:

$$T(\underline{k}) = ik_x T^{\text{rb}}(\underline{k}) + ik_y T^{\text{vel}}(\underline{k}) + T^{\text{tilt}}(\underline{k}) + T^{\text{hydr}}(\underline{k}) \quad (21)$$

The nonlinearity of the velocity bunching is manifested as an exponential azimuth cut-off (the exponential term of Eq. (21)), causing a strong filtering of the azimuth wave components. The azimuth cutoff is related to the azimuth Doppler shift covariance, which can be written in terms of the underlying wave spectra  $S(\underline{k})$  as:

$$\rho_{\xi_x \xi_y}(0, 0) = \frac{1}{2\pi} \int d\underline{k} |T^{\text{vel}}(\underline{k})|^2 S(\underline{k}) \quad (23)$$

As indicated by Eqs. (17) and (18), the azimuth cutoff is governed by the satellite  $R/V$  ratio and the sea state (or alternatively the wind speed).

Subsequent to the development of the ocean-to-SAR spectral transforms, different inversion algorithms were developed (Engen et al. 1994; Hasselmann et al. 1996; Engen et al. 2000; Mastenbroek and de Valk 2000; Schulz-Stellenfleth 2005; Collard et al. 2005; Shao et al. 2015). Such retrieval algorithms generally attempt to reconstruct the a priori ocean wave spectrum by minimizing the difference between the theoretical SAR image spectra of Eq. (19) and the satellite observed SAR image spectra of Eq. (22). However, as a consequence of the exact derivative of the nonlinear transform being too cumbersome compute, most of these inversion schemes ignore the complete nonlinear mapping or represent it through a stochastic model (Schulz-Stellenfleth 2005).

Alternatively, it is possible to derive the wave spectra directly from the quasi-linear transform (see Eq. (21)). This requires that the azimuth cutoff be well estimated and that the nonlinearity of the SAR image spectra is removed from the observed SAR image cross-spectra. This nonlinearity is driven by the wind field and can be predicted simply by taking the difference between the full and the quasi-linear transform,  $P^{\text{nlin}} = P - P^{\text{qlin}}$ . This is the approach implemented in both the ASAR Envisat Wave Mode Level 2 and the Sentinel-1 WV Level 2 processors, where the  $P^{\text{nlin}}$  is provided in a look-up table as a function of wind speed, wind direction, and wave age.

**Funding** J. Knaff's funding is provided by National Oceanic and Atmospheric Administration (NOAA). The views, opinions, and findings contained in this report are those of the authors and should not be construed as an official National Oceanic and Atmospheric Administration or U.S. Government position, policy, or decision. The Office of Naval Research (ONR) has provided funding for C. Sampson through Program Element 0603207N.

## Declarations

**Conflict of interest** The authors do not have financial nor non-financial conflict of interest to declare.

**Open Access** This article is licensed under a Creative Commons Attribution 4.0 International License, which permits use, sharing, adaptation, distribution and reproduction in any medium or format, as long as you give appropriate credit to the original author(s) and the source, provide a link to the Creative Commons licence, and indicate if changes were made. The images or other third party material in this article are included in the article's Creative Commons licence, unless indicated otherwise in a credit line to the material. If material is not included in the article's Creative Commons licence and your intended use is not permitted by statutory regulation or exceeds the permitted use, you will need to obtain permission directly from the copyright holder. To view a copy of this licence, visit <http://creativecommons.org/licenses/by/4.0/>.

## References

- Abdalla S (2012) Ku-band radar altimeter surface wind speed algorithm. *Mar Geodesy* 35(sup1):276–298
- Abdalla S, Bidlot J, Janssen PA (2004) Assimilation of ERS and ENVISAT wave data at ECMWF. *Proceedings ENVISAT-ERS Symposium*, Salzburg
- Abdalla S, Dinardo S, Benveniste J, Janssen PAEM (2018) Assessment of CryoSat-2 SAR mode wind and wave data. *Adv Space Res* 62(6):1421–1433
- Abdalla S, Bidlot J-R, Janssen PAEM (2006) Global Validation and assimilation of ENVISAT ASAR wave mode spectra. *Proceedings SeaSAR 2006*, 23–26 Jan. 2006, Frascati, Italy, (ESA SP-613, Apr. 2006)
- Abdalla S, Janssen PA, Bidlot J-R (2010) Envisat ASAR wave mode spectra global validation and assimilation. *Proceedings "SeaSAR 2010"* Frascati, Italy, 25–29 January 2010 (ESA SP-679, April 2010)
- Ablain M, Meyssignac B, Zawadzki L, Jugier R, Ribes A, Spada G, Benveniste J, Cazenave A, Picot N (2019) Uncertainty in satellite estimates of global mean sea-level changes, trend and acceleration. *Earth Syst Sci Data* 11(3):1189–1202
- Aird P (2018) *Deepwater drilling: well planning, design, engineering, operations and technology application*. Gulf Professional Publishing, Cambridge
- Almar R, Bergsma EWJ, Maisongrande P, de Almeida LPM (2019) Wave-derived coastal bathymetry from satellite video imagery: a showcase with pleiades persistent mode. *Remote Sens Environ* 231:111263. <https://doi.org/10.1016/j.rse.2019.111263>
- Alpers W, Hasselmann K (1978) The two-frequency microwave technique for measuring ocean wave spectra from an airplane or satellite. *Boundary Layer Meteorol* 13:215–230
- Alpers W, Hennings I (1984) A theory of the imaging mechanism of underwater bottom topography by real and synthetic aperture radar. *J Geophys Res* 89(C6):10529–10546
- Alpers WR, Rufenach CL (1981) The effect of orbital motions on synthetic aperture radar imagery of ocean waves. *IEEE Trans Antennas Propag* 27(C7):685–690
- Alpers WR, Ross DB, Rufenach CL (1981) On the detectability of ocean surface waves by real and synthetic aperture radar. *J Geophys Res* 86(C7):6481–6498
- Angelova M (2002) *Whitecaps, sea-salt aerosols, and climate*. University of Delaware, Lewes
- Anthony EJ (2015) Wave influence in the construction, shaping and destruction of river deltas: a review. *Mar Geol* 361:53–78. <https://doi.org/10.1016/j.margeo.2014.12.004>
- Aouf L, Lefèvre J-M, Hauser D (2006) Assimilation of directional wave spectra in the wave model WAM: an impact study from synthetic observations in preparation to the SWIMSAT satellite mission. *J Atmos Oceanic Tech* 23(3):448–463
- Aouf L, Dalphiné A, Hauser D, Delaye L, Tison C et al (2019) On the assimilation of CFOSAT wave data in the wave model MFWAM: verification phase. *IEEE Int Geosci Remote Sens Symp*. <https://doi.org/10.1109/IGARSS.2019.8900180>
- Aouf L, Hauser D, Chapron B, Toffoli A, Tourrain C, Peureux C (2021) New directional wave satellite observations: towards improved wave forecasts and climate description in Southern Ocean. *Geophys Res Lett*. <https://doi.org/10.1029/2020GL091187>

- Aouf L, Lefèvre J-M (2012) On the impact of ASAR wave spectra in the operational wave model MFWAM. In: Proceedings of SEASAR 2012. ESA, Tromsø
- Aouf L, Phalippou L (2015) On the signature of swell for the Cryosat-2 SAR-mode wave data, Ocean Surface Topography Science Team Meeting 2015, Reston, Oct. 20–Oct. 23. Available online at [https://meetings.avisio.altimetry.fr/fileadmin/user\\_upload/tx\\_ausycslsminar/files/OSTST2015/IPM-02-ostst\\_Aouf\\_sarmode\\_2015\\_1.pdf](https://meetings.avisio.altimetry.fr/fileadmin/user_upload/tx_ausycslsminar/files/OSTST2015/IPM-02-ostst_Aouf_sarmode_2015_1.pdf).
- Aouf L, Law-Chune S, Hauser D, Chapron B, Tourain C, Le Baron G (2022) On the improvement of ocean/wave coupling with CFOSAT directional wave observations. Communication at the OSTST Meeting. [https://ostst.avisio.altimetry.fr/fileadmin/user\\_upload/OSTST2022/Presentations/CFO2022-On\\_the\\_improvement\\_of\\_ocean\\_wave\\_coupling\\_with\\_CFOSAT\\_directional\\_wave\\_observations.pdf](https://ostst.avisio.altimetry.fr/fileadmin/user_upload/OSTST2022/Presentations/CFO2022-On_the_improvement_of_ocean_wave_coupling_with_CFOSAT_directional_wave_observations.pdf)
- Apel JR (1994) An improved model of the ocean surface wave vector spectrum and its effects on radar backscatter. *J Geophys Res Oceans* 99(C8):16269–16291. <https://doi.org/10.1029/94JC00846>
- Ardhuin F, Marié L, Rascle N, Forget P, Roland A (2009a) Observation and estimation of Lagrangian, Stokes, and Eulerian currents induced by wind and waves at the sea surface. *J Phys Oceanogr* 39(11):2820–2838. <https://doi.org/10.1175/2009JPO4169.1>
- Ardhuin F, Chapron B, Collard F (2009b) Observation of swell dissipation across oceans. *Geophys Res Lett*. <https://doi.org/10.1029/2008GL037030>
- Ardhuin F, Rogers E, Babanin AV, Filipot J-F et al (2010) Semiempirical dissipation source functions for ocean waves Part i: definition, calibration, and validation. *J Phys Oceanogr* 40(9):1917–1941. <https://doi.org/10.1175/2010JPO4324.1>
- Ardhuin F, Collard F, Chapron B, Girard-Ardhuin F, Guitton G, Mouche A, Stopa JE (2015) Estimates of ocean wave heights and attenuation in sea ice using the SAR wave mode on Sentinel-1A. *Geophys Res Lett* 42(7):2317–2325. <https://doi.org/10.1002/2014GL062940>
- Ardhuin F, Gille ST, Menemenlis D, Rocha CB, Rascle N, Chapron B, Gula J, Molemaker J (2017) Small-scale open ocean currents have large effects on wind wave heights. *J Geophys Res Oceans* 122(6):4500–4517
- Ardhuin F, Aksenov Y, Benetazzo A, Bertin L, Brandt P et al (2018) Measuring currents, ice drift, and waves from space: the Sea surface Kinematics Multiscale Monitoring (SKIM) concept. *Ocean Sci* 14:337–354. <https://doi.org/10.5194/os-14-337-2018>
- Ardhuin F, Brandt P, Gaultier PM, Donlon C et al (2019a) SKIM, a candidate satellite mission exploring global ocean currents and waves. *Front Mar Sci*. <https://doi.org/10.3389/fmars.2019a.00209>
- Ardhuin F, Chapron B, Maes C, Romeiser R, Gommenginger C, Cravatte S, Morrow R, Donlon C, Bourassa M (2019b) Satellite Doppler observations for the motions of the oceans. *Bull Am Meteorol Soc*. <https://doi.org/10.1175/BAMS-D-19-0039.1>
- Ardhuin F, Stopa JE, Chapron B, Collard F, Husson R, Jensen RE, Johannessen J, Mouche A, Passaro M, Quartly GD, Swail V, Young I (2019c) Observing sea states. *Front Mar Sci*. <https://doi.org/10.3389/fmars.2019c.00124>
- Ardhuin F, Otero M, Merrifield S, Grouazel A, Terrill E (2020) Ice breakup controls dissipation of wind waves across southern ocean sea ice. *Geophys Res Lett*. <https://doi.org/10.1029/2020GL087699>
- Ardhuin F, Alday M, Yurovskaya M (2021) Total surface current vector and shear from a sequence of satellite images: effect of waves in opposite directions. *J Geophys Res Oceans* 126(7):e2021JC017342
- Ayet A, Rascle N, Chapron B, Couvreur F, Terray L (2021) Uncovering air-sea interaction in oceanic submesoscale frontal regions using high-resolution satellite observations. *US CLIVAR variations*, Fall 2021, Vol. 19(1), <https://indd.adobe.com/view/f410826b-6bb1-486d-b8da-6a89e7351324>
- Babanin AV, Ganopolski A, Phillips WR (2009) Wave-induced upper-ocean mixing in a climate model of intermediate complexity. *Ocean Model* 29(3):189–197. <https://doi.org/10.1016/j.ocemod.2009.04.003>
- Bamler R (1991) Doppler frequency estimation and the Cramer-Rao bound. *IEEE Trans Geosci Remote Sens* 29(3):7854
- Barrick DE (1968) Relationship between slope probability density function and the physical optics integral in rough surface scattering. *Proc IEEE (letters)* 56:1728–1729
- Bauer P, Thorpe A, Brunet G (2015) The quiet revolution of numerical weather prediction. *Nature* 525:47–55. <https://doi.org/10.1038/nature14956>
- Beckmann P, Spizzichino A (1963) The scattering of electromagnetic waves from rough surfaces. MacMillan Editor
- Belmonte RM, Stoffelen A (2019) Characterizing ERA-Interim and ERA5 surface wind biases using ASCAT. *Ocean Sci* 15:831–852. <https://doi.org/10.5194/os-15-831-2019>
- Belmonte-Rivas M, Stoffelen A, Verspeek J, Verhoef A, Anderson NXC (2017) Cone metrics: a new tool for the intercomparison of scatterometer records. *IEEE J Select Top Appl Earth Obs Remote Sens* 10(5):2195–2204



- Benveniste J, Cazenave A, Vignudelli S, Fenoglio-Marc L, Shah R et al (2019) Requirements for a coastal zone observing system. *Front Mar Sci*. <https://doi.org/10.3389/fmars.2019.00348>
- Bergsma EWJ, Almar R, Maisongrande P (2019) Radon-augmented Sentinel 2 satellite imagery to derive wave-patterns and regional bathymetry. *Remote Sens* 11(16):1918. <https://doi.org/10.3390/rs11161918>
- Bergsma EWJ, Almar R, Rolland A, Binet R, Brodie KL, Bak S (2021) Coastal morphology from space: a showcase of monitoring the topography-bathymetry continuum. *Rem Sens Env* 261:112469
- Berrisford P, Dee DP, Poli P, Brugge R, Fielding M, Fuentes M, Kållberg PW, Kobayashi S, Uppala S, Simmons A (2011) The ERA-Interim archive. ECWF ERA Report Series. <https://www.ecmwf.int/node/8174>
- Bespalova EA, Veselov VM, Gershenzon VE, Militskiy YA, Mirovskiy VG, Pokrovskaya IV, Raev MD, Semin AG, Smirnov NK, Skachkov VA, Trokhimovski YG, Hapin YB, Chistyakov VN, Sharkov EA, Etkin VS (1982) Surface wind velocity determination from the measurements of the polarization anisotropy of microwave emission and backscatter. *Soviet J Remote Sens* 1:121–131
- Biról F, Léger F, Passaro M, Cazenave A, Niño F, Calafat FM, Shaw A, Legeais J-F, Gouzenes Y, Schwatke C, Benveniste J (2021) The X-TRACK/ALES multi-mission processing system: new advances in altimetry towards the coast. *Adv Space Res* 67(8):2398–2415
- Born GH, Dunne JA, Lame DB (1979) Seasat mission overview. *Science* 204(4400):1405–1406. <https://doi.org/10.1126/science.204.4400.1405>
- Bourassa M, Meissner T et al (2019) Remotely sensed winds and wind stresses for marine forecasting and ocean modeling. *Front Mar Sci*. <https://doi.org/10.3389/fmars.2019.00443>
- Boy F, Desjonquères J-D, Picot N, Moreau T, Raynal M (2016) CryoSat-2 SAR-mode over oceans: processing methods, global assessment, and benefits. *IEEE Trans Geosci Remote Sens* 55(1):148–158
- Breivik Ø, Allen AA, Maisondieu C, Olagnon M (2013) Advances in search and rescue at sea. *Ocean Dyn* 63:83–88. <https://doi.org/10.1007/s10236-012-0581-1>
- Breivik Ø, Mogensen K, Bidlot J-R, Alonso Balmaseda M, Janssen PAEM (2015) Surface wave effects in the NEMO ocean model: forced and coupled experiments. *J Geophys Res Oceans* 120(4):2973–2992. <https://doi.org/10.1002/2014JC010565>
- Brennan MJ, Hennon CC, Knabb RD (2009) The operational use of QuikSCAT ocean surface vector winds at the National hurricane center. *Weather Forecast* 24:625–645
- Brivoal T (2021) Une modélisation alternative haute résolution du couplage air-mer et de ses effets sur la dynamique océanique dans l'Atlantique Nord-Est. PhD thesis, Université Toulouse 3 Paul Sabatier, pp 199
- Brown G (1977) The average impulse response of a rough surface and its applications. *IEEE Trans Antennas Propag* 25(1):67–74
- Brown GS (1990) Quasi-specular scattering from the air-sea interface. In: Geernaert GL, Plant WJ (eds) *Surface waves and fluxes Volume II—remote sensing*. Kluwer Academic Press, Cham
- Brumer SE, Zappa CJ, Blomquist BW, Fairall CW, Cifuentes-Lorenzen A, Edson JB et al (2017) Wave-related reynolds number parameterizations of CO<sub>2</sub> and DMS transfer velocities. *Geophys Res Lett* 44(19):9865–9875. <https://doi.org/10.1002/2017gl074979>
- Bu Jinwei Yu, Kegen ZY, Nijia Q, Jun C (2020) Developing and testing models for sea surface wind speed estimation with GNSS-R delay Doppler maps and delay waveforms. *Remote Sens* 12:3760. <https://doi.org/10.3390/rs12223760>
- Buchhaupt C, Fenoglio L, Becker M, Kusche J (2021) Impact of vertical water particle motions on focused SAR altimetry. *Adv Space Res* 68(2):853–874
- Bye JAT (1986) Momentum exchange at the sea surface by wind stress and understress. *Q J R Meteorol Soc* 112(472):501–510. <https://doi.org/10.1002/qj.49711247212>
- Caires S, Sterl A (2005) 100-year return value estimates for ocean wind speed and significant wave height from the ERA-40 data. *J Clim* 18(7):1032–1048. <https://doi.org/10.1175/jcli-3312.1>
- Caires S, Marseille GJ, Verlaan M, Stoffelen A (2018) North Sea wave analysis using data assimilation and mesoscale model forcing winds. *J Waterway Port Coast and Ocean Eng*. [https://doi.org/10.1061/\(ASCE\)WW.1943-5460.0000439](https://doi.org/10.1061/(ASCE)WW.1943-5460.0000439)
- Calafat F, Cipollini P, Bouffard J, Snaith H, Féménias P (2017) Evaluation of new CryoSat-2 products over the ocean. *Remote Sens Environ* 191:131–144
- Cardinali C (2009) Monitoring the observation impact on the short-range Forecast. *Q J R Meteorol Soc* 135:239–250. <https://doi.org/10.1002/qj.366>
- Carter D, Challenor P, Srokosz M (1992) An assessment of Geosat wave height and wind speed measurements. *J Geophys Res Oceans* 97(C7):11383–11392
- Caudal G, Hauser D, Valentin R, Le Gac C (2014) KuROS: a new airborne Ku-band Doppler radar for observation of surfaces. *J Atmos Ocean Technol* 31(10):2223–2245

- Cavaleri L, Fox-Kemper B, Hemer M (2012) Wind waves in the coupled climate system. *Bull Am Meteor Soc* 93(11):1651–1661. <https://doi.org/10.1175/BAMS-D-11-00170.1>
- Chambon P, Mahfouf J-F, Audouin P, Birman C, Fourrié N et al (2022) Global observing system experiments within the météo-france 4D-Var data assimilation system. *Mon Weather Rev*. <https://doi.org/10.1175/MWR-D-22-0087.1> (10.1175/MWR-D-22-0087.1). (hal-03859189)
- Chapron B, Johnsen H, Garello R (2001) Wave and wind retrieval from SAR images of the ocean. *Annal Des Telecommun* 56:682–699
- Chapron B, Collard F, Ardhuin F (2005) Direct measurements of ocean surface velocity from space: interpretation and validation. *J Geophys Res* 110(C07008):1–17. <https://doi.org/10.1029/2004JC002809>
- Chawla I, Karthikeyan L, Mishra AK (2020) A review of remote sensing applications for water security: quantity, quality and extremes. *J Hydrol* 585:124826
- Chelton DB, Ries JC, Haines BJ, Fu L-L, Callahan P (2011) Satellite altimetry. In: Fu C (ed) *Satellite altimetry and Earth sciences*. Academic Press, Cambridge
- Chen W, Vandemark D, Mouche A, Chapron B, Li H, Foster RC (2020) An assessment of marine atmospheric boundary layer roll detection using Sentinel-1 SAR data. *Remote Sens Environ* 250:112031. <https://doi.org/10.1016/j.rse.2020.112031>
- Cheng Y, Xu Q, Gao L, Li X, Zou B, Liu T (2019) Sea state bias variability in satellite altimetry data. *Remote Sens* 11(10):1176
- Cipollini P, Benveniste J, Bouffard J, Emery W, Gommenginger C, Griffin D, Høyer J, Madsen K, Mercier F, Miller L (2010) The role of altimetry in coastal observing systems. *Proc OceanObs'09* 09:181–191
- Cipollini P, Benveniste J, Birol F, Fernandes MJ, Obligis E, Passaro M, Strub PT, Valladeau G, Vignudelli S, Wilkin J (2017) Satellite altimetry in coastal regions. In: *Satellite altimetry over oceans and land surfaces*, edited. CRC Press
- Collard F, Ardhuin F, Chapron B (2005) Extraction of coastal ocean wave fields from SAR images. *IEEE J Oceanic Eng* 30:526–533
- Collard F, Ardhuin F, Chapron B (2009) Monitoring and analysis of ocean swell fields from space: new methods for routine observations. *J Geophys Res*. <https://doi.org/10.1029/2008JC005215>
- Combout C, Mouche A, Knaff J, Yili Z, Yuan Z, Vinour L, Chapron B (2020) Extensive high-resolution synthetic aperture radar (SAR) data analysis of tropical cyclones: comparisons with SFMR flights and best-track. *Mon Weather Rev* 148(11):4545–4563. <https://doi.org/10.1175/MWR-D-20-0005.1>
- Cotton D, Lindgren G, Rychlik I, Olagnon M, Prevosto M, Nerzic R, Leenaars C, Brugghe P, Parmentier G (2000) Conveying metocean knowledge improvements on to shipping safety. Final Report European Commission under contract number ENV4-CT98–0751. <http://www.satoc.eu/sos/projects/Projects/Comkiss/reports/COMKISSFR.pdf>
- Cox R, Ardhuin F, Dias F, Autret R, Beisiegel N, Earlie CS et al (2020) Systematic review shows that work done by storm waves can be misinterpreted as tsunami-related because commonly used hydrodynamic equations are flawed. *Front Mar Sci*. <https://doi.org/10.3389/fmars.2020.00004>
- Cradden L, Kalogeri C, Barrios IM, Galanis G, Ingram D, Kallos G (2016) Multi-criteria site selection for offshore renewable energy platforms. *Renew Energy* 87:791–806
- D'Asaro EA (2014) Turbulence in the upper-ocean mixed layer. *Ann Rev Mar Sci* 6:101–115. <https://doi.org/10.1146/annurev-marine-010213-135138>
- Danilo C, Melgani F (2019) High-coverage satellite-based coastal bathymetry through a fusion of physical and learning methods. *Remote Sens* 11:376
- D'Asaro EA, Carlson DF, Chamecki M, Harcourt RR, Haus BK, Fox-Kemper B, Molemaker MJ, Poje AC, Yang D (2020) Advances in observing and understanding small-scale open ocean circulation during the Gulf of Mexico research initiative Era. *Front Mar Sci*. <https://doi.org/10.3389/fmars.2020.00349>
- Davidson MA, van Koningsveld M, de Kruif A, Rawson J, Holman R, Lamberti A, Medina R, Kroon A, Aarninkhof S (2007) The CoastView project: developing video-derived coastal state indicators in support of coastal zone management. *Coastal Eng* 54:463–475
- Davidson FJM, Allen A, Brasington GB, Breivik Ø, Daniel P, Kamachi M, Sato S, King B, Lefevre F, Sutton M, Kaneko H (2009) Applications of GODAE ocean current forecasts to search and rescue and ship routing. *Oceanography* 22(3):176–181. <https://doi.org/10.5670/oceanog.2009.76>
- Davidson MA, Steele ECC, Sauter A (2019) Operational forecasting of coastal resilience. *Coastal Sedim*. [https://doi.org/10.1142/9789811204487\\_0121](https://doi.org/10.1142/9789811204487_0121)
- de Kloe J, Stoffelen A, Verhoef A (2017) Improved use of scatterometer measurements by using stress-equivalent reference winds. *J Select Top Appl Earth Obs Remote Sens* 10(5):2340–2347. <https://doi.org/10.1109/JSTARS.2017.2685242>

- de Michele M, Raucoules D, Idier D, Smai F, Fomelis M (2021) Shallow bathymetry from multiple Sentinel 2 images via the joint estimation of wave celerity and wavelength. *Remote Sens* 13:2149. <https://doi.org/10.3390/rs13112149>
- De Las Heras MM, Burgers G, Janssen PAEM (1994) Variational wave data assimilation in a third-generation wave model. *J Atmos Oceanic Tech* 11(5):1350–1369. [https://doi.org/10.1175/1520-0426\(1994\)011%3c1350:VWDAIA%3e2.0.CO;2](https://doi.org/10.1175/1520-0426(1994)011%3c1350:VWDAIA%3e2.0.CO;2)
- Deng X, Featherstone W (2006) A coastal retracking system for satellite radar altimeter waveforms: application to ERS-2 around Australia. *J Geophys Res Oceans* 111(C6):32541
- Denny MW, Helmuth B, Leonard GH, Harley CDG, Hunt LJH, Nelson EK (2004) Quantifying scale in ecology: lessons from awave-swept shore. *Ecol Monogr* 74(3):513–532. <https://doi.org/10.1890/03-4043>
- Dewar WK, Flierl GR (1987) Some effects of the wind on rings. *J Phys Oceanogr* 17(10):1653–1667
- Dinard S, Fenoglio-Marc L, Becker M, Scharroo R, Fernandes MJ, Staneva J, Grayek E, Benveniste J (2021) A RIP-based SAR retracker and its application in North East Atlantic with Sentinel-3. *Adv Space Res* 68(2):892–929
- Dinardo S, Fenoglio-Marc L, Buchhaupt C, Becker M, Scharroo R, Fernandes MJ, Benveniste J (2018) Coastal sar and plrm altimetry in german bight and west baltic sea. *Adv Space Res* 62(6):1371–1404
- Dobrynin M, Murawski J, Baehr J, Ilyina T (2015) Detection and attribution of climate change signal in ocean wind waves. *J Clim* 28(4):1578–1591
- Dobson E, Monaldo F, Goldhirsh J, Wilkerson J (1987) Validation of Geosat altimeter-derived wind speeds and significant wave heights using buoy data. *J Geophys Res Oceans* 92(C10):10719–10731
- Dodet G, Piolle J-F, Quilfen Y, Abdalla S, Accensi M, Ardhuin F, Ash E, Bidlot J-R, Gommenginger C, Marechal C, Passaro M, Quartly G, Stopa J, Timmermans B, Young I, Cipollini P, Donlon C (2020) The sea state CCI dataset v1: towards a sea state climate data record based on satellite observations. *Earth Syst Sci Data* 12:1929–1951. <https://doi.org/10.5194/essd-12-1929-2020>
- Dodet G, Abdalla S, Alday M, Accensi M, Bidlot J-R, Ardhuin F (2022) Error characterization of significant wave heights in multi-decadal satellite altimeter product, model hindcast and in situ measurements, using triple collocation technique. *J Atmosph Oceanic Tech.* <https://doi.org/10.1175/JTECH-D-21-0179.1>
- Donelan MA, Pierson WJ Jr (1987) Radar scattering and equilibrium ranges in wind-generated waves with application to scatterometry. *J Geophys Res* 92(C5):4971–5029
- Donlon CJ, Cullen R, Giulicchi L, Vuilleumier P, Francis CR, Kuschnerus M, Simpson W, Bouridah A, Caleno M, Bertoni R (2021) The Copernicus Sentinel-6 mission: enhanced continuity of satellite sea level measurements from space. *Remote Sens Environ* 258:112395
- Drennan WM, Graber HC, Hauser D, Quentin C (2003) On the wave age dependence of wind stress over pure wind seas. *J Geophys Res* 108(C3):8062. <https://doi.org/10.1029/2000JC000715>
- Du Y, Vachon PW, Wolfe J (2002) Wind direction estimation from SAR images of the ocean using wavelet analysis. *Can J Remote Sens* 28(3):498–509
- Dukhovskoy DS, Morey SL (2011) Simulation of the Hurricane Dennis storm surge and considerations for vertical resolution. *Nat Hazards J* 58:511–540. <https://doi.org/10.1007/s11069-010-9684-5>
- Dullaart JCM, Muis S, Bloemendaal N et al (2020) Advancing global storm surge modeling using the new ERA5 climate reanalysis. *Clim Dyn* 54:1007–1021. <https://doi.org/10.1007/s00382-019-05044-0>
- Duncan JB, Marseille GJ, and Wijntan IL (2019) DOWA validation against ASCAT satellite winds. TNO report 2018 R11649, Petten, The Netherlands. <https://www.dutchcoffshorewindatlas.nl/binaries/dowa/documents/reports/2019/01/18/tno-report---dowa-validation-against-ascatsatellite-winds/TNO+2018+R11649+DOWA+validation+ASCAT.pdf>
- Dvorak V (1984) Tropical cyclone intensity analysis using satellite data. NOAA Technical Report NESDIS 11, NOAA. [https://satepsanone.nesdis.noaa.gov/pub/Publications/Tropical/Dvorak\\_1984.pdf](https://satepsanone.nesdis.noaa.gov/pub/Publications/Tropical/Dvorak_1984.pdf)
- Egido A, Dinardo S, Ray C (2021) The case for increasing the posting rate in delay/Doppler altimeters. *Adv Space Res* 68(2):930–936
- Elfouhaily TM, Chapron B, Katsaros K, Vandemark D (1997) A unified directional spectrum for long and short wind-driven waves. *J Geophys Res* 102:15781–15796. <https://doi.org/10.1029/97JC00467>
- Elhouhaily TM, Guérin C-A (2004) A critical survey of approximate scattering wave theories from random rough surfaces. *Waves Random Media.* <https://doi.org/10.1088/0959-7174/14/4/R01>
- Elyouncha A, Eriksson LEB, Johnsen H (2022) Direct comparison of sea surface velocity estimated from Sentinel-1 and TanDEM-X SAR data. *IEEE J Select Top Appl Earth Obs Remote Sens* 15:2425–2436. <https://doi.org/10.1109/JSTARS.2022.3158190>
- Engen G, Johnsen H (1995) SAR ocean wave inversion using image cross spectra. *IEEE Trans Geosci Remote Sens* 33(4):1047–1056

- Engen G, Johnsen H, Krogstad HE, Barstow SF (1994a) Directional wave spectra by inversion of ERS-1 synthetic aperture radar ocean imagery. *IEEE Trans Geosci Remote Sens* 32(2):340–352
- Engen G, Vachon PW, Johnsen H, Dobson FW (2000) Retrieval of ocean wave spectra and RAR MTF's from dual-polarization SAR data. *IEEE Trans Geosci Remote Sens* 38(1):391–403. <https://doi.org/10.1109/36.82393>
- Engen G, Johnsen H (2015) Sentinel-1 Doppler and ocean radial velocity algorithm definition. Norut report No. 19/2015, S1-TN-NRT-53–0658, version 1.4. ISBN: 978–82–7492–311–9
- Engen G (1997) Imaging ocean waves with synthetic aperture Radar. Phd thesis, University of Tromsø, NORUT IT
- English S, Prigent C, Johnson B, Yueh S, Dinnat E, Boutin J, Newman S, Angelova M, Meissner T, Kazumori M, Weng F, Supply A, Kilic L, Bettenhausen M, Stoffelen A, Accadia C (2020) Reference-quality emission and backscatter modeling for the ocean. *Bull Am Meteorol Soc* 101(10):E1593–E1601
- Entekhabi D, Njoku E, O'Neill P, Kellogg KH, Crow W, Edelstein WN, Entin J, Goodman S, Jackson T, Johnson J, Kimball J, Piepmeier J, Koster R, Martin N, McDonald K, Moghaddam M, Moran S, Reichle R, Shi J, van Zyl J (2010) The soil moisture active passive (SMAP) mission. *Proc IEEE* 98:704–716. <https://doi.org/10.1109/JPROC.2010.2043918>
- Ericson EA, Lyzenga DR, Walker DT (1999) Radar backscattering from Estationary breaking waves. *J Geophys Res* 104:29,679–29,695
- ESA (2019) Report for mission selection: SKIM, ESA-EOPSM-SKIM-RP-3550. European Space Agency, Noordwijk
- Escudier P, Couhert A, Mercier F, Mallet A, Thibaut P, Tran N, Amarouche L, Picard B, Carrere L, Dibarboure G, Ablain A, Richard J, Steunou N, Dubois P, Rio M-H, Dorandeu J (2017) Satellite radar altimetry. In: Stammer D, Cazenave A (eds) *Satellite altimetry over oceans and land surfaces*. CRC Press, Boca Raton
- Fenoglio-Marc L, Dinardo S, Scharroo R, Roland A SMD, Lucas B, Becker M, Benveniste J, Weiss R (2015) The German bight: a validation of CryoSat-2 altimeter data in SAR mode. *Adv Space Res* 55(11):2641–2656
- Figa-Saldaña J, Wilson JW, Attema E, Gelsthorpe R, Drinkwater MR, Stoffelen A (2002) The advanced scatterometer (ASCAT) on the meteorological operational (MetOp) platform: a follow on for European wind scatterometers. *Can J Remote Sens* 28(3):404–412. <https://doi.org/10.5589/m02-035>
- Fingas M, Brown CE (2018) A review of oil spill remote sensing. *Sensors* 18:91. <https://doi.org/10.3390/s18010091>
- Fois F (2015) Enhanced ocean scatterometry. PhD thesis, Delft University of Technology, Delft. <https://doi.org/10.4233/uuid:06d7f7ad-36a9-49fa-b7ae-ab9dfc072f9c>
- Fois F, Hoogeboom P, Le Chevalier F, Stoffelen A (2015) An analytical model for the description of the full-polarimetric sea surface Doppler signature. *J Geophys Res Oceans* 120(2):988–1015
- Foltz GR, Brandt P, Richter I, Rodríguez-Fonseca B, Hernandez F, Dengler M, Rodrigues RR, Schmidt JO, Yu L, Lefevre N, Da Cunha LC, McPhaden MJ, Araujo M, Karstensen J, Hahn J, Martín-Rey M, Patricola CM, Poli P, Zuidema P, Hummels R, Perez RC, Hatje V, Lübbecke JF, Polo I, Lumpkin R, Bourlès B, Asuquo FE, Lehodey P, Conchon A, Chang P, Dandin P, Schmid C, Sutton A, Giordani H, Xue Y, Illig S, Losada T, Grodsky SA, Gasparin F, Lee T, Mohino E, Nobre P, Wankinkhof R, Keenlyside N, Garçon V, Sánchez-Gómez E, Nnamchi HC, Drévillon M, Storto A, Remy E, Lazar A, Speich S, Goes M, Dorrington T, Johns WE, Moum JN, Robinson C, Perruche C, de Souza RB, Gaye AT, López-Parages J, Monerie P-A, Castellanos P, Benson NU, Hounkonnou MN, Duhá JT, Laxenaire R, Reul N (2019) The tropical Atlantic observing system. *Front Mar Sci* 6:206. <https://doi.org/10.3389/fmars.2019.00206>
- Fore AG, Yueh SH, Tang W, Stiles BW, Hayashi AK (2016) Combined active/passive retrievals of ocean vector wind and sea surface salinity with SMAP. *IEEE Trans Geosci Remote Sens* 54:7396–7404. <https://doi.org/10.1109/TGRS.2016.2601486>
- Fore AG, Yueh SH, Stiles BW, Tang W, Hayashi AK (2018) SMAP radiometer-only tropical cyclone intensity and size validation. *IEEE Geosci Remote Sens Lett* 15:1480–1484. <https://doi.org/10.1109/LGRS.2018.2849649>
- Foti G, Gommenginger C, Jales P, Unwin M, Shaw A, Robertson C, Roselló J (2015) Spaceborne GNSS reflectometry for ocean winds: First results from the UK TechDemoSat-1 mission. *Geophys Res Lett*. <https://doi.org/10.1002/2015GL064204>
- Foti G, Gommenginger C, Srokosz M (2017) First spaceborne GNSS-reflectometry observations of hurricanes from the UK TechDemoSat-1 Mission. *Geophys Res Lett* 44(24):12358–312366
- Fu L-L, Cazenave A (2001) *Satellite altimetry and Earth sciences- a handbook of techniques and applications*. Academic Press, Cambridge

- Fu L-L, Holt B (1982) Seasat views oceans and seas with synthetic aperture radar. Jet Propulsion Laboratory, Pasadena
- Gade M, Stoffelen A (2019) An introduction to microwave remote sensing of the Asian seas. In: Barale V, Gade M (eds) Remote sensing of the Asian seas. Springer, Cham
- Geernaert GL, Plant WJ (1990) Surface waves and fluxes. In: Geernaert GL, Plant WJ (eds) Volume II—remote sensing. Kluwer Academic Publishers, Cham
- Gerling TW (1986) Structure of the surface wind field from the Seasat SAR. *J Geophys Res* 91:2308–2320
- Giesen R, Clementi E, Bajo M, Federico I, Stoffelen A, Santoleri R (2021) The november 2019 record high water levels in Venice, Italy, Copernicus marine service ocean state report issue 5. *J Oper Oceanogr*. <https://doi.org/10.1080/1755876X.2021.1946240>
- Gommenginger CP, Srokosz MA, Challenor PG, Cotton PD (2002) Development and validation of altimeter wind speed algorithms using an extended collocated buoy/Topex dataset. *IEEE Trans Geosci Remote Sens* 40(2):251–260
- Gommenginger CP, Srokosz MA, Wolf J, Janssen PAEM (2003) An investigation of altimeter sea state bias theories. *J Geophys Res* 108(C1):3011. <https://doi.org/10.1029/2001JC001174>
- Gommenginger CP, Martin-Puig C, Dinardo S, Cotton D, Srokosz M, Benveniste J (2011) Improved altimetric accuracy of SAR altimeters over ocean: Observational evidence from Cryosat-2 SAR and Jason. Ocean Surface Topography Science Team, San Diego
- Gommenginger CP, Chapron B, Hogg A, Buckingham C, Fox-Kemper B, Eriksson L, Soulat F, Rio M-H, Ubelmann C, Ocampo-Torres F, Buongiorno-Nardelli B, Griffin D, Lopez-Dekker P, Knudsen P, Andersen O, Stenseng L, Stapleton N, Perrie W, Violante-Carvalho N, Schulz-Stellenfleth J, Woolf D, Isern-Fontanet J, Arduini F, Klein P, Mouche A, Pascual A, Capet X, Hauser D, Stoffelen A, Morrow R, Aouf L, Breivik O, Fu L-L, Johannessen J, Aksenov Y, Brichenno LM, Hirschi J, Martin ACH, Martin AP, Nurser G, Polton J, Wolf J, Johnsen H, Soloviev A, Jacobs G, Collard F, Groom S, Kudryavstev V, Wilkin J, Navarro V, Babanin A, Martin M, Siddorn J, Sauter A, Rippeth T, Emery B, Maximenko N, Romeiser R, Graber H, Alvera-Azcarate A, Hughes C, Vandemark D, Naveira-Gabarrato A, Gemmrich J, Mahadevan A, Marquez J, Munro Y, Doody S, Burbidge G (2019) SEASTAR: a mission to study ocean submesoscale dynamics and small-scale atmosphere-ocean processes in coastal, shelf and polar seas OceanObs'2019. *Front Mar Sci* 6(457):1. <https://doi.org/10.3389/fmars.2019.0045>
- Gommenginger CP, Martin-Puig C, Amarouche L, Raney RK (2013) Jason-CS SAR mode error budget study: review of state of knowledge of SAR altimetry over ocean. EUM/RSP/REP/14/749304, version 2.2. [http://eprints.soton.ac.uk/366765/1/SARAltimetry\\_Review\\_JasonCS\\_EUMETSAT.pdf](http://eprints.soton.ac.uk/366765/1/SARAltimetry_Review_JasonCS_EUMETSAT.pdf)
- Gourrion J, Vandemark D, Bailey S, Chapron B, Gommenginger CP, Challenor PG, Srokosz MA (2002) A two-parameter wind speed algorithm for Ku-band altimeters. *J Atmos Oceanic Technol* 19:2030–2048. <https://doi.org/10.1175/1520-0426>
- Greenslade DJM (2001) The assimilation of ERS-2 significant wave height data in the Australian region. *J Mar Syst* 28(1–2):141–160. [https://doi.org/10.1016/S0924-7963\(01\)00005-7](https://doi.org/10.1016/S0924-7963(01)00005-7)
- Guérou A, Meyssignac B, Prandi P, Ablain M, Ribes A, Bignalet-Cazalet F (2022) Current observed global mean sea level rise and acceleration estimated from satellite altimetry and the associated uncertainty. *Egusphere*. <https://doi.org/10.5194/egusphere-2022-330>
- Hajduch G et al. (2021) Sentinel-1A and 1B annual performance report 2020, MPC-0504. <https://elib.dlr.de/145956/1/Sentinel-1-Annual-Performance-Report-2020.pdf>
- Hammond ML, Foti G, Gommenginger C, Srokosz M (2020) Temporal variability of GNSS-Reflectometry ocean wind speed retrieval performance during the UK TechDemoSat-1 mission. *Remote Sens Environ* 242:111744
- Hansen J, Sato M, Kharecha P, von Schuckmann K (2011) Earth's energy imbalance and implications. *Atmos Chem Phys* 11:13421–13449. <https://doi.org/10.5194/acp-11-13421-2011>
- Hanson JL, Phillips OM (2001) Automated analysis of ocean surface directional wave spectra. *J Atmos Oceanic Tech* 18(2):277–293
- Haoyu J (2020) Evaluation of altimeter undersampling in estimating global wind and wave climate using virtual observation. *Remote Sens Environ* 245:111840. <https://doi.org/10.1016/j.rse.2020.111840>
- Haoyu J, Mironov A, Lin R, Babanin A, Lin Mu (2021) Validation of wave spectral partitions from SWIM instrument on-board CFOSAT against In-situ Data. *IEEE Trans Geosci Remote Sens*. <https://doi.org/10.1109/TGRS.2021.3110952>
- Hasselmann K, Hasselmann S (1991) On the nonlinear mapping of an ocean wave spectrum into a synthetic aperture radar image spectrum and its inversion. *J Geophys Res* 96(C6):10713–10729
- Hasselmann S, Brüning C, Hasselmann K, Heimbach P (1996) An improved algorithm for the retrieval of ocean wave spectra from SAR image spectra. *J Geophys Res* 101:16615–16629



- Hasselmann S, Lionello P, Hasselmann K (1997) An optimal interpolation scheme for the assimilation of spectral data. *J Geophys Res* 102:15823–15836
- Hauser D, Caudal G, Rijckenberg G-J, Vidal-Madjar D, Laurent G, Lancelin P (1992) RESSAC: A new airborne FM/CW radar ocean wave spectrometer. *IEEE Trans Geosci Remote Sens* 30(5):981–995
- Hauser D, Soussi E, Thouvenot E, Rey L (2001) SWIMSAT: A real aperture radar to measure directional spectra of ocean waves from space, Main characteristics and performance simulation. *J Atmos Oceanic Tech* 18(3):421–437
- Hauser D, Tison C, Amiot T, Delaye L, Corcoral N, Castellan P (2017) SWIM: The first spaceborne wave scatterometer. *IEEE Trans Geosci Remote Sens* 55(5):3000–3014. <https://doi.org/10.1109/TGRS.2017.2658672>
- Hauser D, Tourain C, Hermozo L, Alraddawi D, Aouf L, Chapron B, Dalphiné A, Delaye L, Gressani V, Grouazel A, Guitton G, Husson R, Mironov A, Mouche A, Ollivier A, Oruba L, Piras F, Rodriguez Suquet R, Schippers P, Tison C (2021) New observations from the SWIM radar on board CFOSAT: instrument validation and ocean wave measurement assessment. *IEEE Trans Geosci Remote Sens* 59(1):5–26. <https://doi.org/10.1109/TGRS.2020.2994372>
- Hayne G (1980) Radar altimeter mean return waveforms from near-normal-incidence ocean surface scattering. *IEEE Trans Antennas Propag* 28(5):687–692
- Hersbach H (1998) Application of the adjoint of the WAM model to inverse wave modeling. *J Geophys Res* 103(C5):10469–10487. <https://doi.org/10.1029/97JC03554>
- Hersbach H, de Rosnay P, Bell B, Schepers D, Simmons A, Soci C et al (2018) Operational global reanalysis: progress, future directions and synergies with NWP. Technical Report European Centre for Medium Range Weatherforecasting, UK
- Hollinger JP (1991) DMSP special sensor microwave/imager calibration/validation. Final Report Space Sensing Branch Naval Research Laboratory, Washington
- Holman R, Plant N, Holland T (2013) cBathy: a robust algorithm for estimating nearshore bathymetry. *J. Geophys Res Oceans* 118(5):2592–2609
- Hwang PA, Reul N, Meissner T, Yueh SH (2019a) Ocean surface foam and microwave emission: dependence on frequency and incidence angle. *IEEE Trans Geosci Remote Sens* 57(10):8223–8234
- Hwang PA, Reul N, Meissner T, Yueh SH (2019b) Whitecap and wind stress observations by microwave radiometers: global coverage and extreme conditions. *J Phys Oceanogr* 49(9):2291–2307
- Irisov VG (2000) Azimuthal variations of the microwave radiation from a slightly non-Gaussian sea surface. *Radio Sci.* <https://doi.org/10.1029/1999RS900104.35.1.65-82>
- Isaksen L, Stoffelen A (2000) ERS scatterometer wind data impact on ECMWF ’s tropical cyclone forecasts. *IEEE Trans Geosci Remote Sens* 38(4):1885–1892. <https://doi.org/10.1109/36.851771>
- Ishimaru A (1978) Wave propagation and scattering in random media. IEEE Press Oxford University Press, Oxford
- Jackson FC (1981) An analysis of short pulse and dual frequency radar techniques for measuring ocean wave spectra from satellites. *Radio Sci* 16(6):1385–1400. <https://doi.org/10.1029/RS016i006p01385>
- Jackson FC, Walton WT, Baker PL (1985a) Aircraft and satellite measurement of ocean wave directional spectra using scanning-beam microwave radars. *J Geophys Res* 90(C1):987
- Jackson FC, Walton WT, Peng CY (1985b) A comparison of in situ and airborne radar observations of ocean wave directionality. *J Geophys Res* 90(C1):1005
- Jackson CR, Ruff TW, Knaff JA, Mouche A, Sampson CR (2021) Chasing cyclones from space. *Eos.* <https://doi.org/10.1029/2021EO159148>
- Janssen PAEM, Bidlot J-R (2018) Progress in Operational wave forecasting, *Procedia IUTAM* 26, 14–29. IUTAM Symposium on Wind Waves, 4–8 September 2017, London, UK, <https://doi.org/10.1016/j.piutam.2018.03.003>
- Janssen PM, Bidlot J-R (2009) On the extension of the freak wave warning system and its verification. Tech Memorandum. <https://doi.org/10.21957/uf1sybog>
- Johannessen JA, Chapron B, Collard F, Kudryavtsev V, Mouche A, Akimov D, Dagestad K-F (2008) Direct ocean surface velocity measurements from space: improved quantitative interpretation of Envisat ASAR observations. *Geophys Res Lett* 35:L22608. <https://doi.org/10.1029/2008GL035709>
- Johnsen H (2005) Envisat ASAR wave mode product description and reconstruction procedure. Report for ESA contract 17376/03/I-OL. <https://earth.esa.int/eogateway/documents/20142/37627/Envisat-ASAR-Wave-Mode-Product-Description-and-Reconstruction-Procedure.pdf>
- Johnson JT, Zhang M (1999) Theoretical study of the small slope approximation for ocean polarimetric thermal emission. *IEEE Trans Geosci Remote Sens* 37(5):2305–2316



- Johnsen et al. (2022), Sentinel-1 ocean swell wave spectra (OSW) algorithm definition, ESA document, S1-TN-NRT-52–7450, MPC-0469. [https://sentinel.esa.int/documents/247904/0/S-1\\_L2\\_OSW\\_Detailed\\_Algorithm\\_Definition.pdf/46372081-4a3c-441b-91c9-eee5aa475bbc](https://sentinel.esa.int/documents/247904/0/S-1_L2_OSW_Detailed_Algorithm_Definition.pdf/46372081-4a3c-441b-91c9-eee5aa475bbc)
- Jones CE, Dagestad K-F, Breivik Ø, Holt B, Røhrs J, Christensen KH, Espeseth M, Brekke C, Skrunes S (2016) Measurement and modeling of oil slick transport. *J Geophys Res Oceans* 121:7759–7775
- Kaldellis JK, Kapsali M (2013) Shifting towards offshore wind energy—recent activity and future development. *Energy Policy* 53:136–148
- Kamphuis JW (2020) Introduction to coastal engineering and management, 3rd edn. World Scientific, Singapore
- Kanjir U, Oštir GHC (2018) Vessel detection and classification from spaceborne optical images: a literature survey. *Remote Sens Environ* 207:1–26
- Kerr YH et al (2010) The SMOS mission: new tool for monitoring key elements of the global water cycle. *Proc IEEE* 98:666–687. <https://doi.org/10.1109/JPROC.2010.2043032>
- Khan N, Kalair A, Abas N, Haider A (2017) Review of ocean tidal, wave and thermal energy technologies. *Renew Sustain Energy Rev* 72:590–604
- King GP, Portabella M, Wenming L, Stoffelen A (2022) Correlating extremes in wind divergence with extremes in rain over the tropical atlantic. *Remote Sens* 14(5):1147. <https://doi.org/10.3390/rs14051147>
- Klein P, Lapeyre G, Siegelman L, Qiu B, Fu L-L, Torres H, Su Z, Menemenlis D, Le Gentil S (2019) Ocean-scale interactions from space. *Earth Space Sci* 6(5):795–817
- Klotz BW, Uhlhorn EW (2014) Improved stepped frequency microwave radiometer tropical cyclone surface winds in heavy precipitation. *J Atmos Oceanic Technol* 31(11):2392–2408. <https://doi.org/10.1175/JTECH-D-14-00028.1>
- Klotz BW, Neuenschwander A, Magruder LA (2020) High-resolution ocean wave and wind characteristics determined by the ICESat-2 land surface algorithm. *Geophys Res Lett* 47:e2019GL085907. <https://doi.org/10.1029/2019GL085907>
- Knaff JA, Sampson CR, Kucas M, Slocum CJ, Brennan MJ, Meissner T, Ricciardulli L, Mouche A, Reul N, Morris M, Chirokova G, Caroff P (2021) A practical guide to estimating tropical cyclone surface winds: history, current status, emerging technologies, and a look to the future. *Trop Cyclone Res Rev* 10(3):135–150. <https://doi.org/10.1016/j.tcr.2021.09.002>
- Koch W (2004) Directional analysis of sar images aiming at wind direction. *IEEE Trans Geosci Remote Sens* 42(4):702–710
- Krogstad HE (1992) A simple derivation of Hasselmann's nonlinear ocean-to-synthetic aperture radar transform. *J Geophys Res* 77(C2):2421–2425
- Kudryavtsev V, Hauser D, Caudal G, Chapron B (2003) A semiempirical model of the normalized radar cross-section of the sea surface 1 Background model. *J Geophys Res*. <https://doi.org/10.1029/2001JC001003>
- Kudryavtsev V, Yurovskaya M, Chapron B, Collard F, Donlon C (2017a) Sun glitter imagery of ocean surface waves. Part 1: directional spectrum retrieval and validation. *J Geophys Res Oceans* 122(2):1369–1383. <https://doi.org/10.1002/2016JC012425>
- Kudryavtsev V, Yurovskaya M, Chapron B, Collard F, Donlon C (2017b) Sun glitter imagery of surface waves. Part 2: waves transformation on ocean currents. *J Geophys Res Oceans* 122(2):1384–1399. <https://doi.org/10.1002/2016JC012426>
- Kunkee DB, Gasiewski AJ (1997) Simulation of passive microwave wind direction signatures over the ocean using an asymmetric-wave geometrical optics model. *Radio Sci* 32(1):59–78. <https://doi.org/10.1029/96RS02434>
- Lahtinen J, Pihlflyckt J, Mononen I, Tauriainen SJ, Kemppinen M, Hallikainen MT (2003) Fully polarimetric microwave radiometer for remote sensing. *IEEE Trans Geosci Remote Sens* 41(8):1869–1878. <https://doi.org/10.1109/TGRS.2003.813847>
- Laignel B, Vignudelli S, Almar R, Becker M, Bentamy A, Benveniste J, Birol F, Frappart F, Idier D, Salameh E, Passaro M, Menende M, Simard M, Turki EI, Verpoorter C (2023) Observation of the coastal areas, estuaries and deltas from space. *Surv Geophys* 44, in press
- Lalouaux P, Thépaut J-N, Dee D (2016) Impact of scatterometer surface wind data in the ECMWF coupled assimilation system. *Mon Weather Rev* 144(3):1203–1217. <https://doi.org/10.1175/MWR-D-15-0084.1>
- Lambin J, Morrow R, Fu L-L, Willis JK, Bonekamp H, Lillibridge J, Perbos J, Zaouche G, Vaze P, Ban-noura W (2010) The OSTM/jason-2 mission. *Mar Geodesy* 33(S1):4–25
- Lapeyre G, Klein P (2006) Impact of the small-scale elongated filaments on the oceanic vertical pump. *J Mar Res* 64(6):835–851

- Laursen B, Skou N (2001) Wind direction over the ocean determined by an airborne, imaging, polarimetric radiometer system. *IEEE Trans Geosci Remote Sens* 39(7):1547–1555. <https://doi.org/10.1109/36.934086>
- Lavender S, Lavender A (2016) Practical handbook of remote sensing. CRC Press, Florida
- Laxon SW, Giles KA, Ridout AL, Wingham DJ, Willatt R, Cullen R, Kwok R, Schweiger A, Zhang J, Haas C (2013) CryoSat-2 estimates of Arctic sea-ice thickness and volume. *Geophys Res Lett* 40(4):732–737
- Le Traon P-Y, Antoine D, Bentamy A, Bonekamp H, Breivik LA, Chapron B et al (2015) Use of satellite observations for operational oceanography: recent achievements and future prospects. *J Oper Oceanogr* 8:s12–s27
- Le Traon P-Y, Reppucci A et al (2019) From observation to information and users: the Copernicus Marine Service perspective. *Front Mar Sci* 6:234. <https://doi.org/10.3389/fmars.2019.00234>
- Lévy M, Ferrari R, Franks PJ, Martin AP, Rivière P (2012) Bringing physics to life at the submesoscale. *Geophys Res Lett* 39(14):12544. <https://doi.org/10.1029/2012GL052756>
- Li XM, Lehner S, Bruns T (2011) Ocean wave integral parameter measurements using Envisat ASAR wave mode data. *IEEE Trans Geosci Remote Sens* 49:155–174
- Li H, Chapron B, Mouche AA, Stopa JE. (2019) A new ocean sar cross-spectral parameter: definition and directional property using the global sentinel-1 measurements. *J Geophys Res Oceans* 124(3):1566–1577
- Lillibridge J, Scharroo R, Abdalla S, Vandemark D (2014) One-and two-dimensional wind speed models for Ka-band altimetry. *J Atmos Oceanic Tech* 31(3):630–638
- Lin W, Portabella M, Stoffelen A, Vogelzang J, Verhoef A (2015) ASCAT wind quality under high sub-cell wind variability conditions. *J Geophys Res Oceans* 120:5804–5819. <https://doi.org/10.1002/2015JC010861>
- Lin W et al (2019) A perspective on the performance of the CFOSAT rotating fan-beam scatterometer. *IEEE Trans Geosci Remote Sens* 57(2):627–639. <https://doi.org/10.1109/TGRS.2018.2858852>
- Lionello P, Günther H, Janssen PAEM (1992) Assimilation of altimeter data in a global third-generation wave model. *J Geophys Res* 97(C9):14453–14474. <https://doi.org/10.1029/92JC01055>
- Liu AK, Mollo-Christensen E (1988) Wave propagation in a solid ice pack. *J Phys Oceanogr* 18:1702–1712
- Long DG (2017) Comparison of seawinds backscatter imaging algorithms. *IEEE J Select Top Appl Earth Obs Remote Sens* 10(5):2214–2231. <https://doi.org/10.1109/JSTARS.2016.2626966>
- Longépé N, Mouche AA, Ferro-Famil L, Husson R (2021) Co-cross-polarization coherence over the sea surface from Sentinel-1 SAR data: perspectives for mission calibration and wind field retrieval. *IEEE Trans Geosci Remote Sens* 60:1–16. <https://doi.org/10.1109/TGRS.2021.3055979>
- López-Dekker P, Rott H, Prats-Iraola P, Chapron B, Scipal K, Witte ED (2019) Harmony: an earth explorer 10 mission candidate to observe land, ice, and ocean surface dynamics. *Proc Int Geosci Remote Sens Symp.* <https://doi.org/10.1109/IGARSS.2019.8897983>
- Lorenc A, Bowler N, Clayton A, Pring S, Fairbairn D (2015) Comparison of hybrid-4DVar and Hybrid-4DVar data assimilation methods for global NWP. *Monthly Weather Rev Spec Collect Sixth WMO Data Assimil Symp.* <https://doi.org/10.1175/MWR-D-14-00195.1>
- Luijendijk A, Hagenaaers G, Ranasinghe R, Baart F, Donchyts G, Aarninkhof S (2018) The state of the world's beaches. *Sci Rep* 8(1):6641. <https://doi.org/10.1038/s41598-018-24630-6>
- Marechal G, Arduin F (2021) Surface currents and significant wave height gradients: matching numerical models and high-resolution altimeter wave heights in the Agulhas current region. *J Geophys Res Oceans* 126:e2020JC016564. <https://doi.org/10.1029/2020JC016564>
- Marié L, Collard F, Noguier F, Pineau-Guillou L, Hauser D, Boy F, Arduin F (2020) Measuring ocean surface velocities with the KuROS airborne near-nadir Doppler radar: a multi-scale analysis in preparation of the skim mission. *Ocean Sci* 16:1399–1429. <https://doi.org/10.5194/os-16-1399-2020>
- Martin S (2014) An introduction to ocean remote sensing, 2nd edn. Cambridge University Press, Cambridge
- Martínez ML, Intralawan A, Vázquez G, Pérez-Maqueo O, Sutton P, Landgrave R (2007) The coasts of our world: ecological, economic and social importance. *Ecol Econ* 63:254–272. <https://doi.org/10.1016/j.ecolecon.2006.10.022>
- Mastenbroek C, de Valk CF (2000) A semi-parametric algorithm to retrieve ocean wave spectra from synthetic aperture radar. *J Geophys Res* 105:3497–3516. <https://doi.org/10.1029/1999JC900282>
- Mastenbroek C (1996) Wind-wave interaction. In: Doctoral thesis civil engineering and geosciences, Technical Un. Delft, The Netherlands, <http://resolver.tudelft.nl/uuid:b91093af-ccae-4d85-894e-af128cc9f59c>

- Masters D, Nerem R, Choe C, Leuliette E, Beckley B, White N, Ablain M (2012) Comparison of global mean sea level time series from TOPEX/Poseidon, Jason-1, and Jason-2. *Mar Geodesy* 35(sup1):20–41
- McCarthy MJ, Colna KE, El-Mezayen MM et al (2017) Satellite remote sensing for coastal management: a review of successful applications. *Environ Manage* 60(323):339. <https://doi.org/10.1007/s00267-017-0880-x>
- McGranahan G, Balk D, Anderson B (2007) The rising tide: assessing the risks of climate change and human settlements in low elevation coastal zones. *Environ Urban* 19:17–37. <https://doi.org/10.1177/0956247807076960>
- Medina-Lopez E, McMillan D, Lazic J, Hart E, Zen S, Angeloudis A, Bannon E, Browell J, Dorling S, Dorell RM, Forster R, Old C, Payne GS, Porter G, Rabaneda AS, Sellar B, Tapoglou E, Trifonova N, Woodhouse IH, Zampollo A (2021) Satellite data for the offshore renewable energy sector: synergies and innovation opportunities. *Remote Sens Environ*. <https://doi.org/10.1016/j.rse.2021.112588>
- Meissner T, Wentz F (2009) Wind vector retrievals under rain with passive satellite microwave radiometers. *IEEE Trans Geosci Remote Sens* 47:3065–3083
- Meissner T, Wentz FJ (2012) The emissivity of the ocean surface between 6–90 GHz over a large range of wind speeds and earth incidence angles. *IEEE Trans Geosci Remote Sens* 50(8):3004–3026
- Meissner T, Wentz F, Ricciardulli L (2014) The emission and scattering of L-band microwave radiation from rough ocean surfaces and wind speed measurements from the Aquarius sensor. *J Geophys Res Oceans* 119:6499–6522. <https://doi.org/10.1002/2014JC009837>
- Meissner T, Ricciardulli L, Wentz FJ (2017) Capability of the SMAP mission to measure ocean surface winds in storms. *Bull Amer Meteor Soc* 98:1660–1677. <https://doi.org/10.1175/BAMS-D-16-0052.1>
- Meissner T, Ricciardulli L, Manaster A (2021) Tropical cyclone wind speeds from WindSat, AMSR and SMAP: Algorithm development and testing. *Remote Sens* 13:1641. <https://doi.org/10.3390/rs13091641>
- Melet A, Teatini P, Le Cozannet G et al (2020) Earth observations for monitoring marine coastal hazards and their drivers. *Surv Geophys* 41:1489–1534. <https://doi.org/10.1007/s10712-020-09594-5>
- Meucci A, Young IR, Aarnes OJ, Breivik O (2019) Comparison of wind speed and wave height trends from twentieth-century models and satellite altimeters. *J Clim* 33(2):611–624. <https://doi.org/10.1175/JCLI-D-19-0540.1>
- Mile M, Randriamampianina R, Marseille G-J, Stoffelen A (2021) Supermodding—a special footprint operator for mesoscale data assimilation using scatterometer winds. *Q J R Meteorol Soc* 147:1382–1402. <https://doi.org/10.1002/qj.3979>
- Misra T, Chakraborty P, Lad C, Gupta P, Rao J, Upadhyay G, Kumar S, Kumar B, Gangele S, Sinha S, Tolani H, Vithani HV, Raman B, Rao C, Dave D, Jyoti R, Desai N (2019) SCATSAT-1 scatterometer: an improved successor of OSCAT. *Curr Sci* 117:941–949. <https://doi.org/10.18520/cs/v117/i6/941-949>
- Moiseev A, Johnsen H, Wergeland HM, Johannessen JA (2020a) Evaluation of radial ocean surface currents derived from Sentinel-1 IW Doppler shift using coastal radar and lagrangian surface drifter observations. *J Geophys Res Oceans* 125:e2019JC015743. <https://doi.org/10.1029/2019JC015743>
- Moiseev A, Johnsen H, Johannessen JA, Collard F, Guitton G (2020b) On removal of sea state contribution to Sentinel-1 Doppler shift for retrieving reliable ocean surface current. *J Geophys Res Oceans* 125:e2020JC016288. <https://doi.org/10.1029/2020JC016288>
- Moiseev A, Johannessen JA, Johnsen H (2022) Towards retrieving reliable ocean surface currents in the coastal zone from the Sentinel-1 Doppler shift observations. *J Geophys Res Oceans* 127:e2021JC018201. <https://doi.org/10.1029/2021JC018201>
- Monahan E, O'Muircheartaigh IG (1980) Optimal power-law description of oceanic whitecap coverage dependence on wind speed. *J Phys Oceanogr* 10:2094–2099
- Moreau T, Tran N, Aublanc J, Tison C, Le Gac S, Boy F (2018) Impact of long ocean waves on wave height retrieval from SAR altimetry data. *Adv Space Res* 62(6):1434–1444
- Moreau T, Cadier E, Boy F, Aublanc J, Rieu P, Raynal M, Labroue S, Thibaut P, Dibarboure G, Picot N (2021) High-performance altimeter Doppler processing for measuring sea level height under varying sea state conditions. *Adv Space Res* 67(6):1870–1886
- Mori N, Onorato M, Janssen PAEM (2011) On the estimation of the kurtosis in directional sea states for freak wave forecasting. *J Phys Oceanogr* 41:1484–1497. <https://doi.org/10.1175/2011JPO4542.1>
- Morrow R, Fu L-L, Arduin F, Benkiran M, Chapron B, Cosme E, d'Ovidio F, Farrar JT, Gille ST, Lapeyre G (2019) Global observations of fine-scale ocean surface topography with the surface water and ocean topography (SWOT) mission. *Front Mar Sci* 6:232
- Morrow R, Fu L-L, Rio M-H, Ray R, Prandi P, Le Traon P-Y, Benveniste J (2023) Ocean circulation from space. <https://doi.org/10.1007/s10712-023-09778-9>

- Mouche AA, Chapron B, Reul N, Collard F (2008) Predicted Doppler shifts induced by ocean surface wave displacements using asymptotic electromagnetic wave scattering theories. *Waves Random Complex Med* 18(1):185–196. <https://doi.org/10.1080/17455030701564644>
- Mouche AA, Collard F, Chapron B, Dagestad KF, Guitton G, Johannessen JA, Hansen MW (2012) On the use of Doppler shift for sea surface wind retrieval from SAR. *IEEE Trans Geosci Remote Sens* 50(7):2901–2909. <https://doi.org/10.1109/TGRS.2011.2174998>
- Mouche AA, Chapron B, Zhang B, Husson R (2017) Combined co- and cross- polarized SAR measurements under extreme wind conditions. *IEEE Trans Geosci Remote Sens* 55(12):6746–6755. <https://doi.org/10.1109/TGRS.2017.2732508>
- Mouche AA, Chapron B, Knaff J, Zhao Y, Zhang B, Combet C (2019) Co- and Cross- polarized SAR measurements for high-resolution description of major hurricane wind-structures: application to Irma category-5 Hurricane. *J Geophys Res Oceans* 124:3905–3922. <https://doi.org/10.1029/2019JC015056>
- Mulet S, Rio M-H, Etienne H, Artana C, Cancet M, Dibarboure G, Feng H, Husson R, Picot N, Provost C, Strub PT (2021) The new CNES-CLS18 global mean dynamic topography. *Ocean Sci* 17:789–808. <https://doi.org/10.5194/os-17-789-2021,2021>
- Najar MA, Benshila R, Bennioui YE, Thoumyre G, Almar R, Bergsma EWJ, Delvit J-M, Wilson DG (2022) Estimation from Sentinel-2 satellite imagery: comparing deep learning and physics-based approaches. *Remote Sens* 14:1196. <https://doi.org/10.3390/rs14051196>
- Naylor R, Burke M (2005) Aquaculture and ocean resources: raising tigers of the sea. *Annu Rev Environ Resour* 30:185–218. <https://doi.org/10.1146/annurev.energy.30.081804.121034>
- Neumann B, Vafeidis AT, Zimmermann J, Nicholls RJ (2015) Future coastal population growth and exposure to sea-level rise and coastal flooding—a global assessment. *PLoS ONE* 10(3):e0118571. <https://doi.org/10.1371/journal.pone.0118571>
- Njoku EG, Swanson L (1983) Global measurements of sea surface temperature, wind speed and atmospheric water content from satellite microwave radiometry. *Monthly Weather Rev* 111(10):1997
- Noh Y, Min HS, Raasch A (2004) Large eddy simulation of the ocean mixed layer: the effects of wave breaking and Langmuir circulation. *J Phys Oceanogr* 34:720–733
- Norberg W, Conaway J, Ross DB, Wilheit T (1971) Measurements of microwave emission from a foam-covered, wind-driven sea. *J Atmos Sci* 28(3):429–435. [https://doi.org/10.1175/1520-0469\(1971\)028%3c0429:MOMEFA%3e2.0.CO;2](https://doi.org/10.1175/1520-0469(1971)028%3c0429:MOMEFA%3e2.0.CO;2)
- Nouguier F, Chapron B, Collard F, Mouche AA, Rascle N, Ardhuin F, Wu X (2018) Sea surface kinematics from near-nadir radar measurements. *IEEE Trans Geosci Remote Sens*. <https://doi.org/10.1109/tgrs.2018.2833200>
- O'Neill LW (2012) Wind speed and stability effects on coupling between surface wind stress and SST observed from buoys and satellite. *J Clim* 25(5):1544–1569
- OECD (2016) The ocean economy in 2030. OECD Publishing, Paris
- ORSIG (2018) Metocean procedures guide for offshore renewables. *Inst Mar Sci Technol Tech Rep*. <https://www.imarest.org/reports/650-metocean-procedures-guide>
- Parfitt R, Czaja A, Minobe S, Kuwano-Yoshida A (2016) The atmospheric frontal response to SST perturbations in the Gulf stream region. *Geophys Res Lett* 43:2299–2306. <https://doi.org/10.1002/2016GL067723>
- Passaro M, Fenoglio-Marc L, Cipollini P (2014) Validation of significant wave height from improved satellite altimetry in the German Bight. *IEEE Trans Geosci Remote Sens* 53(4):2146–2156
- Pedersen IF, Engen G, Johnsen H (2005) Polarization dependency in sea surface frequency and its application to Envisat Alt-Pol data. *Proc Envisat ERS Symp* 572:41.1
- Pereira P, Baptista P, Cunha T, Silva PA, Romão S, Lafon V (2019) Estimation of the nearshore bathymetry from high temporal resolution Sentinel-1A C-band SAR data—a case study. *Remote Sens Environ* 223:166–178
- Phalippou L, Enjorlas V (2007) Re-tracking of SAR altimeter ocean power-waveforms and related accuracies of the retrieved sea surface height, significant wave height and wind speed. *Proc 2007 IEEE Int Geosci Remote Sens Symp*. <https://doi.org/10.1109/IGARSS.2007.4423608>
- Phillips OM (1988) Radar returns from the sea surface—Bragg scattering and breaking waves. *J Phys Oceanogr* 18:1063–1074
- Piepmeyer JR, Gasiewski AJ (2001) High-resolution passive polarimetric microwave mapping of ocean surface wind vector fields. *IEEE Trans Geosci Remote Sens* 39(3):606–622. <https://doi.org/10.1109/36.911118>
- Plant WJ (1990) Bragg scattering of electromagnetic waves from the air/sea interface. In: Geernaert GL, Plant WJ (eds) *Surface waves and fluxes, remote sensing*. Kluwer Academic Publishers, Cham

- Pleskachevsky A, Rosenthal W, Lehner S (2016) Meteo-marine parameters for highly variable environment in coastal regions from satellite radar images. *J Photogr Remote Sens* 119:464–484. <https://doi.org/10.1016/j.isprsjprs.2016.02.001>
- Pleskachevsky A, Jacobsen S, Tings B, Schwarz E (2019) Estimation of sea state from Sentinel-1 synthetic aperture radar imagery for maritime situation awareness. *Int J Remote Sens*. <https://doi.org/10.1080/01431161.2018.1558377>
- Polverari F, Portabella M, Lin W, Sapp JW, Stoffelen A, Jelenak Z, Chang PS (2021) On high and extreme wind calibration using ASCAT. *IEEE Trans Geosci Remote Sens*. <https://doi.org/10.1109/TGRS.2021.3079898>
- Polverari F, Sapp JW, Portabella M, Stoffelen A, Jelenak Z, Chang PS (2022) On dropsonde surface-adjusted winds and their use for the stepped frequency microwave radiometer wind speed calibration. *IEEE Trans Geosci Remote Sens*. <https://doi.org/10.1109/TGRS.2022.3189310>
- Portabella M, Stoffelen A, Johannessen JA (2002) Toward an optimal inversion method for synthetic aperture radar wind retrieval. *J Geophys Res: Oceans* 107(C8):1–1. <https://doi.org/10.1029/2001JC000925>
- Poupardin A, Idier D, de Michele M, Raucoules D (2016) Water depth inversion from a single SPOT-5 dataset. *IEEE Trans Geosci Remote Sens*. <https://doi.org/10.1109/TGRS.2015.2499379>
- Priftis G, Lang TJ, Garg P, Nesbitt SW, Lindsley RD, Chronis T (2021) Evaluating the detection of mesoscale outflow boundaries using scatterometer winds at different spatial resolutions. *Remote Sens* 13:1334. <https://doi.org/10.3390/rs13071334>
- Quach B, Glaser Y, Stopa JE, Mouche AA, Sadowski PP (2021) Deep learning for predicting significant wave height from synthetic aperture radar. *IEEE Trans Geosci Remote Sens* 59(3):1859–1867. <https://doi.org/10.1109/TGRS.2020.3003839>
- Quilfen Y, Chapron B (2019) Ocean surface wave-current signatures from satellite altimeter measurements. *Geophys Res Lett* 46(1):253–261. <https://doi.org/10.1029/2018GL081029>
- Ranchin T, Trolliet M, Ménard L, Wald L (2020) Which variables are essential for renewable energies? *Int J Digital Earth* 13(2):253–261
- Raney RK (1998) The delay/Doppler radar altimeter. *IEEE Trans Geosci Remote Sens* 36(5):1578–1588
- Ray C, Martin-Puig C, Clarizia MP, Ruffini G, Dinardo S, Gommenginger C, Benveniste J (2015) SAR altimeter backscattered waveform model. *IEEE Trans Geosci Remote Sens* 53(2):911–919. <https://doi.org/10.1109/Tgrs.2014.2330423>
- Rayner R, Jolly C, Gouldman C (2019) Ocean observing and the blue economy. *Front Mar Sci*. <https://doi.org/10.3389/fmars.2019.00330>
- Renault L, Molemaker MJ, McWilliams JC, Shchepetkin AF, Lemarié F, Chelton D et al (2016a) Modulation of wind work by oceanic current interaction with the atmosphere. *J Phys Oceanogr* 46(6):1685–1704. <https://doi.org/10.1175/jpo-d-15-0232.1>
- Renault L, Molemaker MJ, Gula J, Masson S, McWilliams JC (2016b) Control and stabilization of the gulf stream by oceanic current interaction with the atmosphere. *J Phys Oceanogr* 46(11):3439–3453. <https://doi.org/10.1175/jpo-d-16-0115.1>
- Reul N, Chapron B (2003) A model of sea-foam thickness distribution for passive microwave remote sensing applications. *J Geophys Res* 108(C10):3321. <https://doi.org/10.1029/2003JC001887>
- Reul N, Tenerelli J, Chapron B, Vandemark D, Quilfen Y, Kerr Y (2012) SMOS satellite L-band radiometer: a new capability for ocean surface remote sensing in hurricanes. *J Geophys Res* 117:C02006. <https://doi.org/10.1029/2011JC007474>
- Reul N, Chapron B, Zabolotskikh E, Donlon C, Quilfen Y, Guimbard S, Piolle J-F (2016) A revised L-band radio-brightness sensitivity to extreme winds under tropical cyclones: the 5 year SMOS-storm database. *Remote Sens Environ* 180:274–291. <https://doi.org/10.1016/j.rse.2016.03.011>
- Reul N, Chapron B, Zabolotskikh E, Donlon C, Mouche A, Tenerelli J, Collard F, Piolle J-F, Fore A, Yueh S, Cotton J, Francis P, Quilfen Y, Kudryavtsev V (2017) A new generation of tropical cyclone size measurements from space. *Bull Am Meteor Soc* 98(11):2367–2386
- Ribal A, Young IR (2019) 33 years of globally calibrated wave height and wind speed data based on altimeter observations. *Sci Data*. <https://doi.org/10.1038/s41597-019-0083-9>
- Ribal A, Young IR (2020) Calibration and cross validation of global ocean wind speed based on scatterometer observations. *J Atmosph Oceanic Tech* 37(2):279–297. <https://doi.org/10.1175/JTECH-D-19-0119.1>
- Ricciardulli L, Manaster A (2021) Intercalibration of ASCAT scatterometers winds from MetOp-A, -B, and -C, for a stable climate data record. *Remote Sens* 13(18):3678. <https://doi.org/10.3390/rs13183678>
- Rice SD (1951) Reflection of electromagnetic waves from slightly rough surfaces. *Commun Pure Appl Math* 4(2/3):361–378



- Rieu P, Moreau T, Cadier E, Raynal M, Clerc S, Donlon C, Borde F, Boy F, Maraldi C (2021) Exploiting the Sentinel-3 tandem phase dataset and azimuth oversampling to better characterize the sensitivity of SAR altimeter sea surface height to long ocean waves. *Adv Space Res* 67(1):253–265
- Rodriguez E (2018) On the optimal design of Doppler scatterometers. *Remote Sens* 10(11):1765. <https://doi.org/10.3390/rs10111765>
- Rodriguez E, Esteban-Fernandez D, Peral E, Chen CW, De Bleser J-W, Williams B (2018) Wide-swath altimetry: a review. In: Stammer D, Cazenave A (eds) *Satellite altimetry over oceans and land surfaces*. Taylor and Francis, Milton Park
- Rodríguez E, Bourassa M, Chelton D, Farrar JT, Long D, Perkovic-Martin D, Samelson R (2019) The winds and currents mission concept. *Front Mar Sci* 6:438. <https://doi.org/10.3389/fmars.2019.00438>
- Rohrs J, Christensen KH, Vikebo F, Sundby S, Saetra Ø, Brostrom G (2014) Wave-induced transport and vertical mixing of pelagic eggs and larvae. *Limnol Oceanogr* 59(4):1213–1227. <https://doi.org/10.4319/lo.2014.59.4.1213>
- Röhrs J, Sperrevik AK, Christensen KH, Broström G, Breivik Ø (2015) Comparison of HF radar measurements with Eulerian and Lagrangian surface currents. *Ocean Dyn* 65:679–690. <https://doi.org/10.1007/s10236-015-0828-8>
- Röhrs J, Sutherland G, Jeans G, Bedington M, Sperrevik AL, Dagestad KF, Gusdal Y, Mauritzen C, Dale A, LaCasce JH (2021) Surface currents in operational oceanography: key applications, mechanisms, and methods. *J Operat Oceanogr*. <https://doi.org/10.1080/1755876X.2021.1903221>
- Romeiser R, Thompson DR (2000) Numerical study on the along-track interferometric radar imaging mechanism of oceanic surface currents. *IEEE Trans Geosci Remote Sens* 38(1):446–458
- Romeiser R, Suchandt S, Runge H, Steinbrecher U, Grünler S (2010) First analysis of TerraSAR-X along-track InSAR-derived current fields. *IEEE Trans Geosci Remote Sens* 48:820–829
- Romeiser R, Runge H, Suchandt S, Kahle R, Rossi C, Bell PS (2014) Quality assessment of surface current fields from TerraSAR-X and TanDEM-X along-track interferometry and Doppler centroid analysis. *IEEE Trans Geosci Remote Sens* 52:2759–2772
- Romeiser R, Graber HC, Caruso MJ, Jensen RE, Walker DT, Cox AT (2015) A new approach to ocean wave parameter estimates from C-band ScanSAR images. *IEEE Trans Geosci Remote Sens* 53(3):1320–1345. <https://doi.org/10.1109/TGRS.2014.2337663>
- Ruf CS, Chew C, Lang L et al (2018) A new paradigm in earth environmental monitoring with the CYGNSS small satellite constellation. *Sci Rep* 8:8782. <https://doi.org/10.1038/s41598-018-27127-4>
- Russell JL, Long DG et al (2021) Measuring vector winds from space to reduce the uncertainty in the southern ocean carbon fluxes: science requirements and proposed mission. *Geophys Res Lett*. <https://doi.org/10.1002/essoar.10506276.1>
- Sagawa T, Yamashita Y, Okumura T, Yamanokuchi T (2019) Satellite derived bathymetry using machine learning and multi-temporal satellite images. *Remote Sens* 11:1155
- Saïd F, Johnsen H, Chapron B, Engen G (2015) An ocean wind Doppler model based on the generalized curvature ocean surface scattering model. *IEEE Trans Geosci Remote Sens*. <https://doi.org/10.1109/TGRS.2015.2445057>
- Saïd F, Jelenak Z, Park J, Chang PS (2021) The NOAA track-wise wind retrieval algorithm and product assessment for CyGNSS. *IEEE Trans Geosci Remote Sens*. <https://doi.org/10.1109/TGRS.2021.3087426>
- Salameh E, Frappart F, Almar R, Baptista P, Heygster G, Lubac B, Raucoules D, Almeida LP, Bergsma EWJ, Capo S, De Michele M, Idier D, Li Z, Marieu V, Poupardin A, Silva PA, Turki I, Laignel B (2019) Monitoring beach topography and nearshore bathymetry using spaceborne remote sensing: a review. *Remote Sens* 11(18):2212. <https://doi.org/10.3390/rs11192212>
- Sampson CR, Schrader AJ (2000) The automated tropical cyclone forecasting system. *Bull Am Meteorol Soc* 81(6):1231–1240
- Sapp JW, Alsweiss SO, Jelenak Z, Chang PS, Carswell J (2019) Stepped frequency microwave radiometer wind-speed retrieval improvements. *Remote Sens* 11:214
- Saulter AN, Bunney C, King RR, Waters J (2020) An application of NEMOVAR for regional wave model data assimilation. *Front Mar Sci* 7:897. <https://doi.org/10.3389/fmars.2020.579834>
- Schlembach F, Passaro M, Quartly GD, Kurekin A, Nencioli F, Dodet G, Piollé J-F, Arduhuin F, Bidlot JR, Schwatke C (2020) Round robin assessment of radar altimeter low resolution mode and delay-Doppler retracking algorithms for significant wave height. *Remote Sens* 12(8):1254
- Schmitt RW (2018) The ocean's role in climate. *Oceanography* 31(2):32–40. <https://doi.org/10.5670/oceanog.2018.225>
- Schulz-Stellenfleh J, Lehner S, Hoja D (2005) A parametric scheme for the retrieval of two-dimensional ocean wave spectra from synthetic aperture radar look cross spectra. *J Geophys Res*. <https://doi.org/10.1029/2004JC002822>



- Schulz-Stellenfleh J, König T, Lehner S (2007) An empirical approach for the retrieval of integral ocean wave parameters from synthetic aperture radar data. *J Geophys Res* 122(3):1827–1848. <https://doi.org/10.1029/2006JC003970>
- Shao W, Li X, Sun J (2015) Ocean wave parameters retrieval from TerraSAR-X images validated against buoy measurements and model results. *Remote Sens* 7(10):12815–12828
- Shi Q, Bourassa MA (2019) Coupling ocean currents and waves with wind stress over the gulf stream. *Remote Sens* 11(12):1476. <https://doi.org/10.3390/rs11121476>
- Shibata A (2006) A wind speed retrieval algorithm by combining 6 and 10 GHz data from advanced microwave scanning radiometer: wind speed inside hurricanes. *J Oceanogr* 62:351–359
- Shipping World Council (2020) Containers lost at Sea 2020 update. [www.worldshipping.org/Containers\\_Lost\\_at\\_Sea\\_-\\_2020\\_Update\\_FINAL\\_.pdf](http://www.worldshipping.org/Containers_Lost_at_Sea_-_2020_Update_FINAL_.pdf)
- Sihan X et al (2020) Significant wave height retrieval from Sentinel-1 SAR imagery by convolutional neural network. *J Oceanogr* 76(6):465–477
- Sikora TD, Young GS, Beal RC, Edson JB (1995) Use of spaceborne synthetic aperture radar imagery of the sea surface in detecting the presence and structure of the convective marine atmospheric boundary layer. *Mon Weather Rev* 123(12):3623–3632. [https://doi.org/10.1175/1520-0493\(1995\)123h3623:uossari2.0.co;2](https://doi.org/10.1175/1520-0493(1995)123h3623:uossari2.0.co;2)
- Small C, Nicholls RJ (2003) A global analysis of human settlement in coastal zones. *J Coast Res* 19(3):584–599. <https://doi.org/10.2307/4299200>
- Smith N (2006) Perspectives from the global ocean data assimilation experiment. In: Chassignet EP, Verron J (eds) *Ocean weather forecasting*. Springer, Dordrecht
- Spencer MW, Wu CL, Long DG (2000) Improved resolution backscatter measurements with the SeaWinds pencil-beam scatterometer. *IEEE Trans Geosci Remote Sens* 38(1):89–104. <https://doi.org/10.1109/36.823904>
- Srokosz M (1986) On the joint distribution of surface elevation and slopes for a nonlinear random sea, with an application to radar altimetry. *J Geophys Res Oceans* 91(C1):995–1006
- Srokosz MA, Challenor PG, Guymier TH (1995) Satellite remote sensing of metocean parameters: present status and future prospects. Health and Safety Executive Books, Offshore Technology Report, OTH 93 421 ISBN 0-7176-0936-7. <https://www.hse.gov.uk/research/othpdf/400-499/oth421.pdf>
- Steele ECC, Davidson MA, Saulter A, Fournier N, Upton J (2019) Protection of critical oil and gas infrastructure via the skilful prediction of coastal erosion at short lead times. *Proc Offshore Technol Conf*. <https://doi.org/10.4043/29542-MS>
- Steele ECC, Brown H, Bunney C, Gill P, Mylne K, Saulter A, Standen J, Blair L, Cruickshank S, Gulbrandsen MK (2021) Using metocean forecast verification information to effectively enhance operational decision-making. *Proc Offshore Technol Conf*. <https://doi.org/10.4043/31253-MS>
- Stevens R, Calverley M, Jeans G (2021) Marine energy sector use of wave data, presentation to the ESA CCI sea state user consultation meeting 2021. [https://climate.esa.int/documents/1067/UCM2\\_Stephens\\_Calverley\\_Jeans.pdf](https://climate.esa.int/documents/1067/UCM2_Stephens_Calverley_Jeans.pdf)
- Stewart RH (1984) *Methods of satellite oceanography*. University of California Press, Berkeley
- Stoffelen A (1998) *Scatterometry*. PhD thesis University, Utrecht
- Stoffelen ACM, Anderson DLT (1997) Scatterometer data interpretation: derivation of the transfer function CMOD4. *J Geophys Res* 102(C3):5767–5780
- Stoffelen A, Wagner W (2013) The ERS scatterometer: achievements and the future, in ERS missions: 20 years of observing earth. In: Fletcher K (ed) *ESA SP-1326*. Publisher ESA Communications, Noordwijk
- Stoffelen A, Paillex J, Källén E, Vaughan JM, Isaksen L, Flamant P, Wergen W, Andersson E, Schyberg H, Culoma A, Meynart R, Endemann M, Ingmann P (2005) The atmospheric dynamics mission for global wind field measurement. *Bull Am Meteorol Soc* 86(1):73–88. <https://doi.org/10.1175/BAMS-86-1-73>
- Stoffelen A, Verspeek JA, Vogelzang J, Verhoef A (2017a) The CMOD7 geophysical model function for ASCAT and ERS wind retrievals. *IEEE J Select Top Appl Earth Obs Remote Sens* 10(5):2123–2134. <https://doi.org/10.1109/JSTARS.2017.2681806>
- Stoffelen A et al (2017b) Scientific developments and the EPS-SG scatterometers. *J Sel Topics Appl Earth Obs Remote Sens* 10(5):2086–2097. <https://doi.org/10.1109/JSTARS.2017.2696424>
- Stoffelen A, Kumar R, Zou J, Karaev V, Chang PS, Rodriguez E (2019) Ocean surface vector wind observations. In: Barale V, Gade M (eds) *Remote sensing of the Asian Seas*. Springer, Cham
- Stoffelen A, Vogelzang J (2021) Wind bias correction guide. In: EUMETSAT NWP SAF Document NWP-SAF-KN-UD-007. KNMI, The Netherlands. [https://nwp-saf.eumetsat.int/site/download/documentat ion/scatterometer/Wind\\_Bias\\_Correction\\_Guide\\_v1.5.pdf](https://nwp-saf.eumetsat.int/site/download/documentat ion/scatterometer/Wind_Bias_Correction_Guide_v1.5.pdf)

- Stoffelen A, Vogelzang J, Lin W (2015) On buoys, scatterometers and reanalyses for globally representative winds. EUMETSAT NWP SAF report NWPSAF-KN-TR-024. [https://www.nwpsaf.eu/publications/tech\\_reports/nwpsaf-kn-tr-024.pdf](https://www.nwpsaf.eu/publications/tech_reports/nwpsaf-kn-tr-024.pdf)
- Stoffelen A, Mouche AA, Polverari F, van Zadelhoff G, Sapp J, Portabella M, Chang P, Lin W, Jelenak Z (2020a) C-band high and extreme-force speeds (CHEFS). In: EUMETSAT project final report. Darmstadt, Germany. <https://www.eumetsat.int/CHEFS>
- Stoffelen A, Vogelzang J, Marseille G-. (2020b) High resolution data assimilation guide. In: EUMETSAT NWP SAF documentation, version 1.3. KNMI, The Netherlands. [https://nwp-saf.eumetsat.int/site/download/documentation/scatterometer/reports/High\\_Resolution\\_Wind\\_Data\\_Assimilation\\_Guide\\_1.3.pdf](https://nwp-saf.eumetsat.int/site/download/documentation/scatterometer/reports/High_Resolution_Wind_Data_Assimilation_Guide_1.3.pdf)
- Stoffelen A, Marseille G-J, Ni W, Mouche A, Polverari F, Portabella M, Lin W, Sapp J, Chang PS, Jelenak Z (2021) Hurricane Ocean wind speeds. IGARSS Conference Paper TH1.O-10.5. <https://igarss2021.com/> 12–16 July 2021
- Stoffelen A et al. (2013) Research and development in Europe on global application of the OceanSat-2 Scatterometer Winds. NWP SAF report NWPSAF-KN-TR-022. [http://www.knmi.nl/publications/fulltexts/oceansat\\_cal\\_val\\_report\\_final\\_copy1.pdf](http://www.knmi.nl/publications/fulltexts/oceansat_cal_val_report_final_copy1.pdf)
- Stogryn A (1972) The emissivity of sea foam at microwave frequencies. *J Geophys Res* 77:1658–1666
- Stopa JE, Mouche A (2017) Significant wave heights from Sentinel-1 SAR: validation and applications. *J Geophys Res Oceans* 122:1827–1848. <https://doi.org/10.1002/2016JC012364>
- Stopa JE, Sutherland P, Ardhuin F (2018) Strong and highly variable push of ocean waves on Southern Ocean sea ice. *P Natl Acad Sci USA* 115:5861–5865. <https://doi.org/10.1073/pnas.1802011115>
- Stopa JE, Chen W, Vandemark D, Foster R, Mouche A, Chapron B (2022) Automated global classification of surface layer stratification using high-resolution sea surface roughness measurements by satellite synthetic aperture radar. *Geophys Res Lett* 49(12):e2022GL098686. <https://doi.org/10.1029/2022GL098686>
- Takbash A, Young IR, Breivik Ø (2019) Global wind speed and wave height extremes derived from long-duration satellite records. *J Clim* 32(1):109–126. <https://doi.org/10.1175/JCLI-D-18-0520.1>
- The International Altimetry Team (2021) Altimetry for the future: building on 25 years of progress. *Adv Space Res* 68(2):319–363
- The WISE Group, Cavaleri L et al (2007) Wave modelling—The state of the art. *Prog Oceanogr* 75:603–674. <https://doi.org/10.1016/j.pocean.2007.05.005>
- Thibaut P, Poisson J, Bronner E, Picot N (2010) Relative performance of the MLE3 and MLE4 retracking algorithms on Jason-2 altimeter waveforms. *Mar Geodesy* 33(S1):317–335
- Timmermans B, Gommenginger C, Dodet G, Bidlot JR (2020) Global wave height trends and variability from new multimission satellite altimeter products. *Reanal Wave Buoys Geophys Res Lett* 47(9):e2019GL086880
- Tokmakian R, Challenor P, Guymer T, Srokosz M (1994) The UK EODC ERS-1 altimeter oceans processing scheme. *Int J Remote Sens* 15(4):939–962
- Tran N, Labroue S, Philipps S, Bronner E, Picot N (2010) Overview and update of the sea state bias corrections for the Jason-2, Jason-1 and TOPEX missions. *Mar Geodesy* 33(S1):348–362
- Trindade A, Portabella M, Stoffelen A, Lin W, Verhoef A (2020) ERAstar: a high-resolution ocean forcing product. *IEEE Trans Geosci Remote Sens* 58(2):1337–1347. <https://doi.org/10.1109/TGRS.2019.2946019>
- Trokhimovski YG, Kuzmin AV, Pospelov MN, Irisov VG, Sadovsky IN (2003) Laboratory polarimetric measurements of microwave emission from capillary waves. *Radio Sci.* <https://doi.org/10.1029/2002RS002661>
- Tsai W, Spencer TM, Wu C, Winn C, Kellogg K (2000) SeaWinds on QuikSCAT: sensor description and mission overview. *Proc IEEE 2000 Int Geosci Remote Sens Symp* 3:1021–1023. <https://doi.org/10.1109/IGARSS.2000.858008>
- Turner IL, Harley MD, Almar R, Bergsma EWJ (2021) Satellite optical imagery in coastal engineering. *Coastal Eng* 167:103919. <https://doi.org/10.1016/j.coastaleng.2021.103919>
- Ubelmann C, Dibarboure G, Gaultier L, Ponte A, Ardhuin F, Ballarotta M, Faugère Y (2021) Reconstructing ocean surface current combining altimetry and future spaceborne Doppler data. *J Geophys Res Oceans* 126(3):e2020JC16560
- Uhlhorn EW, Black PG (2003) Verification of remotely sensed sea surface winds in hurricanes. *J Atmos Oceanic Technol* 20:99–116. [https://doi.org/10.1175/1520-0426\(2003\)020%3c0099:VORSSS%3e2.0.CO;2](https://doi.org/10.1175/1520-0426(2003)020%3c0099:VORSSS%3e2.0.CO;2)
- Uhlhorn EW, Black PG, Franklin JL, Goodberlet M, Carswell J, Goldstein AS (2007) Hurricane surface wind measurements from an operational stepped frequency microwave radiometer. *Mon Wea Rev* 135:3070–3085. <https://doi.org/10.1175/MWR3454.1>

- UK Government (2021) Shipping fleet statistics: 2020. Department for transport technical report. [https://assets.publishing.service.gov.uk/government/uploads/system/uploads/attachment\\_data/file/967763/shipping-fleet-statistics-2020.pdf](https://assets.publishing.service.gov.uk/government/uploads/system/uploads/attachment_data/file/967763/shipping-fleet-statistics-2020.pdf)
- Ulabay F, Long D (2015) Microwave radar and radiometric remote sensing. The University of Michigan Press, Ann Arbor
- UNCTD (2021) Review of Maritime Transport 2018. United Nations conference on trade and development technical report. <https://unctad.org/topic/transport-and-trade-logistics/review-of-maritime-transport>
- Unwin M, Jales P, Tye J, Gommenginger C, Foti G, Rosello J (2016) Spaceborne GNSS-reflectometry on TechDemoSat-1: early mission operations and exploitation. *IEEE J Select Top Appl Earth Obs Remote Sens* 9(10):4525–4539. <https://doi.org/10.1109/JSTARS.2016.2603846>
- Unwin M, Pierdicca N, Cardellach E, Rautiainen K, Foti G, Blunt P, Guerriero L, Santi E, Tossaint M (2021) An introduction to the HydroGNSS GNSS reflectometry remote sensing mission. *IEEE J Select Top Appl Earth Obs Remote Sens* 14:6987–6999. <https://doi.org/10.1109/JSTARS.2021.3089550>
- Vachon P, Raney RK (1991) Resolution of the ocean wave propagation direction in SAR imagery. *IEEE Trans Geosci Remote Sens* 29:105–112
- Vachon PW, Wolfe J (2011) C-band cross-polarization wind speed retrieval. *IEEE Geosci Remote Sens Lett* 8(3):456–459
- Valenzuela GR (1978) Theories for the interaction of electromagnetic and oceanic waves—a review. *Bound Layer Meteorol* 13:61–85
- van Sebille E et al (2020) The physical oceanography of the transport of floating marine debris. *Environ Res Lett* 15:023003
- Verhoef A, Vogelzang J, Verspeek J, Stoffelen A (2017) Long-term scatterometer wind climate data records. *IEEE J Select Top Appl Earth Obs Remote Sens* 10(5):2186–2194. <https://doi.org/10.1109/JSTARS.2016.2615873>
- Verron J, Bonnefond P et al (2018) The benefits of the Ka-band as evidenced from the SARAL/AltiKa altimetric mission: scientific applications. *Remote Sens* 10(2):163
- Viatte C, Clerbaux C, Maes C, Daniel P, Garellio R, Safeddine S, Ardhuin F (2020) Air and sea pollution seen from space. *Surv Geophys*. <https://doi.org/10.1007/s10712-020-09599-0>
- Vignudelli S, Kostianoy AG, Cipollini P, Benveniste J (2011) Coastal altimetry. Springer, Berlin
- Villas-Bôas AB et al (2019) Integrated observations of global surface winds, currents, and waves: requirements and challenges for the next decade. *Front Mar Sci*. <https://doi.org/10.3389/fmars.2019.00425>
- Vogelzang J, Stoffelen A (2017) ASCAT ultrahigh-resolution wind products on optimized grids. *IEEE J Select Topics Appl Earth Obs Remote Sens* 10(5):2332–2339. <https://doi.org/10.1109/JSTARS.2016.2623861>
- Vogelzang J, Stoffelen A (2021) Quadruple collocation analysis of in-situ, scatterometer, and NWP winds. *J Geophys Res Oceans* 126:20289. <https://doi.org/10.1029/2021JC017189>
- Voorrips AC, de Valk C (1997) A comparison of two operational wave assimilation methods. *The Global Atmos Ocean Syst* 7(1):4532
- Voorrips AC, Makin VK, Hasselmann S (1997) Assimilation of wave spectra from pitch and roll buoys in a North Sea wave model. *J Geophys Res* 102:5829–5849
- Voorrips AC, Heemink AW, Komen GJ (1999) Wave data assimilation with the Kalman filter. *J Mar Syst* 19(4):267–291
- Voorrips AC (1998) Sequential data assimilation methods for ocean wave models. PhD thesis. <https://repository.tudelft.nl/islandora/object/uuid:3e446d99-e02c-4836-a629-6f5d82f7fd48/datastream/OBJ/download>
- WAMDI Group (1988) The wam model—a third generation ocean wave prediction model. *J Phys Oceanogr* 18(12):1775–1810. [https://doi.org/10.1175/1520-0485\(1988\)018%3c1775:TWMTGO%3e2.0.CO;2](https://doi.org/10.1175/1520-0485(1988)018%3c1775:TWMTGO%3e2.0.CO;2)
- Wang Z, Stoffelen A, Fois F, Verhoef A, Zhao C, Lin M, Chen G (2017) SST dependence of Ku- and C-Band backscatter measurements. *IEEE J Select Top Appl Earth Obs Remote Sensing* 10(5):2135–2146. <https://doi.org/10.1109/JSTARS.2016.2600749>
- Wang Z, Stoffelen A, Zou J, Lin W, Verhoef A, Zhang Y, He Y, Lin M (2020) Validation of new sea surface wind products from scatterometers onboard the HY-2B and MetOp-C satellites. *IEEE Trans Geosci Remote Sens* 58(6):4387–4394. <https://doi.org/10.1109/TGRS.2019.2963690>
- Wang H, Mouche A, Husson R, Grouazel A, Chapron B, Yang J (2022) Assessment of ocean swell height observations from Sentinel-1A/B wave mode against buoy in situ and modeling hindcasts. *Remote Sens* 14:862. <https://doi.org/10.3390/rs14040862>
- Waugh DW, Primeau F, DeVries T, Holzer M (2013) Recent changes in the ventilation of the southern oceans. *Science* 339:568–570. <https://doi.org/10.1126/science.1225411>

- Wentz FJ, Ricciardulli L, Rodriguez E, Stiles BW, Bourassa MA, Long DG, Hoffma RN, Stoffelen A, Verhoef A, O'Neill LW et al (2017) Evaluating and extending the ocean wind climate data record. *IEEE J Sel Top Appl Earth Obs Remote Sens* 10(5):2165–2185. <https://doi.org/10.1109/JSTARS.2016.2643641>
- Wentz F (2005) The effects of cloud and rain on the Aquarius salinity retrieval. In: RSS technical report 3031805, Remote Sensing Systems, Santa Rosa. [http://images.remss.com/papers/rsstech/2005\\_3031805\\_Wentz\\_rain\\_effect\\_on\\_salinity.pdf](http://images.remss.com/papers/rsstech/2005_3031805_Wentz_rain_effect_on_salinity.pdf)
- Wingham DJ, Phalippou L, Mavrocordatos C, Wallis D (2004) The mean echo and echo cross product from a beamforming interferometric altimeter and their application to elevation measurement. *IEEE Trans Geosci Remote Sens* 42(10):2305–2323
- Witter DL, Chelton DB (1991) A Geosat altimeter wind speed algorithm and a method for altimeter wind speed algorithm development. *J Geophys Res Oceans* 96(C5):8853–8860
- Xu X, Stoffelen A (2020) Improved rain screening for Ku-band wind scatterometry. *IEEE Trans Geosci Remote Sens* 58(4):2494–2503. <https://doi.org/10.1109/TGRS.2019.2951726>
- Xu X, Stoffelen A (2021) Support vector machine tropical wind speed retrieval in the presence of rain for Ku-band wind scatterometry. *Atmos Meas Tech* 14:7435–7451. <https://doi.org/10.5194/amt-14-7435-2021>
- Ying Xu, Hauser D, Liu J, Si J, Yan C, Chen S, Meng J, Fan C, Liu M, Chen P (2022) Statistical comparison of ocean wave directional spectra derived from SWIM/CFOSAT satellite observations and from buoy observations. *IEEE Trans Geosci Remote Sens* 60:1–20. <https://doi.org/10.1109/TGRS.2022.3199393>
- Young IR, Ribal A (2019) Multiplatform evaluation of global trends in wind speed and wave height. *Science* 364(6440):eaav9527. <https://doi.org/10.1126/science.aav9527>
- Young IR, Ribal A (2022) Can multi-mission altimeter datasets accurately measure long-term trends in wave height? *Remote Sens* 14:974. <https://doi.org/10.3390/rs14040974>
- Young GS, Sikora TD, Winstead NS (2005) Use of synthetic aperture radar in finescale surface analysis of synoptic-scale fronts at sea. *Weather Forecast* 20(3):311–327. <https://doi.org/10.1175/waf853.1>
- Young IR, Vinoth J, Zieger S, Babanin AV (2012) Investigation of trends in extreme value wave height and wind speed. *J Geophys Res Ocean*. <https://doi.org/10.1029/2011JC007753>
- Yueh SH, Kwok R, Li FK, Nghiem SV, Wilson WJ, Kong JA (1994a) Polarimetric passive remote sensing of ocean wind vectors. *Radio Sci* 29(4):799–814
- Yueh SH, Kwok R, Nghiem SV (1994b) Polarimetric scattering and emission properties of targets with reflection symmetry. *Radio Sci* 29(6):1409–1420
- Yueh SH, Wilson WJ, Li FK, Nghiem SV, Ricketts WB (1995) Polarimetric measurements of sea surface brightness temperatures using an aircraft K-band radiometer. *IEEE Trans Geosci Remote Sens* 33(1):85–92. <https://doi.org/10.1109/36.368219>
- Yueh SH, Wilson WJ, Dinardo SJ, Hsiao SV (2006) Polarimetric microwave wind radiometer model function and retrieval testing for WindSat. *IEEE Trans Geosci Remote Sens* 44(3):584–596. <https://doi.org/10.1109/TGRS.2005.858416>
- Yueh SH, Tang W, Fore AG, Neumann G, Hayashi A, Freedman A, Chaubell J, Lagerloef GSE (2013) L-band passive and active microwave geophysical model functions of ocean surface winds and applications to aquarius retrieval. *IEEE Trans Geosci Remote Sens* 51:4619–4632
- Yueh SH, Fore AG, Tang W, Hayashi A, Stiles B, Reul N, Weng Y, Zhang F (2016) SMAP L-band passive microwave observations of Ocean surface wind during severe storms. *IEEE Trans Geosci Remote Sens* 54(12):7339–7350
- Yurovskaya M, Kudryavtsev V, Chapron B, Collard F (2019) Ocean surface current retrieval from space: the Sentinel-2 multispectral capabilities. *Remote Sens Environ* 234:111468. <https://doi.org/10.1016/j.rse.2019.111468>
- Yurovsky YY, Kudryavtsev VN, Grodsky SA, Chapron B (2021) Ka-band radar cross-section of breaking wind waves. *Remote Sens* 13:1929. <https://doi.org/10.3390/rs13101929>
- Zabolotskikh EV, Reul N, Chapron B (2016) Geophysical Model Function for the AMSR2 C-band wind excess emissivity at high winds. *IEEE Geosci Remote Sens Lett* 13(1):78–81
- Zaron ED, DeCarvalho R (2016) Identification and reduction of retracker-related noise in altimeter-derived sea surface height measurements. *J Atmos Oceanic Tech* 33(1):201–210
- Zebker HA, Villasenor J (1992) Decorrelation in interferometric radar echoes. *IEEE Trans Geosci Remote Sens* 30:950–959
- Zecchetto S (2018) Wind direction extraction from SAR in coastal areas. *Remote Sens* 10(2):261
- Zhang B, Perrie W (2012) Cross-polarized synthetic aperture radar: A new potential measurement technique for hurricanes. *Bull Am Meteorol Soc* 93(4):531–541. <https://doi.org/10.1175/BAMS-D-11-00001.1>
- Zhang B, Perrie W, Vachon PW, Li X, Pichel WG, Guo J, He Y (2012) Ocean vector winds retrieval from c-band fully polarimetric sar measurements. *IEEE Trans Geosci Remote Sens* 50(11):4252–4261

- Zhao D, Li M (2019) Dependence of wind stress across an air–sea interface on wave states. *J Oceanogr* 75:207–223. <https://doi.org/10.1007/s10872-018-0494-9>
- Zhou L, Zheng G, Li X, Yang J, Ren L, Chen P, Zhang H, Lou X (2017) An improved local gradient method for sea surface wind direction retrieval from SAR imagery. *Remote Sens* 9(7):671
- Zieger S, Vinoth J, Young I (2009) Joint calibration of multiplatform altimeter measurements of wind speed and wave height over the past 20 years. *J Atmos Oceanic Tech* 26(12):2549–2564
- Zijl F, Verlaan M, Gerritsen H (2013) Improved water-level forecasting for the Northwest European shelf and north sea through direct modeling of tide, surge and non-linear interaction. *Ocean Dyn* 63:823–847. <https://doi.org/10.1007/s10236-013-0624-2>

**Publisher's Note** Springer Nature remains neutral with regard to jurisdictional claims in published maps and institutional affiliations.

## Authors and Affiliations

**Danièle Hauser<sup>1</sup>**  · **Saleh Abdalla<sup>2</sup>** · **Fabrice Ardhuin<sup>3</sup>** · **Jean-Raymond Bidlot<sup>2</sup>** · **Mark Bourassa<sup>4</sup>** · **David Cotton<sup>5</sup>** · **Christine Gommenginger<sup>6</sup>** · **Hayley Evers-King<sup>7</sup>** · **Harald Johnsen<sup>8</sup>** · **John Knaff<sup>9</sup>** · **Samantha Lavender<sup>10</sup>** · **Alexis Mouche<sup>3</sup>** · **Nicolas Reul<sup>3</sup>** · **Charles Sampson<sup>11</sup>** · **Edward C.C Steele<sup>7</sup>** · **Ad Stoffelen<sup>12</sup>**

✉ Danièle Hauser  
daniele.hauser@latmos.ipsl.fr

<sup>1</sup> LATMOS, CNRS; University of Versailles Saint-Quentin; Sorbonne University, 11 Boulevard d'Alembert, 78280, Guyancourt, France

<sup>2</sup> European Centre for Medium-Range Weather Forecasts, RG2 9AX Reading, UK

<sup>3</sup> Present Address: LOPS, Université de Bretagne Occidentale; CNRS; Ifremer; IRD, Technopôle Brest Iroise, 29280 Plouzané, France

<sup>4</sup> Centre for Ocean-Atmosphere Prediction Studies, Florida State University, FL 32306 Tallahassee, Florida, USA

<sup>5</sup> Satellite Oceanographic Consultants Limited, SK22 4QF New Mills, UK

<sup>6</sup> National Oceanography Center, SO14 3ZH Southampton, UK

<sup>7</sup> Met Office, EX1 3PB Exeter, Devon, UK

<sup>8</sup> NORCE Norwegian Research Center AS, Postboks 6434, 929 Tromsø, Norway

<sup>9</sup> Center for Satellite Applications and Research, NOAA, CO 80523-1375 Fort Collins, USA

<sup>10</sup> Pixalytics Ltd, PL6 8BX Plymouth, UK

<sup>11</sup> Naval Research Laboratory, CA 93943 Monterey, California, USA

<sup>12</sup> KNMI, 3731 GA De Bilt, The Netherlands